High Pressure Ignition Chemistry of Alternative Fuels

Bryan William Weber, Ph.D.

University of Connecticut, 2014

Abstract

High Pressure Ignition Chemistry of Alternative Fuels

Bryan William Weber

B.S., Case Western Reserve University, 2009

M.S., University of Connecticut, 2010

A Dissertation

Submitted in Partial Fulfillment of the

Requirements for the Degree of Doctor of Philosophy

at the

University of Connecticut

2014

2014

APPROVAL PAGE

Doctor of Philosophy Dissertation

High Pressure Ignition Chemistry of Alternative Fuels

Presented by

Bryan William Weber, B.S., M.S.

Major Advisor _____
Chih-Jen Sung

Associate Advisor _____
Baki Cetegen

Associate Advisor _____
Michael Renfro

University of Connecticut

2014

Acknowledgements

So long, and thanks for all the fish.

Contents

List of Figures

viii

List of Tables

Chapter 1

Introduction

1.1 Background

The world relies heavily on combustion to provide energy in useful forms for human consumption; combustion currently represents over 80 % of the world energy production [1] and is predicted to decrease in importance only slightly by 2040 [2]. In particular, the transportation sector accounts for nearly 40 % of the energy use in the United States and of that, more than 90 % is supplied by combustion of fossil fuels [3]. Unfortunately, emissions from the combustion of traditional fossil fuels have been implicated in a host of deleterious effects on human health and the environment [4] and fluctuations in the price of traditional fuels can have a negative impact on the economy [5].

Despite its shortcomings, combustion is currently the only energy conversion mechanism that offers the immediate capability to generate the sheer amount of energy required to run the modern world. Since we cannot eliminate combustion as an important energy conversion method, we must instead ameliorate the shortcomings of a primarily combustion-based energy economy. A two-pronged approach has been developed to achieve the necessary improvements. These approaches include: 1) development of new fuel sources and 2) development of new combustion technologies. First, using new sources of fuel for combustion-based energy conversion can reduce the economic impact of swings in the price of current fuels, in addition to potentially reducing emissions. Second,

using new combustion technologies can reduce harmful emissions while simultaneously increasing the efficiency of combustion processes, thereby reducing fuel consumption.

Many new sources of fuels have been investigated recently. The most promising of these in the long term are renewable biological sources, which are used to produce fuels known as biofuels. The advantage of biofuels over traditional fuels lies in their feedstocks. Whereas traditional fuel feedstocks generally require millions of years to be produced, biofuel feedstocks are replenished on an annual basis. Furthermore, biofuels offer the potential to offset carbon emissions created from their combustion by reusing the emitted carbon to grow the plants from which the fuels are produced.

However, the combustion properties of biofuels may be substantially different from the traditional fuels they are intended to replace. This makes it difficult to quickly switch the energy economy to biofuels and necessitates medium-term investigation of alternative sources for traditional fuels. These sources include shale oil and liquefied coal, which have different chemical compositions than traditional fuel sources and therefore fuels made from these alternative sources have different combustion properties. Collectively, all of these fuels created from non-traditional sources are known as alternative fuels.

In addition to new fuel sources, new engine technologies are rapidly being developed. These include engines capable of operating in favorable combustion regimes, such as so-called Low Temperature Combustion (LTC) engines and Homogeneous Charge Compression Ignition (HCCI) engines. These devices avoid regions in the temperature-equivalence ratio space where combustion generates a large amount of emissions and operate in regions where efficiency is maximized and emissions are reduced. Other devices, such as the well-known catalytic converter, operate on the exhaust after it leaves the cylinder to improve emissions characteristics.

Neither of these approaches is able to mitigate all of the negative impacts of combustion by itself. By switching to biofuels but retaining the same engines, the efficiency and emissions targets may not be met; by only developing new engines, our sources of fuel will continue to cause economic distress, turmoil, and negative effects on the environment. It will take a concerted effort to bring

these two pathways of innovation together.

Unfortunately, there are many roadblocks on the way to combining new fuels in new engines. For instance, one can imagine the design and testing process of new engines and fuels becoming circular: the "best" alternative fuel should be tested in the "best" engine, but the "best" engine depends on which is selected as the "best" alternative fuel. One way to cut this circle short is by employing computer-aided design and modeling of new engines with new fuels to design engines to be fuel-flexible. Accurate and predictive models of combustion processes can be used to computationally test the efficacy of new technologies and fuels before they undergo expensive real-world testing. The key to this process is the development of accurate and predictive combustion models.

Substantial work has been put forth recently to develop and validate predictive combustion models for several alternative fuels. These studies include calculation and measurement of reaction rate coefficients, measurement of global and local combustion properties, and development of model construction methodologies. Nevertheless, much of the work is still ongoing, and there is substantial room for extending the state-of-the-art knowledge, especially at high-pressure conditions relevant to combustion in engines.

A combustion model for the combustion of a given fuel in a given device must necessarily accurately model the complete interaction of the operating elements of the device. This includes sub-models for the chemical reactions that the fuel and oxidizer undergo as well as the interaction of the fuel/oxidizer mixture with the operation of the device. The first of these is known as a chemical kinetic model or reaction mechanism; the second typically includes such effects as turbulence interaction, heat transfer, liquid spray dynamics, fluid mechanics, etc., each of which are typically modeled independently.

Chemical kinetic models for the combustion of large molecules are typically built in a hierarchical fashion, as described by Westbrook and Dryer [6]. That is, the model for the combustion of heptane contains the model for the combustion of hexane added to the model of combustion for pentane, and so on down to the models for hydrogen and carbon monoxide combustion. Therefore, it is important

3

to thoroughly validate the models for smaller species while building models of higher hydrocarbons and other molecular types. Work has been ongoing to explore the chemistry of small molecules for decades. Notable recent kinetic mechanisms to emerge from this work include the GRI-Mech series of mechanisms (most recently, version 3.0 [7]), USC-Mech v2 [8], and the AramcoMech series of mechanisms, most recently version 1.3 [9].

Validation of kinetic models for the combustion of larger fuels has proceeded in parallel with the small molecule chemistry. Given their projected importance to combustion, one focus of the larger molecule work has naturally been on biofuels. These biofuels typically include chemical species such as alcohols and esters – neat alcohols can be used as fuels, while esters are typically found as components of biodiesel fuels. A review by Kohse-Höinghaus et al. [10] covers much of the experimental data available until 2010. Since then an enormous amount of data has been produced for both alcohols and esters. Since the focus of this study is on alcohols, I will highlight alcohols in the following sections.

Model construction and validation has also been focused on alternative "traditional" fuels, that is, fuels that are chemically similar to traditional fuels but produced from alternative sources such as shale oil or coal liquefaction. Traditional fuels and alternative "traditional" fuels typically contain hundreds or thousands of chemical components. This makes building and using models containing every species present in the fuel intractable on current computer hardware. Therefore, a more useful approach to building models for these fuels is to define a surrogate fuel. Surrogate fuels are made of a limited number of chemical components to ensure that model building and use are tractable, but the components are chosen so that the surrogate fuel faithfully reproduces the physical and chemical properties of the real fuel.

Much progress has been made recently to construct surrogates for typical transportation fuels. For instance, work on diesel surrogate formulation has recently been reviewed by Pitz and Mueller [11], work on gas turbine fuel surrogates has been briefly summarized by Dooley et al. [12], and work on gasoline surrogates has been summarized in the work of Anand et al. [13] and Pitz et al. [14]. One typical component class in the surrogate formulations is a cycloalkane or alkyl-cycloalkane

4

(collectively known as naphthenes), due to this class' presence in nearly all transportation fuels [14–17]. One particular cycloalkane, methylcyclohexane (MCH), has been suggested in several surrogate formulations, including those by Bieleveld et al. [18] and Naik et al. [19]. Recent work on MCH combustion will also be highlighted in the following sections.

1.2 Recent Work on the Combustion of Alcohols

Among the alcohols being considered as biofuels, two criteria are typically used to judge the suitability of a species: 1) its ease of production and 2) its potential as a "drop-in" replacement for current fuels. Because of these criteria (among others), much research recently has focused on the isomers of butanol, the C_4 alcohols, and i-pentanol, a C_5 alcohol. This is because these fuels are easy to produce by a number of biological pathways [20] and offer similar properties as gasoline for use in typical automotive transportation applications [21, 22].

One of the most common biofuels currently in use is ethanol (C_2H_6O). Although ethanol is ubiquitous at gasoline pumps, it suffers from several disadvantages that suggest it needs to be replaced [23]. In particular, ethanol has a much lower energy density than gasoline, reducing volumetric fuel economy, and ethanol is typically produced from crops that would otherwise be used as food sources [24].

n-Butanol has recently been identified as one of a suite of so called "second generation" biofuels intended to supplement or replace the "first generation" biofuels currently in use, such as ethanol [25, 26]. The second generation biofuels will help alleviate some of the problems identified with the first generation biofuels, including concerns about feedstocks. In addition to the normal (n) isomer, there are three other isomers of butanol— s-, i-, and t-butanol. Biological production pathways have been identified for n-, s-, and i-butanol [26, 27], but t-butanol is a petroleum derived product. Nevertheless, t-butanol is currently used as an octane enhancer in gasoline.

In the last five years, research into the combustion characteristics of the isomers of butanol has exploded, so exemplary references are provided here except for the articles of particular interest to

this work. In addition to applied engine research [28–30], fundamental combustion measurements have been made using many different systems. These include laminar flame speeds [31], jet-stirred reactor chemistry [32], low-pressure flame structure [33, 34], atmospheric pressure flame structure [35], pyrolysis [36–38], flow reactors [39, 40], and ignition delays, which will be discussed in more detail shortly. Other researchers have measured or calculated the reaction rate constants of reactions of butanol with various radicals, including OH [41–49], HO_2 [50–52], and CH_3 [53, 54].

Several studies of ignition delay of the butanol isomers have been conducted in both STs (STs) and Rapid Compression Machines (RCMs), including work in STs by Moss et al. [55], Black et al. [56], Noorani et al. [57], Zhang et al. [58], Stranic et al. [59], Yasunaga et al. [60], Heufer et al. [61], Vranckx et al. [62], and Zhu et al. [63] and work in RCMs by Weber et al. [64], Weber and Sung [65], Weber et al. [66], and Karwat et al. [67]. These studies have covered a wide range of temperature-pressure regimes, from 1 bar to 90 bar and 675 K to 1800 K.

Among the ST ignition studies, Moss et al. [55] have done measurements for all four isomers of butanol at 1 bar and 4 bar and 1200 K to 1800 K, over equivalence ratios of $\phi = 0.5$, 1.0, and 2.0 and fuel mole percentages of 0.25 %, 0.5 %, and 1.0 %. Black et al. [56] investigated autoignition for n-butanol from 1100 K to 1800 K and 1 atm, 2.6 atm, and 8 atm over equivalence ratios of $\phi = 0.5$, 1.0, and 2.0 and fuel mole percentages of 0.6 %, 0.75 %, and 3.5 %. Noorani et al. [57] investigated the ignition delays of the primary alcohols from C_1–C_4 at pressures of 2 atm, 10 atm, and 12 atm under dilute conditions for equivalence ratios $\phi = 0.5$, 1.0, and 2.0, and temperatures from 1070 K to 1760 K. Zhang et al. [58] measured ignition delays of n-butanol at pressures of 2 atm and 10 atm, temperatures in the range of 1200 K to 1650 K, and for equivalence ratios of 0.5, 1.0, and 2.0. Stranic et al. [59] measured ignition delays of all four isomers of butanol over the pressure range 1.5 atm to 43 atm, temperature range 1050 K to 1600 K, and equivalence ratios of 0.5 and 1.0. These studies showed generally good agreement of the ignition delays for n-butanol, but Stranic et al. [59] found that their ignition delays for the other isomers of butanol were shorter than the ignition delays measured by Moss et al. [55]. Stranic et al. [59] were unable to determine the reason for the discrepancy.

Yasunaga et al. [60] measured ignition delays of s-, t-, and i-butanol at a pressure of 3.5 atm

and temperatures between 1250 K to 1800 K. In addition, Yasunaga et al. [60] measured reactant, intermediate, and product species during pyrolysis of all four butanol isomers by sample extraction from their ST and analysis by gas chromatography. Other researchers have measured species profiles during the pyrolysis of butanol isomers in a ST by optical techniques, including Cook et al. [68], Stranic et al. [69, 70], and Rosado-Reyes and Tsang [71, 72]. At Stanford University, researchers measured the time-history of the concentration of the fuel, OH, H_2O, C_2H_4, CO, and CH_4 behind reflected shock waves for n-, s-, and i-butanol [68–70]. Rosado-Reyes and Tsang [71, 72] measured the thermal decomposition of n- and s-butanol in a single-pulse ST and derived rate expressions for the decomposition reactions.

Heufer et al. [61] reported high pressure ignition delay results of stoichiometric n-butanol/air mixtures under the conditions behind the reflected shock of approximately 10 bar to 42 bar and 770 K to 1250 K. The results of Heufer et al. [61] showed an interesting non-Arrhenius behavior at temperatures lower than about 1000 K for the pressure range studied. They found that the rate of increase of ignition delay with decreasing temperature appeared to change around 1000 K. Vranckx et al. [62] further developed the low-temperature oxidation mechanism of n-butanol by performing experiments between 61 bar to 92 bar and 795 K to 1200 K and updating a kinetic model with a butyl-peroxy sub-mechanism. They showed improved agreement with predictions of low-temperature butanol ignition delays, but incorrectly predicted the existence of two-stage ignition phenomena.

Zhu et al. [63] measured the ignition delays of n-butanol in a ST using a newly developed technique known as constrained reaction volume (CRV). In traditional ST experiments, it is difficult to measure ignition delays longer than approximately 1 ms to 10 ms because fluid-dynamic effects and other phenomena invalidate the assumptions typically used to calculate the thermodynamic state. In the CRV strategy, the reactants are effectively limited to a small region in the ST ensuring that the conditions under which ignition occurs are constant enthalpy/nearly constant pressure and are well characterized for longer time scales than in traditional ST experiments. Zhu et al. [63] were thus able to measure ignition delays of n-butanol between temperatures of 716 K to 1121 K, pressures

7

of 20 atm and 40 atm, and equivalence ratios of $\phi = 0.5$, 1.0, and 2.0. Using the CRV strategy and constant enthalpy/constant pressure modeling assumptions, Zhu et al. [63] demonstrated that one recent kinetic model was able to accurately predict the ignition delay of n-butanol for most of the conditions they studied.

Ignition delay experiments of the butanol isomers have also been performed in RCMs. Weber et al. [64] studied the ignition delays of n-butanol for low- to intermediate-temperature conditions between 675 K to 925 K, pressures of 15 bar and 30 bar, and equivalence ratios of $\phi = 0.5$, 1.0, and 2.0. Weber et al. [64] found no evidence of two-stage ignition or non-Arrhenius behavior in their results. Weber et al. [64] also found that models available until the time of their work (2011) were unable to predict the ignition delays of n-butanol, over-predicting the ignition delay by approximately one order of magnitude. Subsequently, Weber and Sung [65] extended their study to the other isomers of butanol, covering temperatures between 715 K to 910 K, pressures of 15 bar and 30 bar, and the stoichiometric equivalence ratio. Results from the study by Weber and Sung [65] are presented in Chapter 3. In summary, Weber and Sung [65] found that the order of reactivity—in terms of the inverse of ignition delay—of the butanol isomers changed when the pressure was changed from 15 to 30 bar. Moreover, Weber and Sung [65] found unique pre-ignition heat release behavior during the ignition of t-butanol that was not present during the ignition of the other isomers.

Weber et al. [66] studied the autoignition of i-butanol at three mixture conditions, including $\phi = 0.5$ with air as the oxidizer and $\phi = 0.5$ and 2.0 where the O_2:N_2 ratio in the oxidizer was changed while the fuel mole fraction was held constant to change the equivalence ratio. Weber et al. [66] found that a newly developed kinetic model for i-butanol combustion was able to predict the stoichiometric (from the work of Weber and Sung [65]) and lean ignition delays in air, but was unable to capture the dependence of the ignition delays on the initial oxygen concentration. In addition, Zhu et al. [63] and Weber et al. [64] noted similar inability to predict the dependence of ignition delay on initial oxygen concentration for n-butanol for several different kinetic mechanisms.

Karwat et al. [67] studied the ignition delays of n-butanol for stoichiometric mixtures over temperatures from 920 K to 1040 K and pressures near 3 atm. Karwat et al. [67] found good agree-

ment of the ignition delays with the kinetic model developed in the study of Black et al. [56]. In addition, Karwat et al. [67] used a high-speed sampling valve to remove gas samples from the reaction chamber during the induction period of n-butanol ignition. They quantified mole fractions of CH_4, CO, C_2H_4, C_3H_6, C_2H_4O, C_4H_8O, 1-C_4H_8, and n-butanol at several times during the ignition. Comparison of the time histories of these species with predictions from the model by Black et al. [56] showed that, although the model was able to predict the ignition delay well, it was not able to reproduce the time history of species concentrations very well, particularly C_2H_4. This result demonstrates the importance of rigorously validating a kinetic model over a wide range of conditions and for a wide range of validation targets.

In comparison to the butanol isomers, i-pentanol has received significantly less focus in the literature. Studies of the combustion of i-pentanol have been conducted in jet stirred reactors (JSRs) [73–75], low-pressure flow reactors [76], counterflow flame experiments [75], STs [75, 77, 78], and RCMs [75, 77]. Other studies have investigated the efficacy of using i-pentanol in a homogeneous charge compression iginition (HCCI) engine [79–81]. Finally, studies described in this work have been conducted to determine the ignition properties of i-pentanol (see Chapter 4). Both the works by Sarathy et al. [75] and Tsujimura et al. [77] developed detailed kinetic models for the combustion of i-pentanol whose validation was based, in part, on ignition delay experiments. Using STs and RCMs in concert, these studies were able to provide ignition delays for temperatures, pressures, and equivalence ratios of $650\,K$ to $1450\,K$, $7\,bar$ to $60\,bar$, and $\phi = 0.5$, 1.0, and 2.0, respectively. These studies generally found good agreement of their models with their validation data sets, although Sarathy et al. [75] found that their model had difficulty predicting rich ignition delays. In addition, substantial pre-ignition heat release was observed for all of the equivalence ratios at $40\,bar$ in the RCM measurements, similar to t-butanol.

1.3 Recent Work on Ignition of Methylcyclohexane

Several studies have suggested the use of methylcyclohexane (MCH) as a component in surrogate formulations [18, 19], as discussed previously. Furthermore, MCH is the simplest branched or substituted cycloalkane, and can therefore provide a base from which to build models of the combustion of other, larger naphthenes.

Substantial experimental and modeling work has been conducted for napthenes in general, and MCH in particular. Pitz and Mueller [11] conducted an extensive review of the work on naphthenes, so only studies involving homogeneous ignition of MCH are discussed here. Ignition delays of MCH have been measured in STs [82–87] and RCMs [14, 88, 89] by a number of researchers. These studies collectively cover the temperature-pressure space in the range of 700 K to 2100 K and 1 atm to 70 atm. To complement this experimental work, a number of kinetic models for MCH combustion have been constructed, notably by Pitz et al. [14] and Orme et al. [86].

The study of Rotavera and Petersen [82] measured ignition delays of MCH behind reflected shock waves near 1 atm and 10 atm for equivalence ratios of $\phi = 0.5$, 1.0, and 2.0. They compared their measured ignition delays with predictions from the model of Pitz et al. [14] and found generally good agreement. Hong et al. [87] measured ignition delays for conditions of temperature between 1280 K to 1480 K, pressures of 1.5 atm and 3 atm, and equivalence ratios of $\phi = 1.0$ and 0.5. Hong et al. [87] compared their measurements with three mechanisms from the literature, including those by Pitz et al. [14] and Orme et al. [86] and found relatively good agreement for their conditions.

However, other studies have found that the existing models are not able to predict ignition delays at conditions for which they were not validated—that is, the models are not truly predictive. For instance, previous work conducted in an RCM by Mittal and Sung [89] measured the ignition delays of MCH/O_2/N_2/Ar mixtures at pressures of 15.1 bar and 25.5 bar, for three equivalence ratios of $\phi = 0.5$, 1.0, and 1.5, and over the temperature range of 680 K to 840 K. They compared their measured ignition delays to simulated ignition delays computed using the mechanism of Pitz et al. [14] and found that the model substantially over-predicted both the first stage and overall ignition

delay [89]. Moreover, studies conducted in STs by Vasu et al. [83] and Vanderover and Oehlschlaeger [84] came to similar conclusions, which collectively considered conditions between 795 K to 1560 K and 1 atm to 70 atm. Further studies described in Chapter 5 and published in the work of Weber et al. [90] have expanded the validation range of MCH ignition data and substantially improved the predictive ability of kinetic models of MCH combustion.

1.4 Gas Sampling in Rapid Compression Machines

Due to its relevance in predicting the performance of a fuel in existing and advanced engines, ignition delay is a very common measure of the global performance of a kinetic mechanism. Ignition delays for homogeneous systems are typically measured in STs or RCMs, where the effects of fluid motion and turbulence are generally minimized. However, as demonstrated for the case of butanol isomers, *i*-pentanol, and methylcyclohexane, the validation target of ignition delays is necessary but not sufficient to develop truly predictive kinetic models.

Optical methods can offer non-intrusive in-situ measurements of species and temperature during homogeneous ignition events—c.f. the work by Das et al. [91] and Uddi et al. [92] to directly measure the temperature and water number density in the reaction chamber of an RCM using mid-IR laser light absorption and the work by Stranic et al. [70] to perform simultaneous concentration measurements of multiple species in their ST. However, these methods can detect only a limited set of species and require extensive calibration at engine-relevant pressure conditions.

Another avenue to improve the rigor of validation targets is to remove samples from the reacting gas and analyze them ex-situ. Work on this avenue began in the early part of the 20th century, to help explain the phenomenon of "knock" in engines. Several researchers developed techniques to remove gas samples from the cylinder of spark-ignition engines. According to Withrow et al. [93], Brooks [94] was the first to develop a system to withdraw samples from the cylinder of an oil-injection engine around 1922. Subsequently, Withrow et al. [93], Callendar [95], Egerton and Gates [96], Lovell et al. [97], Ricardo and Thornycroft [98], Steele [99], Egerton et al. [100], Downs

et al. [101], and Pahnke et al. [102] further developed these systems for sampling from the cylinder of spark-ignition engines.

In 1961, Roblee [103] adapted a sampling device to an RCM for the first time. The design of this sampling apparatus was such that the entire reaction chamber could be quickly evacuated to an expansion chamber through a punctured diaphragm. The diaphragm was ruptured either by pressure difference between the reaction chamber and the expansion chamber, or by a spring-actuated knife. Upon diaphragm rupture, the gases in the reaction chamber rushed into the expansion chamber, generating a shock wave that propagated further into the expansion chamber. Simultaneously, a rarefaction wave was generated that propagated backwards into the combustion chamber, expanding the gases therein and quenching any ongoing reactions. After quenching, the products were transferred to a gas chromatograph for analysis.

Roblee [103] used this apparatus to study the decomposition of benzene during the induction period. Roblee [103] noted that minimal consumption of benzene and oxygen occurred during the induction period. Using a similar technique, but in a different RCM, Martinengo et al. [104] measured the products of the decomposition of *i*-octane and *n*-octane at temperatures ranging from 600 K to 700 K and pressures between 15 atm to 20 atm. Martinengo et al. [104] noted that the main intermediate species they measured were alkenes and carbonyl compounds under these conditions, and that CO was produced nearly simultaneously with the final stage of ignition.

Affleck and Fish [105] used a wide-aperture, electronically-triggered valve to effect sampling from their RCM. The valve was triggered after the first stage of ignition of 2-methylpentane, and the sample was quenched by adiabatic cooling through expansion into a large sampling chamber. Affleck and Fish [105] also compared the composition of the samples from high-pressure experiments in the RCM with samples drawn from low-pressure ignition experiments conducted in Pyrex bulbs. The authors noted that the products were largely similar between the two experiments, despite the wide variation in pressure.

Beeley et al. [106] used the diaphragm-puncture method to analyze the reaction intermediates during the pyrolysis and combustion of isopropyl nitrate. The results from the pyrolysis indicated

that the breakdown of the fuel did not lead to chain branching and thus ignition, whereas when oxygen was added, chain branching pathways were available and hot ignition was observed.

The group at the Université des Sciences et Technologies de Lille in France has conducted a number of studies using a sampling apparatus fitted to their RCM [107–111]. These studies have measured the concentration of intermediate species during the ignition of *n*-butane, *n*-heptane, *i*-octane, cyclohexane, cyclohexene, and cyclohexa-1,3-diene. The sampling system used in these studies is similar to that developed by Roblee [103] in that it uses an expansion chamber separated from the reaction chamber by a diaphragm that is punctured by a knife at the appointed time.

Using a gas chromatograph coupled to a mass spectrometer to analyze their samples, Minetti et al. [107] were able to identify approximately 25 species produced during the autoignition of *n*-butane. These species included several cyclic ethers produced during the low-temperature oxidation process through peroxy species. Minetti et al. [107] noted that a kinetic model for the combustion of *n*-butane was able to accurately reproduce the major species profiles, but was unable to predict the mole fractions of several minor species.

Minetti et al. [108] studied the species produced during autoignition of *n*-heptane and found that, although a detailed kinetic model was able to correctly predict the ignition delays, it was unable to capture the concentration profiles of the major species, including *n*-heptane and its oxidation products. Minetti et al. [109] compared the oxidation products of *n*-heptane with *i*-octane under conditions of similar ignition delay. The authors noted that the kinetic scheme for two-stage ignition for the two fuels was similar in the sense that the important reaction classes were the same; however, the species produced by the two fuels were largely different.

Lemaire et al. [110] and Ribaucour et al. [111] studied the concentration of intermediate species during autoignition of cyclohexane, cyclohexene, and cyclohexa-1,3-diene. Lemaire et al. [110] noted that cyclohexane was prone to the same autoignition phenomena as acyclic alkanes, namely two-stage ignition at low temperatures, followed by a region of negative temperature dependence of the ignition delay as the temperature increases, and finally, single stage ignition at high temperatures. They further observed that cyclohexa-1,3-diene did not exhibit such behavior. Lemaire et al. [110]

also compared the species present during the autoignition and found that cyclohexane showed many of the same species as acyclic alkane ignition, whereas cyclohexa-1,3-diene did not have such species. Cyclohexene showed behavior intermediate between cyclohexane and cyclohexa-1,3-diene, both in terms of the ignition behavior and the species concentrations.

Ribaucour et al. [111] studied the autoignition of cyclohexene and constructed a detailed model for its oxidation. They found two primary reaction pathways, one involving the double bond and the other involving peroxy radicals, during the ignition period and also noted that effects from the ring structure and the double bond combined to produced the observed chemistry.

More recently, He [112] at the University of Michigan and Mittal [113] at Case Western Reserve University developed sampling systems for their rapid compression devices. Mittal and Sung [114] demonstrated the feasibility of their sampling apparatus by measuring the major species during the induction period of methane ignition. To date, no further results have been presented from this sampling apparatus.

The system developed by He [112] at the University of Michigan for their Rapid Compression Facility (RCF) is a unique design in that it quenches only a small portion of the reactants from the reaction chamber instead of quenching the entire chamber. A small diameter tube protrudes into the reaction chamber through which samples are drawn into a large expansion chamber. The sampling time is controlled by a fast-acting solenoid valve located outside the reaction chamber that is triggered based on the position of the piston in the RCF and a delay timer.

The local sampling technique developed by He [112] has several important advantages compared to the global sampling techniques used in previous work. In particular, capturing the entire reaction chamber also captures the boundary layer near the chamber walls, potentially causing significant dilution of the test sample. By capturing only a small sample from the center of the reaction chamber, the boundary layer and attendant dilution can be avoided. In addition, the local sampling technique does not substantially disturb the ongoing reactions, meaning that the ignition process is allowed to proceed unhindered.

Nonetheless, the local sampling technique has some disadvantages. Notably, the presence of

dead volume in the sampling system can impact the quantification of species in a manner similar to the capture of the boundary layer in global sampling techniques. In particular, the dead volume will have a much lower temperature than the core gases due to the large surface-area-to-volume ratio, which prevents reactions from occurring in the dead volume.

He et al. [115] used this sampling system to study the oxidation products developed during the autoignition of *i*-octane and noted that comparison to a detailed kinetic model developed after the work of Minetti et al. [109] showed agreement within a factor of two for most species. For the species that showed larger disagreement, the authors were able to use their results to suggest several alternate oxidation pathways that were not included in the model.

Subsequently, Walton [116] upgraded the sampling system at the University of Michigan to reduce the dead volume and improve the response time. Walton et al. [117] used the upgraded system to study the intermediate species in the oxidation of methyl butanoate. The authors found that a kinetic model was able to well predict the concentration profiles of the several species, although larger disagreement was noted for propene.

Karwat et al. [67, 118, 119] used the upgraded sampling system to study the autoignition chemistry of *n*-butanol [67], *n*-heptane/*n*-butanol blends [118], and *n*-heptane [119] (the results for *n*-butanol have been described previously). Karwat et al. [118] demonstrated that the reactivity of *n*-heptane was reduced when blended with *n*-butanol, and moreover that the fundamental reaction pathways of *n*-heptane were changed by the addition of *n*-butanol. A kinetic model over-predicted the consumption of *n*-heptane during the first stage of ignition, and was thus unable to reproduce many of the species profiles for the duration of the induction period. Karwat et al. [119] further used species sampling measurements of pure *n*-heptane, combined with newly calculated reaction rate constants for alkylperoxy reactions from the literature, to improve a kinetic model of *n*-heptane combustion, although they did not compare the updated model to their blending results.

1.5 Summary

The works presented in the previous sections represent a large volume of validation data for kinetic models, and have greatly expanded our understanding of the combustion chemistry of alternative fuels. Nonetheless, gaps in the state of the art knowledge have been revealed through several experimental studies, gaps that prevent the development of truly predictive kinetic models—for example, the inability of models to predict the oxygen concentration dependence of ignition delays is still unexplained.

Thus, the major objectives of this work can be stated succinctly as follows:

1. Generate ignition delay datasets for alternative fuels at high-pressure, low-temperature conditions that have not been studied extensively in previous work

2. Develop and characterize a new experimental apparatus to enable ex-situ species measurements from the reaction chamber of the RCM during the ignition delay

3. Use the data acquired from Item 1 and Item 2 to extend the validation of new and existing chemical kinetic models for the combustion of alternative fuels

4. Analyze new and existing chemical kinetic models to help understand the cause of discrepancies and clarify the important reaction pathways in high-pressure alternative fuel ignition

1.6 Organization of this Work

The bulk of what follows has been published in the archival literature, and the preceding introduction has primarily been taken from those papers (and includes a summary of some results from the following chapters). In addition, much of Chapter 2 has been taken from the published work. Chapter 2 presents an introduction to the RCM and other facilities used in the experiments described in subsequent chapters, including the fast sampling system that was newly developed for this work. Detailed uncertainty analyses are also considered for the appropriate apparatuses.

The subsequent chapters are organized by the fuel studied: Chapter 3 considers the butanol isomers and was published in *Energy & Fuels* [65]; Chapter 4 considers *i*-pentanol and was published in *Combustion and Flame* [75]; Chapter 5 considers methylcyclohexane and was published in *Combustion and Flame* [90]. Finally, Chapter 6 presents conclusions based on this work and recommendations for future directions.

The works published in or submitted to the archival literature during the course of this program are as follows:

Weber, B.W., Kumar, K., Zhang, Y., and Sung, C.-J. "Autoignition of *n*-butanol at elevated pressure and low-to-intermediate temperature." *Combust. Flame*, vol. 158, no. 5 (Mar. 2011), pp. 809–819. DOI: 10.1016/j.combustflame.2011.02.005.

Tsujimura, T., Pitz, W. J., Gillespie, F., Curran, H. J., Weber, B. W., Zhang, Y., and Sung, C.-J. "Development of Isopentanol Reaction Mechanism Reproducing Autoignition Character at High and Low Temperatures." *Energy Fuel*, vol. 26, no. 8 (Aug. 2012), pp. 4871–4886. DOI: 10.1021/ef300879k.

Weber, B. W. and Sung, C.-J. "Comparative Autoignition Trends in Butanol Isomers at Elevated Pressure." *Energy Fuel*, vol. 27, no. 3 (Mar. 2013), pp. 1688–1698. DOI: 10.1021/ef302195c.

Sarathy, S. M., Park, S., Weber, B. W., Wang, W., Veloo, P. S., Davis, A. C., Togbé, C., Westbrook, C. K., Park, O., Dayma, G., Luo, Z., Oehlschlaeger, M. A., Egolfopoulos, F. N., Lu, T., Pitz, W. J., Sung, C.-J., and Dagaut, P. "A comprehensive experimental and modeling study of iso-pentanol combustion." *Combust. Flame*, vol. 160, no. 12 (Dec. 2013), pp. 2712–2728. DOI: 10.1016/j.combustflame.2013.06.022.

Weber, B. W., Pitz, W. J., Mehl, M., Silke, E. J., Davis, A. C., and Sung, C.-J. "Experiments and modeling of the autoignition of methylcyclohexane at high pressure." *Combust. Flame*, (Feb. 2014), In Press. DOI: 10.1016/j.combustflame.2014.01.018.

Burke, S., Burke, U., Mathieu, O., Osorio, I., Keesee, C., Morones, A., Petersen, E. L., Wang, W., DeVerter, T., Oehlschlaeger, M. A., Rhodes, B., Hanson, R. K., Davidson, D. F., Weber, B. W., Sung, C.-J., Santner, J., Ju, Y., Haas, F. M., Dryer, F. L., Volkov, E., Nilsson, E., Konnov, A., Alrefae, M., Khaled, F., Farooq, A., Dirrenberger, P., Glaude, P.-A., and Battin-Leclerc, F. "An Experimental and Modeling Study of Propene Oxidation. Part 2: Ignition Delay Time and Flame Speed Measurements." *Combust. Flame*, (Submitted).

Chapter 2

Experimental Facilities

2.1 Rapid Compression Machine

2.1.1 Experimental Procedure

The studies in this dissertation were conducted using the Rapid Compression Machine (RCM) constructed by Mittal around 2005 and described in the work of Mittal [113] and Mittal and Sung [114]. This RCM has been used to study the autoignition behavior of a number of fuels, including *n*-decane, methylcyclohexane, hydrogen, syngas, dimethyl ether, methanol, toluene, benzene, di-isobutylene, iso-octane, jet fuel, and gasoline [12, 89, 91, 120–132], in addition to the studies presented in this work.

A modern RCM operates by rapidly compressing (hence the name) a test gas mixture to targeted pressure and temperature conditions. The compression is effected by either a single piston or dual, opposed pistons. Upon reaching the targeted state, the piston (or pistons) is stopped and fixed in place so that the reactions proceed in a constant volume reactor. When studying autoignition with an RCM, the primary data are the measured pressure traces during and after the compression stroke. These pressure traces are processed to derive information such as the pressure and temperature at the end of compression (EOC) and the ignition delay. It is also possible to employ laser diagnostics

or extract gas samples from the reactor to examine reaction pathways in more detail.

The present RCM is a pneumatically-driven/hydraulically-stopped single-piston arrangement. A schematic of the RCM is shown in Fig. 2.1 and an image is shown in Fig. 2.2. The RCM consists of four chambers and three pistons that are used to control the machine. The chambers are called the reaction chamber, the hydraulic chamber, the pneumatic chamber, and the driving tank; similarly, the pistons are called the reactor, hydraulic, and pneumatic pistons and each is installed in the chamber of the same name. The rear of the reaction chamber is bolted to the front of the hydraulic chamber; seals in the face of the hydraulic chamber prevent oil from leaking into and contaminating the reaction chamber. The driving tank and the rear of the pneumatic chamber are connected by a union; a seal around the circumference of the pneumatic piston seals gas in the driving tank from the front of the pneumatic chamber. Thus, the pneumatic piston can be driven by pressure from the driving tank on its rear and pressure from the pneumatic chamber on its front. The three pistons are connected by a rod running from the front of the pneumatic piston to the rear of the reactor piston so that they move as one; this will be referred to as the piston assembly.

At the start of an experimental run, with the piston in the EOC position, the reaction chamber is vacuumed to less than 1 torr. Next, the piston assembly is retracted by pressurizing the front face of the piston in the pneumatic chamber. For safety, and to prevent damage to the RCM, the driving tank is filled to limit the acceleration of the piston assembly during the retraction. The pressure on the front of the pneumatic piston pulls the piston assembly rearward and seats the rear of the hydraulic piston onto an O-ring in the rear of the hydraulic chamber. The hydraulic chamber is filled with oil to a pressure of approximately 800 psi, providing a rearward force on the front face of the hydraulic piston. The air pressure is released from the front of the pneumatic chamber and the driving tank is filled to the desired driving pressure. The force on the hydraulic piston opposes the force on the pneumatic piston from the driving tank and the piston assembly remains at rest. The reaction chamber is filled with the required initial pressure of test gas mixture from the mixing tank. Finally, compression is triggered by releasing the hydraulic pressure through an electrically-operated solenoid valve. The piston assembly is driven forward by the unbalanced

C:/Users/bww09001/Documents/Github/dissertation/figures/02-Experimental-Facilities/rcm-schematic.pdf

Figure 2.1: Schematic of the RCM. Not to scale

C:/Users/bww09001/Documents/Github/dissertation/figures/02-Experimental-Facilities/rc

Figure 2.2: Photograph of the RCM.

force from the pressure in the driving tank on the pneumatic piston. The gases in the reaction chamber are brought to the compressed pressure (P_C) and compressed temperature (T_C) conditions in approximately 30 ms to 50 ms.

The required driving pressure for a given EOC pressure can be estimated from a force balance between the force on the pneumatic piston from the driving tank and the force on the reactor piston from the test gases, as shown in Eq. (2.1c).

$$P_{d,\text{min}} \cdot A_p = P_{r,\text{EOC}} \cdot A_r \tag{2.1a}$$

$$P_{d,\text{min}} \cdot \frac{\pi d_p^2}{4} = P_{r,\text{EOC}} \cdot \frac{\pi d_r^2}{4} \tag{2.1b}$$

$$P_{d,\text{min}} = P_{r,\text{EOC}} \cdot \frac{d_r^2}{d_p^2} \tag{2.1c}$$

In Eq. (2.1), $P_{d,\text{min}}$ is the minimum driving pressure, A_p is the cross-sectional area of the pneumatic piston, $P_{r,\text{EOC}}$ is the pressure in the reactor at the EOC (i.e. P_C), A_r is the cross-sectional area of the reactor piston, d_p is the diameter of the pneumatic piston, and d_r is the diameter of the reactor piston.

The minimum driving pressure is such that the piston does not rebound at the EOC due to pressure on the reactor piston. So that the driving pressure can be much lower than the EOC pressure, the diameter ratio of the reactor piston to the driver piston is 2:5, allowing the driving pressure to be lower than the EOC pressure by a factor of 6.25. The actual driving pressure should

22

exceed the minimum by some safety margin so that the reactor remains at constant volume even if there is some pressure rise due to heat release in the reaction chamber prior to the main ignition.

There is not a theoretical upper limit on the driving pressure. It is desired that the piston should reach the EOC conditions in as short a time as possible to minimize heat loss from the reactants to the reactor walls and minimize the time for reactions to occur during the compression stroke. This implies that the driving pressure should be made as high as possible so that the highest piston velocity is achieved. However, higher piston velocities require a higher deceleration at the EOC. In the present RCM, the deceleration is provided by venting the hydraulic oil between steps on the hydraulic piston and matched steps on the front of the hydraulic chamber. If the piston is overdriven—that is, the driving pressure is too high—the piston will not be sufficiently decelerated by the oil venting and will impact the front of the hydraulic chamber at high velocity. This can damage the RCM and cause the piston to rebound elastically. It also generates substantial noise in the pressure trace and should be avoided.

Typical driving gas pressures are between $50\,\mathrm{psi}$ for $P_C = 15\,\mathrm{bar}$ experiments to $125\,\mathrm{psi}$ for $P_C = 50\,\mathrm{bar}$ experiments. These driving pressures represent a good compromise between the minimum required for no rebound at EOC due to pressure and no rebound at EOC due to elastic reaction. Nonetheless, a small amount of piston rebound can be expected during/after the main ignition event. This small rebound may have an effect on the computation of ignition delay if it reduces the pressure rise rate during the ignition; it is expected that this effect will be very small relative to the typical random uncertainty in ignition delay experiments. Moreover, the driving pressures required to balance the full pressure rise during ignition are more likely cause elastic rebound, especially for high P_C when the post-ignition pressure rise is greater.

The EOC conditions (P_C and T_C) can be independently varied. This is made possible by independent variation of the compression ratio, initial pressure and initial temperature, and the specific heat ratio of the test gases. The compression ratio can be increased by adding spacers onto the rear of the hydraulic chamber or increasing the stroke, and can be reduced by adding split shims onto the rear of the reaction chamber or increasing the EOC clearance length. Adjustment of the specific

heat ratio of the gas can be accomplished by substituting components (e.g. substituting Ar for N_2 results in higher P_C and T_C if all other conditions are fixed). The initial temperature is controlled by heaters, as described in the following section.

2.1.2   Test Gas Mixture Preparation

Fuel/oxidizer pre-mixtures are prepared in two mixing tanks, one approximately 17 L and the other approximately 15 L in volume. These large volumes allow many runs to be conducted from one mixture preparation. The mixing tanks are connected to the reaction chamber by flexible stainless steel manifold tubing. The tanks, reaction chamber, and connecting manifold are wrapped in heating tape and insulation to control the initial temperature of the mixture. Temperature controllers from Omega Engineering use thermocouples placed on the lid of each mixing tank, approximately in the center of each mixing tank, embedded in the wall of the reaction chamber, and near the inlet valve of the reaction chamber to control the preheat temperature of the mixture. A static pressure transducer measures the pressure in the manifold and mixing tanks. This transducer is used during mixture preparation and to measure the initial pressure of a given experiment. Two transducers are used for various experiments in this work, as described below in Sec. 2.1.8.2.

Most of the fuels studied in this work are liquids at room temperature and pressure and have relatively low vapor pressure. A similar procedure, outlined below, was used for all of the butanol isomers, *iso*-pentanol, and methylcyclohexane; specific procedures are given in the chapter relevant to each fuel. First, the mixing tanks are vacuumed to an ultimate pressure less than 5 torr. The liquid fuel is massed in a syringe to a precision of 0.01 g prior to injection through a septum. Proportions of O_2, N_2, and Ar are added manometrically at room temperature. The preheat temperature of the RCM is set above the saturation point for each fuel to ensure complete vaporization. The vapor pressure as a function of temperature is calculated according to fits taken from Yaws [133]. A magnetic stirrer mixes the reactants. The temperature inside the mixing tank is allowed to equilibrate for approximately 1.5 h.

This approach to mixture preparation has been validated in several previous studies by withdraw-

ing gas samples from the mixing tank and analyzing the contents by GC/MS [64], GC-FID [120], and GC-TCD [91]. These studies have verified the concentration of *n*-butanol, *n*-decane, and water, respectively. In addition, both the work by Kumar et al. [120] on *n*-decane and the study of Weber et al. [64] on *n*-butanol confirmed that there was no fuel decomposition over the course of a typical set of experiments. Furthermore, each new mixture preparation is checked against previously tested conditions to ensure reproducibility.

2.1.3 Definition of Ignition Delay

The pressure in the reaction chamber during an experiment is monitored by a Kistler 6125B piezoelectric dynamic pressure transducer. The charge signal from the transducer is amplified and converted to a voltage by a Kistler 5010B charge amplifier. The voltage is sent to a National Instruments cDAQ equipped with the NI-9215 module. The signal is recorded by a LabView VirtualInstrument at 50 kHz.

Figure 2.3 shows a representative pressure trace from these experiments with methylcyclohexane (MCH) at $P_C = 50$ bar, $T_C = 761$ K, and $\phi = 1.5$ (See Chapter 5). Note that Fig. 2.3 shows a case with two stages of ignition; not all of the fuels studied had conditions that showed two-stage ignition. Nonetheless, the ignition delay is consistently defined in all the work in this study. The definitions of the EOC and the ignition delays are indicated on the figure. The end of compression time is defined as the time when the pressure reaches its maximum before first stage ignition occurs, or for cases where there is no first stage ignition, the maximum pressure before the overall ignition occurs. The first stage ignition delay is the time from the end of compression until the first peak in the time derivative of the pressure. The overall ignition delay is the time from the end of compression until the largest peak in the time derivative of the pressure.

Each unique P_C and T_C condition is repeated at least 5 times to ensure repeatability of the experiments. The experiment closest to the mean of the runs at a particular condition is chosen for analysis and presentation. The standard deviation of all of the runs at a particular condition is less than 10 % of the mean in all cases. The uncertainty of the ignition delay at each condition is

25

C:/Users/bww09001/Documents/Github/dissertation/figures/02-Experimental-Facilit

Figure 2.3: Representative pressure trace indicating the definition of the first stage and overall ignition delays and the corresponding non-reactive pressure trace. EOC stands for End of Compression.

estimated as twice the standard deviation of all the runs at a particular condition.

2.1.4   Non-Reactive Experiments

Figure 2.3 also shows a representative non-reactive pressure trace corresponding to the experimental conditions in the figure. Due to heat loss from the test mixture to the cold reactor walls, the pressure and temperature of the gas in the reaction chamber will decrease after the end of compression. A non-reactive pressure trace is measured that corresponds to each unique P_C and T_C condition studied to quantify the effect of the heat loss on the ignition process and to verify that no heat release has occurred during the compression stroke. The non-reactive pressure trace is acquired by replacing the O_2 in the oxidizer with N_2, so that the specific heat ratio of the initial mixture is maintained, but the heat release due to exothermic oxidation reactions is eliminated. Maintaining a similar specific heat ratio ensures that the non-reactive experiment faithfully reproduces the conditions of the reactive experiment.

2.1.5 Reaction Chamber Homogeneity

An RCM to be used for studies of homogeneous chemistry—as in this study—must ensure that homogeneous conditions exist inside the reaction chamber for the duration of the experiment. Due to the high piston velocities required to minimize heat loss and reaction during the compression stroke, complex fluid mechanical effects can strongly affect the state of the reactants at the EOC. The most important of these effects is caused by the motion of the piston itself, where the piston pushes the wall boundary layer into a roll-up vortex [134]. This cold vortex mixes with the hotter gases near the center of the reaction chamber and causes large spatial inhomogeneities of temperature and species.

To facilitate spatially homogeneous conditions in the reactor and reduce the effect of the roll-up vortex, it is necessary to trap the boundary layer. This is accomplished in the present RCM by a crevice machined into the crown of the piston, shown in cross-section in Fig. 2.4. The boundary layer enters the crevice through the converging section as the piston moves forward and is trapped within the crevice. The dimensions of the crevice were optimized by Mittal [113] through computational fluid dynamic (CFD) simulations. Subsequently, Mittal and Sung [135] experimentally showed that the optimized crevice design provided homogeneous conditions in the reaction chamber up to approximately 150 ms after the EOC. By using planar laser induced fluorescence (PLIF) measurements of acetone-seeded mixtures, Mittal and Sung [135] showed that there was a core region of gases near the center of the reactor whose temperature remained spatially homogeneous.

2.1.6 Determination of Reactant Temperature

In general, it is rather difficult to directly measure the temperature of the gases in the reaction chamber during and after compression. Intrusive methods such as thermocouples may introduce inhomogeneities into the reaction chamber and non-intrusive optical techniques are difficult to set up and require extensive calibration at the pressures of interest in RCM studies. Thus, the temperature is determined indirectly by applying an assumption called the "adiabatic core hypothesis" to the reaction chamber [114, 134].

Figure 2.4: Creviced piston installed in the present RCM.

If all of the gases in the reaction chamber were compressed isentropically, the temperature at the end of compression could be found by the following relations:

$$\ln(\text{CR}) = \int_{T_0}^{T_{ic}} \frac{1}{T(\gamma - 1)} \, dT \tag{2.2a}$$

$$\ln\left(\frac{P_{ic}}{P_0}\right) = \int_{T_0}^{T_{ic}} \frac{\gamma}{T(\gamma - 1)} \, dT \tag{2.2b}$$

where CR is the volumetric compression ratio, T_0 is the initial temperature, T_{ic} is the temperature at the end of isentropic compression, γ is the temperature-dependent ratio of specific heats, P_{ic} is the pressure at the end of isentropic compression, and P_0 is the initial pressure.

However, experiments have shown that the measured pressure in the reaction chamber does not reach the value of P_{ic} calculated by using the geometric compression ratio. The difference is due to finite heat loss from the reactants to the reactor walls and the crevice volume during the compression. Under the adiabatic core hypothesis, it is assumed that the heat loss from the reactants only occurs in a thin boundary layer near the wall, and the central core region is unaffected by heat

loss (i.e. the core is adiabatic) [136]. Thus, the heat loss is modeled as an effective reduction in the compression ratio, and the temperature during the compression stroke can be calculated by:

$$\ln\left(\frac{P_C}{P_0}\right) = \int_{T_0}^{T_C} \frac{\gamma}{T(\gamma - 1)} \, dT \qquad (2.3)$$

where P_C is the measured pressure at the end of compression, T_C is the temperature at the end of compression, and the other variables are the same as in Eq. (2.2).

After the end of compression, the pressure in the reaction chamber decreases, as can be seen in Fig. 2.3. This pressure decrease is caused by heat loss from the reactants in the constant volume reaction chamber and is accompanied by a decrease in the temperature of the reactants. To model the thermodynamic state after the end of compression, the adiabatic core hypothesis is applied and the heat loss is assumed to occur only in a thin boundary layer near the reactor walls. Thus, the core region is modeled as adiabatic, and the heat loss from the boundary layer is modeled as an isentropic volume expansion.

In general, the specific heat ratio used in Eqs. (2.2) and (2.3) is an unknown function of temperature and composition, so Eq. (2.3) cannot be integrated directly to find T_C. If the specific heats are parameterized with a linear fit and the composition is assumed to be fixed, it is possible to integrate Eq. (2.3) directly, but this process is quite tedious; nonetheless, it will be applied in Sec. 2.1.8 to determine the uncertainty of T_C. In general, the simplest method of calculating T_C is to use software to numerically integrate Eq. (2.3).

In this work, the CHEMKIN-Pro [137] software is used to perform the numerical integration and calculation of T_C. The CHEMKIN-Pro software provides the facility for a user-specified volume profile as a function of time to be applied to a homogeneous, adiabatic reactor. Since the adiabatic core of the reaction chamber is modeled as undergoing an isentropic volumetric compression followed by an isentropic volumetric expansion, this user-specified volume functionality is used to compute the RCM reactor state as a function of time in CHEMKIN-Pro.

A volume trace for simulation is computed from the measured pressure trace using the isentropic

relation:

$$\frac{V_2}{V_1} = \left[\frac{P_1}{P_2}\right]^{\frac{1}{\gamma}} \tag{2.4}$$

where V_1 and V_2 are the volumes at consecutive time points, P_1 and P_2 are the pressures at consecutive time points, and γ is the temperature dependent specific heat. This equation is applied during and after the compression stroke to calculate the volume trace. Since the non-reactive experiment requires slightly different initial pressure (typically on the order of 5 torr) to reach the same compressed pressure as the reactive experiment—due to the slightly different specific heat ratio in the non-reactive experiment compared to the reactive experiment—the reactive pressure trace is used to compute the volume trace until EOC; after EOC, the corresponding non-reactive pressure trace is used. In Eq. (2.4) it is assumed that changes in composition of the reactants are negligible during the compression stroke, which is confirmed by comparing simulations with and without reaction steps in the chemical kinetic model. The EOC conditions are the same in both cases. The initial volume is arbitrarily taken to be equal to 1.0.

For use in Eq. (2.4), the temperature-dependent specific heat ratio γ is tabulated for each time point. Thus, the temperature at each time point must also be computed by using the isentropic relation for temperature:

$$\frac{T_2}{T_1} = \left[\frac{P_2}{P_1}\right]^{\frac{\gamma-1}{\gamma}} \tag{2.5}$$

where T_2 and T_1 are the temperatures at consecutive time points. Since T_2 depends on the value of γ, which in turn depends on T_2, Eq. (2.5) is iterated until the temperature changes by less than one tenth of one percent on consecutive iterations. Once again, it is assumed that changes in composition have a negligible influence on the ratio of specific heats. The temperature calculated by Eq. (2.5) is typically within 1K of the temperature calculated by CHEMKIN-Pro.

CHEMKIN-Pro expects the volume profile in a tabular format, with each row containing the

volume at a specified time. For ease of import, the `csv` file format is used. Since the volume is computed at each point that the pressure is experimentally measured (i.e. at a rate of 50 kHz), every fifth volume point is selected for tabulation to reduce the computation time in CHEMKIN-Pro.

2.1.7   Numerical Methods

Two types of simulations are conducted using the Closed Homogeneous Batch Reactor in CHEMKIN-Pro [137]. The first type uses the tabulated volume profile and is specified in the CHEMKIN-Pro input file with the VPRO keyword. Therefore, this type of simulation is referred to as a VPRO simulation hereafter. The second type is a constant volume, adiabatic simulation and is referred to as CONV hereafter, again named after the CHEMKIN-Pro input keyword used to specify this problem type. The CONV type simulations do not capture the effect of the compression stroke and post-compression heat loss; therefore, they allow direct analysis of the kinetic model with no influence of potentially confounding experimental effects.

As mentioned previously, VPRO simulations are used to calculate the temperature at the end of compression, T_C. This temperature is used as the reference temperature for reporting the ignition delay. Simulations to determine TC are conducted with and without detailed reaction steps to determine if there is significant reactivity in the compression stroke. If there is no significant reactivity (and hence heat release), the pressure and temperature at EOC are the same whether or not reactions are included in the simulation.

2.1.8   Uncertainty of Compressed Temperature

The uncertainty of the compressed temperature is an important parameter to report. Since T_C is not measured, we must perform an uncertainty propagation analysis on the equation used to calculate T_C, Eq. (2.3). First, we simplify the term involving γ in Eq. (2.3). By definition, γ is the ratio of the

specific heat at constant pressure to that at constant volume:

$$\gamma \equiv \frac{C_p}{C_v} = \frac{C_p/R}{C_v/R} = \frac{\hat{C}_p}{\hat{C}_v} \tag{2.6}$$

where C_p and C_v are the specific heats in molar units at constant pressure and volume, respectively, and R is the universal gas constant, used to produce non-dimensional specific heats, indicated by a hat. The difference between the non-dimensional specific heats is one, $\hat{C}_v = \hat{C}_p - 1$. Then, it follows that:

$$\frac{\gamma}{\gamma - 1} = \frac{\frac{\hat{C}_p}{\hat{C}_v}}{\frac{\hat{C}_p}{\hat{C}_v} - 1} = \frac{\frac{\hat{C}_p}{\hat{C}_p-1}}{\frac{\hat{C}_p}{\hat{C}_p-1} - 1} = \frac{\frac{\hat{C}_p}{\hat{C}_p-1}}{\frac{1}{\hat{C}_p-1}} = \hat{C}_p \tag{2.7}$$

In Eq. (2.3), the total specific heat ratio for the mixture should be used; thus, the simplification as shown in Eq. (2.7) requires that the specific heat $\hat{C}_p$ also be the total specific heat. In the following, we assume that there is negligible change of the total specific heat due to changes in reactant mole fractions, as for Eqs. (2.4) and (2.5). The total specific heat is simply the sum of the product of the species mole fractions and their specific heats:

$$C_{p,\text{total}} = \sum_i X_i C_{p,i} \tag{2.8a}$$

$$\hat{C}_{p,\text{total}} = \frac{\sum_i X_i C_{p,i}}{R} \tag{2.8b}$$

where i indicates the species and X_i is the species mole fraction. In the NASA polynomial formulation used by CHEMKIN, the non-dimensional specific heat at constant pressure as a function of temperature is represented by a fourth-order polynomial fit:

$$\hat{C}_{p,i} = c_{1,i} + c_{2,i}T + c_{3,i}T^2 + c_{4,i}T^3 + c_{5,i}T^4 \tag{2.9}$$

In general, this means that the specific heat can be non-linear. However, since the mixtures prepared

in this study are composed primarily of O_2, N_2 and Ar (i.e. no more than 7 % of any mixture is the fuel), and since the specific heats of O_2, N_2 and Ar are only weakly temperature dependent over the range of temperatures experienced during compression, for the purposes of this uncertainty analysis, we will approximate the total specific heat as a linear function of temperature:

$$\hat{C}_{p,\text{total}} = \sum_i X_i \hat{C}_{p,i}$$
$$= \sum_i X_i \left(\sum_{j=1}^{5} c_{j,i} T^{j-1} \right) \tag{2.10}$$
$$\approx a + bT$$

where a and b are found by fitting the total non-dimensional specific heat over the temperature range from 300 K to 1100 K, as discussed below in Sec. 2.1.8.4.

With this approximation of the specific heat, we can integrate Eq. (2.3) to find the compressed temperature:

$$\ln \frac{P_C}{P_0} = \int_{T_0}^{T_C} \frac{\gamma}{T(\gamma - 1)} \, dT \tag{2.11a}$$
$$= \int_{T_0}^{T_C} \frac{\hat{C}_p}{T} \, dT \tag{2.11b}$$
$$= \int_{T_0}^{T_C} \frac{a + bT}{T} \, dT \tag{2.11c}$$
$$= \Big[a \ln T + bT \Big]_{T_0}^{T_C} \tag{2.11d}$$

$$\ln \frac{P_C}{P_0} + (a \ln T_0 + bT_0) = a \ln T_C + bT_C \tag{2.11e}$$

Equation (2.11e) can be solved explicitly for T_C by using Lambert's W function [138], but this function is somewhat complex. Instead, Eq. (2.11e) is simplified by performing a Taylor expansion

of the right hand side and solving for T_C:

$$a \ln T_C + b T_C \approx a \ln T_e + b T_e + \left(\frac{a}{T_e} + b\right)(T_C - T_e) \tag{2.12}$$

$$T_C = \frac{\ln \frac{P_C}{P_0} + a \ln \frac{T_0}{T_e} + b(T_0 - T_e)}{\frac{a}{T_e} + b} + T_e \tag{2.13}$$

where T_e is the temperature about which the Taylor expansion is performed.

With an explicit function for T_C, we can estimate the uncertainty in T_C by the quadratic sum of the uncertainty in the parameters in Eq. (2.13) multiplied by the partial derivative of Eq. (2.13) with respect to each of the parameters [139]. The parameters are P_C, P_0, T_0, a, and b and are assumed to be independent with normally distributed uncertainties.

$$U_{T_C} = \sqrt{\left(\frac{\partial T_C}{\partial P_C} U_{P_C}\right)^2 + \left(\frac{\partial T_C}{\partial P_0} U_{P_0}\right)^2 + \left(\frac{\partial T_C}{\partial T_0} U_{T_0}\right)^2 + \left(\frac{\partial T_C}{\partial a} U_a\right)^2 + \left(\frac{\partial T_C}{\partial b} U_b\right)^2} \tag{2.14}$$

In general, the uncertainties of each parameter may not be normally distributed and several of the parameters are correlated (i.e. not independent), so the following analysis provides only an approximation of the true uncertainty. More detailed analysis (e.g. by a Monte Carlo method) is required to investigate the interactions of the uncertainties.

The uncertainties of the parameters, U_j in Eq. (2.14), are in general found by their own root square sum procedure:

$$U_j{}^2 = B_j{}^2 + R_j{}^2 \tag{2.15}$$

where the subscript j represents one of the parameters in Eq. (2.13). The total uncertainty of a particular parameter is composed of two parts, the systematic or bias uncertainty (B_j) and the precision or random uncertainty (R_j). In general, the bias uncertainty is contained in the measurement equipment and can be reduced, e.g. by using different equipment; the random uncertainty is inherent in any measured process and cannot be reduced by experimental techniques. The bias and precision

uncertainties for each parameter will be discussed in the following sections.

The partial derivatives of Eq. (2.13) with respect to each of the parameters are given in Eq. (2.16):

$$\frac{\partial T_C}{\partial P_C} = \frac{T_e}{P_C\,(a + T_e b)} \tag{2.16a}$$

$$\frac{\partial T_C}{\partial P_0} = \frac{-T_e}{P_0\,(a + T_e b)} \tag{2.16b}$$

$$\frac{\partial T_C}{\partial T_0} = \frac{T_e\,(a + T_0 b)}{T_0\,(a + T_e b)} \tag{2.16c}$$

$$\frac{\partial T_C}{\partial a} = \frac{T_e \left[b \left(T_e \ln \frac{T_0}{T_e} + T_e - T_0 \right) - \ln \frac{P_C}{P_0} \right]}{(a + T_e b)^2} \tag{2.16d}$$

$$\frac{\partial T_C}{\partial b} = -\frac{T_e \left[a \left(T_e \ln \frac{T_0}{T_e} + T_e - T_0 \right) + T_e \ln \frac{P_C}{P_0} \right]}{(a + T_e b)^2} \tag{2.16e}$$

2.1.8.1 Uncertainty in Initial Temperature

The bias uncertainty in the initial temperature is due to the standard limits of error of the K-type thermocouple used to measure the initial temperature. According to the Omega Engineering specifications, this is "the greater of 2.2 °C or 0.75 %". The largest initial temperature used in this work, 413 K, leads to an uncertainty of ± 3 K; thus, $B_{T_0} = 3$ K. Bias uncertainty due to the A/D converter in the process meter is negligible compared to this uncertainty. The precision uncertainty is due to the limit of precision of the display on the Omega Engineering CNi3254 process meter used to control the process temperature. This is ± 0.05 K. The total uncertainty of the initial temperature is:

$$U_{T_0} = \sqrt{\left(B_{T_0}\right)^2 + \left(R_{T_0}\right)^2} = \sqrt{(3\,\text{K})^2 + (0.05\,\text{K})^2} = 3\,\text{K} \tag{2.17}$$

2.1.8.2 Uncertainty in Initial Pressure

The bias uncertainty in the initial pressure is due to the standard error in the pressure transducer used to measure the initial pressure. Two different pressure transducers have been used in this study; the first, an Omega Engineering PX-303 (range: 0 psia to 50 psia), has a full scale uncertainty of 1.25 %, or ± 0.625 psi (4309.2 Pa). The second transducer is an Omega Engineering MMA100V10T2D0T4A6 type (range: 0 torr to 5200 torr) and was purchased because preliminary results of this uncertainty analysis indicated that the largest contributor to the uncertainty of T_C was the initial pressure measurement. The full scale uncertainty of the MMA type transducers is 0.05 %, resulting in an uncertainty of ± 2.6 torr (346.6 Pa), an order of magnitude lower than the PX-303 while also providing more than double the operating range. Total uncertainties using the appropriate pressure transducer are reported in each experimental section of this work; both transducers will be analyzed in this section. Bias uncertainty due to the signal acquisition equipment is negligible compared to the standard error in the pressure transducers.

The precision uncertainty is due to the limit of precision of the display on the Omega Engineering DP41-B process meter used to monitor the initial pressure. This is ± 0.005 torr (0.666 Pa). The total uncertainty of the initial pressure is:

$$U_{P_0} = \sqrt{\left(B_{P_0}\right)^2 + \left(R_{P_0}\right)^2} = \sqrt{(4309.2\,\text{Pa})^2 + (0.666\,\text{Pa})^2} = 4309.2\,\text{Pa} \qquad (2.18a)$$

$$U_{P_0} = \sqrt{\left(B_{P_0}\right)^2 + \left(R_{P_0}\right)^2} = \sqrt{(346.6\,\text{Pa})^2 + (0.666\,\text{Pa})^2} = 346.6\,\text{Pa} \qquad (2.18b)$$

2.1.8.3 Uncertainty in Compressed Pressure

The bias uncertainty in the compressed pressure is due to the standard error in the piezoelectric pressure transducer. According to the manufacturer's calibration, the deviation of the full scale output from linearity is less then 0.1 % over the pressure range 0 bar to 50 bar, indicating that $B_{P_C} = 0.05\,\text{bar} = 5000\,\text{Pa}$. The uncertainties in the signal acquisition equipment are negligible compared to this uncertainty. The precision uncertainty is due to the limit of precision of the output

of the pressure, and is 5×10^{-7} bar. This is negligible compared to the bias uncertainty, so the total uncertainty of the compressed pressure is:

$$U_{P_C} = B_{P_C} = 0.05\,\text{bar} = 5000\,\text{Pa} \tag{2.19}$$

2.1.8.4 Uncertainty in the Specific Heat

The uncertainty in the specific heat comes from two sources. First is the uncertainty in the mixture composition and second is the uncertainty in the linear fit to the total specific heat. The uncertainty in the mixture composition can be estimated by the same method as is used for T_C. The specific heat is given by Eq. (2.8), so we can take partial derivatives of that equation with respect to the mole fractions of the species to find the total uncertainty:

$$
\begin{aligned}
\left(U_{\hat{C}_{p,\text{total}}}\right)^2 &= \left(\frac{\partial \hat{C}_p}{\partial X_1} U_{X_1}\right)^2 + \dots + \left(\frac{\partial \hat{C}_p}{\partial X_n} U_{X_n}\right)^2 \\
&= \left(\hat{C}_{p,1} U_{X_1}\right)^2 + \dots + \left(\hat{C}_{p,n} U_{X_n}\right)^2
\end{aligned}
\tag{2.20}
$$

where n is the total number of species. In Eq. (2.20), it is assumed that the uncertainty in the specific heats of each species is negligible. This is considered an acceptable assumption for stable species such as the fuel molecules, oxygen, nitrogen, and argon. Experience with several kinetic mechanisms has shown that the typical variation in individual $\hat{C}_p$ fits causes approximately 1 K changes in T_C.

The uncertainty of the mole fraction of the species is estimated differently depending on how the species was introduced to the mixing tank. For liquid fuel species, experiments with GC/MS have shown that there is approximately 5 % variation in mole fraction from the expected value [64]; this value is adopted for the total uncertainty of all liquid fuels. The mole fraction of the gaseous species is determined by their partial pressures when filling; the mole fraction is related to the pressure by

Dalton's Law of Partial Pressure [140, 141]:

$$X_i = \frac{P_i}{\Sigma_i P_i} \tag{2.21}$$

where P_i is the partial pressure of a species and the sum is over all of the species. It follows that:

$$\begin{aligned}(U_{X_i})^2 &= \left(\frac{\partial X_i}{\partial P_i} U_{P_i}\right)^2 + \sum_{j \neq i}\left(\frac{\partial X_i}{\partial P_j} U_{P_j}\right)^2 \\ &= \left(\frac{\Sigma_{j\neq i} P_j}{(\Sigma_i P_i)^2} U_{P_i}\right)^2 + \sum_{j \neq i}\left(\frac{-P_i}{(\Sigma_i P_i)^2} U_{P_j}\right)^2\end{aligned} \tag{2.22}$$

The uncertainties of each of the pressures P_i are equal and can be estimated by the same procedure as in Sec. 2.1.8.2 since the same pressure transducer is used to measure the pressure. It is assumed that the uncertainty in each partial pressure is independent of all the others for simplicity, although this will not strictly be the case because the gases are filled sequentially.

A line is fit through the end points of the total specific heat curve via simultaneous solution of the equations:

$$\begin{aligned}\hat{C}_{p,2} &= bT_2 + a \\ \hat{C}_{p,1} &= bT_1 + a\end{aligned} \tag{2.23}$$

where $\hat{C}_{p,1}$ and $\hat{C}_{p,2}$ are the total specific heats at T_1 and T_2 respectively. Solving Eq. (2.23) for b and a gives:

$$\begin{aligned}b &= \frac{\hat{C}_{p,2} - \hat{C}_{p,1}}{T_2 - T_1} \\ a &= \frac{f_2 \hat{C}_{p,2} - f_1 \hat{C}_{p,1}}{f_2 - f_1}\end{aligned} \tag{2.24}$$

where f_1 and f_2 are chosen so that b is eliminated in Eq. (2.23).

Uncertainty in the slope and y-intercept can be found by:

$$(U_b)^2 = \left(\frac{\partial b}{\partial \hat{C}_{p,1}} U_{C_{p,1}} \right)^2 + \left(\frac{\partial b}{\partial \hat{C}_{p,2}} U_{C_{p,2}} \right)^2$$

$$(U_a)^2 = \left(\frac{\partial a}{\partial \hat{C}_{p,1}} U_{C_{p,1}} \right)^2 + \left(\frac{\partial a}{\partial \hat{C}_{p,2}} U_{C_{p,2}} \right)^2 \tag{2.25}$$

where the partial derivatives are:

$$\frac{\partial b}{\partial \hat{C}_{p,1}} = \frac{-1}{T_2 - T_1} \qquad\qquad \frac{\partial b}{\partial \hat{C}_{p,2}} = \frac{1}{T_2 - T_1} \tag{2.26}$$

$$\frac{\partial a}{\partial \hat{C}_{p,1}} = \frac{-f_1}{f_2 - f_1} \qquad\qquad \frac{\partial a}{\partial \hat{C}_{p,2}} = \frac{f_2}{f_2 - f_1} \tag{2.27}$$

and the uncertainties of the specific heats $U_{C_{p,1}}$ and $U_{C_{p,2}}$ are calculated as described earlier.

2.1.8.5   Uncertainty in Compressed Temperature for Alcohol Experiments

The following analysis is considered for a representative mixture of 3.38 mol % t-butanol, 20.30 mol % O_2, and 76.32 mol % N_2, i.e. a $\phi = 1.0$ mixture of t-butanol and air. Similar results are obtained for experiments with the other butanol isomers and i-pentanol and experiments at different fuel concentrations, because the fuel specific heats are similar and each experiment uses similar diluent concentrations.

A typical total pressure after filling is approximately 1520 torr (202,650 Pa), with approximately 42,000 Pa of O_2 and 160,650 Pa of N_2. The partial pressure of the liquid fuel is assumed to contribute a negligible amount to the total pressure during the filling of the gases for the purposes of this uncertainty analysis. The results shown below use the uncertainty associated with the PX-303-type pressure transducer because this transducer was used for all of the experiments with alcohol fuels.

Applying Eq. (2.14) to typical conditions of $P_0 = 500$ torr to 760 torr, $T_0 = 300$ K to 400 K, and $P_C = 15$ bar to 30 bar yields a maximum uncertainty of approximately 2 % to 3 % of the compressed temperature T_C.

2.1.8.6 Uncertainty in Compressed Temperature for Methylcyclohexane Experiments

The following analysis is considered for a representative mixture of 1.05 mol % MCH, 10.99 mol % O_2, 12.83 mol % N_2, and 75.13 mol % Ar, i.e. the stoichiometric mixture (#1) from Table 5.1. Similar results are obtained for the other mixtures.

A typical total pressure after filling is approximately 3390 torr (452,000 Pa), with approximately 33,500 Pa of O_2, 78,200 Pa of N_2, and 340,300 Pa of Ar. The partial pressure of the liquid fuel is again assumed to contribute a negligible amount to the total pressure during the filling of the gases for the purposes of this uncertainty analysis. The results shown below use the uncertainty associated with the MMA-type pressure transducer because this transducer was used for all of the experiments with MCH.

Applying Eq. (2.14) to typical conditions of $P_0 = 500$ torr to 1520 torr, $T_0 = 300$ K to 400 K, and $P_C = 15.1$ bar to 50 bar yields a maximum uncertainty of approximately 1 % of the compressed temperature T_C.

2.2 Rapid Sampling Apparatus

The Rapid Sampling Apparatus (RSA) used in this study is an adaptation of the RSA described in the work of Mittal and Sung [114] and Mittal et al. [122]. The basic concept is the same as that developed by Roblee [103]. An aluminum diaphragm is punctured by a pointed rod at the appointed time, evacuating the contents of the reaction chamber into a large vessel. The temperature drop caused by the expansion of the gases into the sampling chamber quenches the reactions, and the products can be removed to an analysis system.

The design of Mittal [114, 122] used an electromagnet to hold a spring in compression. At the designated sampling time, the power to the electromagnet was cut, and the spring force thrust the puncture rod forward into the diaphragm. This system was prone to premature puncture if

C:/Users/bww09001/Documents/Github/dissertation/figures/02-Experimental-Facilities/sam

Figure 2.5: Schematic of the modified RSA used in this study

the spring force overcame the electromagnetic force (e.g. due to a small drop in the current to the electromagnet).

To alleviate the premature puncture problem, the puncture mechanism has been updated as shown in Fig. 2.5. The electromagnet/spring system has been replaced with a linear-acting solenoid. The puncture rod is held in the retracted position by a permanent magnet (not shown) to overcome the pressure force acting on the radial cross section of the rod when the sampling tank is under vacuum. At the sampling time, the solenoid is actuated by a DC voltage to puncture the diaphragm.

The sampled gases flow from the sample tank into an evacuated sampling bottle, as shown schematically in Fig. 2.1. The sample is diluted with ultra-high-purity helium (99.999 % purity) and taken to the analysis system, which is described in Sec. 2.3.

?? shows a pressure trace from the reaction chamber when the solenoid has been triggered and a pressure trace when the solenoid is not actuated. It can be seen that there is a very rapid drop in pressure in the reaction chamber. The ratio of the EOC volume of the reaction chamber to the total (approximate) volume of the sampling tank plus the reaction chamber is 1.1772×10^{-2}. Assuming the expansion into the sampling tank is isentropic and the ratio of specific heats is fixed at $\gamma = 1.3$, the temperature ratio is approximately 2.6379×10^{-1}, leading to temperatures after expansion on the order of $T \approx 200\,\text{K}$, depending on T_C. After expansion, the gases are warmed to room temperature in the sample bottle. The fuel partial pressure in the sampling bottle is a factor of two lower than the saturated vapor pressure at room temperature, so that heating of the sample bottle is not required.

2.3 Gas Chromatograph/Mass Spectrometer

2.3.1 Theory of Gas Chromatography/Mass Spectrometry

2.3.1.1 Gas Chromatography

A gas chromatograph (GC) is a device that physically separates components of a gas sample by means of a tube—known as a *column*—lined or filled with a substance that interacts with the components in the sample. The sample is transported the length of the column by a flow of carrier gas, usually helium or hydrogen, also known as the *mobile phase*. A detector is placed at the outlet of the column to measure the amount and type of components eluted from the column.

The separation of the gaseous components in the sample is effected by the interaction of the sample with the lining of the column, known as the *stationary phase*. Gaseous species that have little interaction with the stationary phase and spend most of their time in the mobile phase are eluted from the column before species that interact strongly with the stationary phase and spend little time in the mobile phase [142].

The column is placed in an insulated oven so that its temperature may be controlled. The column temperature in a given analysis may be constant or may be controlled as a function of time. Since the time that a given component takes to move through the column is a function of temperature, this facility allows optimization of the elution time of the various components in the sample.

The injector of the GC is also temperature controlled; the temperature of the injector is set high enough so that all components (including the solvent, if any) are vaporized but not so high that the sample starts to degrade. On the present GC, a split/splitless injector is installed. This allows for operation in the split mode, where a percentage of the injected sample is removed from the injector prior to injection onto the column, or in the splitless mode, where nearly all of the sample is injected into the column. The split mode is used in this work. The amount of sample removed is controlled

by a valve in the injector. The split ratio is calculated according to Eq. (2.28):

$$\text{Split Ratio} = \frac{\text{Column Flow} + \text{Vent Flow}}{\text{Column Flow}} \qquad (2.28)$$

where the column flow is the carrier gas flow rate at the head of the column and the vent flow is the flow out of the splitter vent [142].

A GC may also be equipped with a gas sample injection valve, in addition to the split/splitless injector. This valve is connected serially prior to the split/splitless injector. The present GC is equipped with a 10-port Valco sample injection valve, shown schematically in Fig. 2.6. Each port is numbered, and curved lines indicate connections between ports. The sample injection valve is used to inject a consistent mass of sample into the column with each injection. This permits reliable quantification of the components in the sample. First, the sample is loaded into the sample loop when the valve is in the "load" position, as in Fig. 2.6a. Then, the valve is electrically actuated at the start of the GC run to rotate the connections into the "inject" position. This allows carrier gas to flow through the sample loop and push the sample from the sample loop into the column via the split/splitless injector (Fig. 2.6b). The valve is then actuated again to remove the sample loop from the carrier gas path and restore the "load" position (Fig. 2.6a).

The sample injection valve is equipped with a heater to maintain the valve body at a constant temperature and the entire assembly is installed in an insulated box. However, this heater is insufficient to heat the tubes attached to the valve, so an additional heater rope is installed in the insulated box. To measure the temperature of the sample loop directly, a thermocouple is fixed to the sample loop by ceramic cement. The temperature of the sample loop is used to control the power provided to the rope heater, while a built-in thermocouple is used to control the power provided to the valve body heater, so that the sample loop remains at a constant temperature.

(a) Load position   (b) Inject position

Figure 2.6: GC/MS sample injection valve.

2.3.1.2 Mass Spectrometry

Many types of detectors are available for GC analyses. These commonly include flame ionization detectors, thermal conductivity detectors, and mass spectrometers. In this work, a mass spectrometer is used to identify and quantify the species eluted from the column.

The fundamental operation of a mass spectrometer (MS) is to detect the spectrum of ions in a given sample. The MS generates this spectrum by detecting the mass-to-charge (m/z) ratios of the ions. Ions are generated from the effluent of the column—which includes sample components, mobile phase, and column bleed, collectively called *analytes*—by an ionization source, typically either electronic or chemical in nature. Nearly all of the ions generated will have a single charge, $z = 1$ [143]; thus, the m/z value of the ions is also equal to the mass of the ion.

In this work, electron ionization (EI) is used to generate the ions for analysis. The effluent from the column is passed in front of an electron source so that the electrons impact the analyte molecules and remove an electron, generating a positive ion. EI is a *hard ionization* technique, in that the electron impact transfers a significant amount of energy to the analyte molecule [143]. The additional energy causes the ion to fragment into two or more pieces; the spectrum of these

44
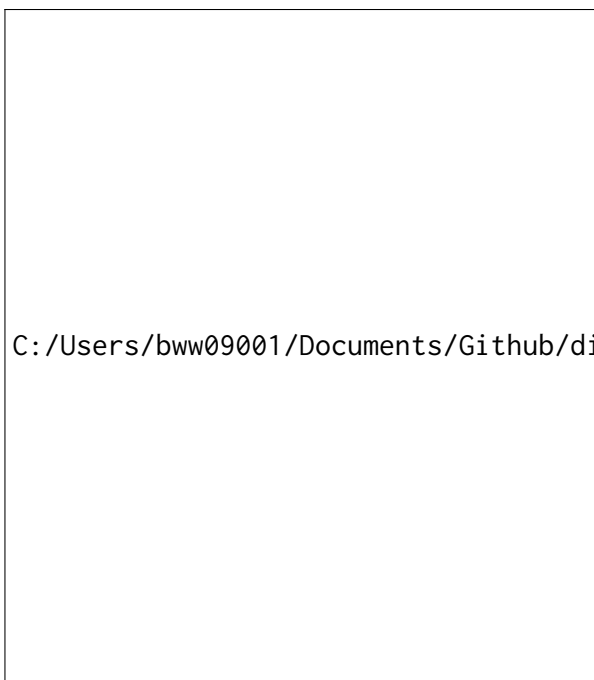
Figure 2.7: Schematic of the transmission quadrupole in an MS.

fragments is characteristic for a given molecule and can be used as a "fingerprint" to identify the source molecule for a given spectrum.

After ionization, the fragments are formed into a beam and accelerated out of the ionization chamber towards the detector. Several detectors are available, including time-of-flight and transmission quadrupole. All of these detectors require high vacuum to avoid impact of the ion beam with extraneous species prior to reaching the detector. The vacuum is achieved in the present MS by a two-stage design, using a rotary vane pump in combination with a turbomolecular pump to achieve ultimate pressures of approximately $2\,\mathrm{Pa}$.

The MS used in this study is a transmission quadrupole type, shown schematically in Fig. 2.7. The transmission quadrupole separates specific ions from the ion beam by means of a time-varying electric field. Conceptually, the quadrupole can be imagined as four round rods, arranged in a cross pattern, with their long axes aligned parallel to the ion beam (i.e. the z axis). The ions are admitted to the rods at one end (e.g. at the origin in Fig. 2.7) and the detector is placed parallel to the $x - y$ plane in Fig. 2.7 at the other end of the rods (not shown in Fig. 2.7). A positive DC voltage is applied to one pair of the rods, while a negative DC voltage is applied to the other pair of rods; in addition,

an AC voltage is applied simultaneously to all four rods. Assuming a specific ratio of AC amplitude to DC amplitude, ions of a certain m/z will remain in the ion beam and reach the detector. Then, holding the AD:DC amplitude ratio fixed, the amplitudes are ramped with a known function of time. This varies the particular m/z that will remain in the ion beam and reach the detector to be recorded [143], generating a mass spectrum.

The voltage amplitudes are ramped many times per second—typical ramp times range from 0.05 s to 0.5 s, depending on the range of m/z values to be acquired—so that many spectra are acquired during the elution of a given chemical compound from the column, which typically occurs on the order of a few seconds. For a given scan from the lowest to the highest amplitude, the number of ions of each m/z is measured at the detector. This information is typically presented in the form of a relative intensity plot. The abscissa is the (integer) m/z while the ordinate is the intensity of a particular m/z scaled by the maximum intensity of all the m/z in a given scan. It is not required that the m/z be integers, although they are usually presented as such for simplicity. An example of a mass spectrum for a given time in a GC/MS analysis is shown in Fig. 2.8.

In addition to the mass spectrum, the MS reports the total ion current (TIC), also known as the total ion chromatogram. This is the sum of all of the mass intensities for a given scan. A sample TIC is plotted in Fig. 2.9 where the abscissa is time in min and the ordinate is an arbitrary unit. Finally, the MS can also report the mass chromatogram (MC), which is the chromatogram for a specific m/z as a function of time.

2.3.2 Identification and Quantification of Species using GC/MS

Species are identified using a GC/MS system by their unique mass spectra. Each peak in the TIC typically represents one compound eluting from the column, although in theory each peak can represent more than one compound if the compounds are retained similarly by the column. The peak is caused by an increase in the number of ions reaching the detector on each scan relative to the baseline as the compound elutes and is ionized. As mentioned previously, many scans of the desired m/z range are conducted over the time that a compound is eluting from the column. To determine
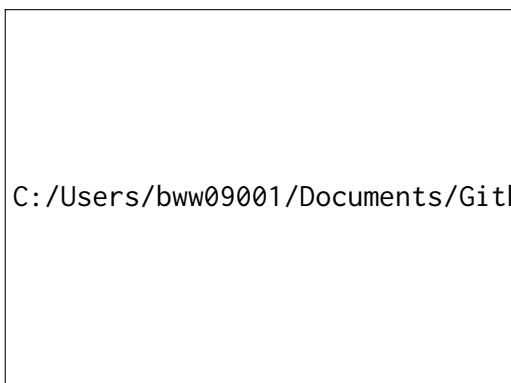
Figure 2.8: Example mass spectrum for a given scan during a GC/MS analysis
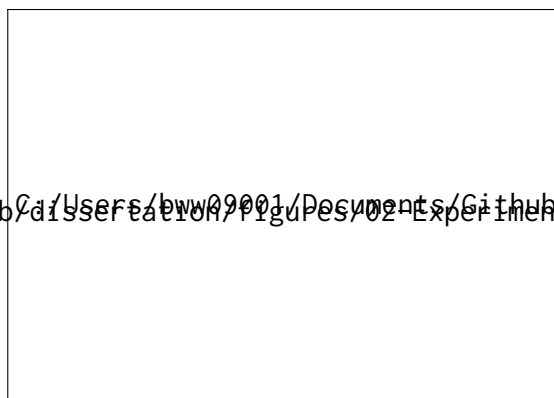
Figure 2.9: Example TIC for a GC/MS analysis of Jet Fuel

the identity of a compound in a given peak, the set of mass intensities over the peak are averaged and the background spectrum is subtracted; this average spectrum is compared to a database supplied by the National Institute of Standards and Technologies (NIST). The database returns several suggested species with a degree of matching parameter indicating how well the supplied spectrum matches the spectrum in the database.

In this work, the external standard method of quantification is used. This requires that calibration curves for each of the species of interest be created, relating the area of the peak in the TIC to the number of moles of analyte reaching the detector. The number of moles of analyte can in turn be related to the number of moles of sample in the gas sample injection valve sample loop. Once the calibration curve is generated, it is used to relate the measured area of the peak of the particular component to its mole fraction. Detailed methods for the construction of calibration curves will be given in Sec. 2.3.3.

2.3.3   Experimental Procedure

The GC/MS used in this study is a Shimadzu model QP-2010S, equipped with a 10-port Valco sample injection valve and split/splitless injector, as mentioned previously. The column used is a Phenomenex model ZB-5MS capillary column with length 30 m, inner diameter 0.25 µm, and film thickness of 0.25 µm. The operating parameters of the GC/MS (known as the *method*) are shown in

??.

The pressure in the gas injection valve sample loop is monitored by an MMA type pressure transducer, the same model as used in Sec. 2.1.8.2. The sample outlet in Fig. 2.6 is open to the atmosphere so that a consistent pressure is maintained in the sample loop. The volume of the sample loop is 10 µL. With the temperature, pressure, and volume of the sample loop known, the number of moles of sample can be calculated by the ideal gas law.

A calibration curve is built for the major species by the following procedure. First, the sample bottle is vacuumed to less than 1 torr. Mixtures of the species of interest in the liquid state are prepared by massing each component on a high-accuracy AND-201 scale. A small mass of this mixture is drawn into a syringe and massed on the same scale. The mixture is injected through a septum into the sample bottle. The sample bottle is filled with high-purity nitrogen or helium to dilute the sample. The sample bottle is connected to the sample injection valve on the GC/MS and the valve on the sample bottle is opened and quickly closed. The pressure is allowed to equalize and the GC/MS is started.

After the completion of the GC/MS method, the TIC is analyzed by the Shimadzu GCMS Post-run Analysis software (version XXXX). Each peak is automatically integrated by the software so that its area can be found. The peak area is then related to the number of moles of sample sent to the detector by linear least-squares regression. This calibration curve is used to compute the mole fraction of any given peak area for that species.

Chapter 3

The Butanol Isomers

Table 3.1: HHV of Ethanol, Butanol Isomers, and Gasoline

Compound	Ethanol [21]	Butanol Isomers [21]	Gasoline [22]
HHV [MJ/kg]	29.67	≈ 36	48.46

C:/Users/bww09001/Documents/Github/dissertation/figures/03-Butanol/nbuoh-skeletal.pdf

(a) *n*-butanol   (b) *s*-butanol   (c) *t*-butanol   (d) *i*-butanol
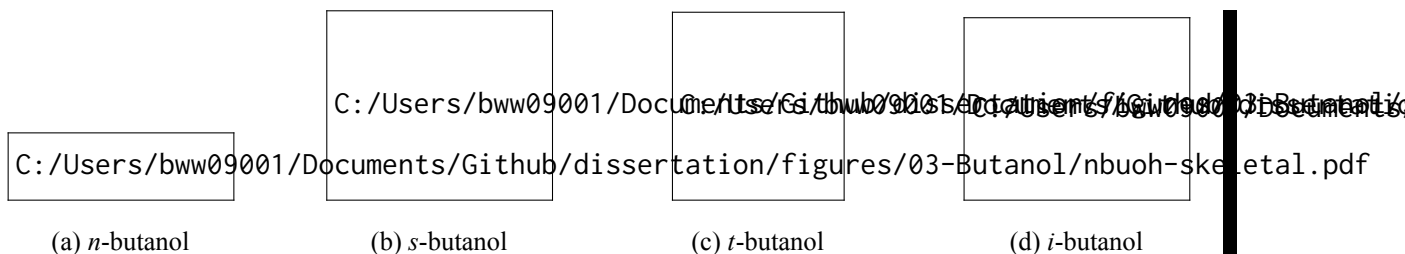
Figure 3.1: Skeletal structures of the butanol isomers

3.1 Structure of the Butanol Isomers

Butanol is the four carbon alcohol, and has four isomers: *n*-butanol (1-butanol); *s*-butanol (2-butanol); *t*-butanol (2-methyl-2-propanol); and *i*-butanol (2-methyl-1-propanol). The skeletal structures of the four isomers are shown in Fig. 3.1. The carbon atoms in the skeleton are labeled according to their distance from the hydroxyl moeity; the α carbon is the closest to the hydroxyl, followed by β, γ, and δ carbons. Not all of the butanols have all of the types of carbons listed here, due to varying

chain lengths. For instance, t-butanol has one α carbon (not labeled), three β carbons, and no γ or δ carbons.

Three of the butanol isomers can be produced by biological pathways (n-, s-, and i-butanol) [26, 27], making them candidates for the "second-generation" of biofuels [25, 26]. Although t-butanol does not have an identified biological production pathway, it has commercial significance as an octane enhancer. In addition, the four isomers of butanol represent the smallest alcohol system with all four types of branching in the skeleton. This makes them excellent candidates to build kinetic models that can be extended to larger alcohols with similar structures.

Table 3.1 shows a comparison of the higher heating value of the butanol isomers with ethanol and gasoline. The higher energy density of the butanol isomers allows them to be blended in gasoline in higher proportions and reduces the volumetric fuel economy (e.g. mpg) impact of replacing gasoline with biofuels.

3.2 Experimental Procedure

The reactants used in this study, along with their purities, are shown in Table 3.2. To determine the relative proportions of each reactant in the mixture, the absolute mass of fuel, the equivalence ratio (ϕ), and the oxidizer ratio ($X_{O_2} : X_{\text{inert}}$, where X indicates mole fraction) are specified. s- and i-Butanol are liquid at room temperature and have relatively low vapor pressure; therefore, each is massed in a syringe to within $0.01\,\text{g}$ of the specified value. t-Butanol is solid at room temperature (melting point: $25\,°\text{C}$), and is melted before being handled in the same procedure as the other fuels. The $17\,\text{L}$ mixing tank is vacuumed to an ultimate pressure less than $5\,\text{Torr}$ prior to the injection of the liquid fuel through a septum. Proportions of O_2 and N_2 are added manometrically at room temperature. The preheat temperature of the RCM is set above the saturation point for each fuel to ensure complete vaporization. A magnetic stirrer mixes the reactants. The temperature inside the mixing tank is allowed to equilibrate for approximately $1.5\,\text{h}$.

This approach to mixture preparation has been validated in several previous studies by with-

Table 3.2: Experimental Conditions and Reactant Purities

Reactant (Purity)					Equivalence Ratio ϕ	Compressed Pressure P_C (bar)
s-butanol (99.99 %)	i-butanol (99.99 %)	t-butanol (99.99 %)	O_2 (99.999 %)	N_2 (99.995 %)		
Mole Percentage						
3.38			20.30	76.32	1.0	15
3.38			20.30	76.32	1.0	30
	3.38		20.30	76.32	1.0	15
	3.38		20.30	76.32	1.0	30
		3.38	20.30	76.32	1.0	15
		3.38	20.30	76.32	1.0	30
		1.72	20.65	77.63	0.5	30
		6.54	19.63	73.83	2.0	30
	1.72		20.65	77.63	0.5	15
	1.72		20.65	77.63	0.5	30
	3.38		40.60	56.02	0.5	15
	3.38		40.60	56.02	0.5	30
	3.38		10.15	86.47	2.0	30
	3.38		10.15	86.47	2.0	30

drawing gas samples from the mixing tank and analyzing the contents by GC/MS [64], GC-FID [120], and GC-TCD [91]. These studies have verified the concentration of n-butanol, n-decane, and water, respectively. In addition, both the work by Kumar et al. [120] on n-decane and the study of Weber et al. [64] on n-butanol confirmed that there was no fuel decomposition over the course of a typical set of experiments. Furthermore, within this study, each new mixture preparation is checked against previously tested conditions to ensure reproducibility.

Table 3.2 shows the experimental conditions considered in this study. The compressed pressure conditions have been chosen to match the previous n-butanol study [64], but also to provide data in regions not covered extensively in previous work. In addition, the fuel loading conditions have been chosen to complement previous work; the studies by Stranic et al. [59] and Moss et al. [55] used relatively dilute mixtures, so we have included higher fuel loading conditions. Furthermore, the compressed temperature conditions we have studied ($T_C = 715\,\text{K}$ to $910\,\text{K}$) have not been examined in any other study, to our knowledge.

3.3 Experimental Results

3.3.1 Comparison of Butanol Isomers Ignition

Figure 3.2 shows the ignition delays of the four isomers of butanol measured in the RCM, at compressed pressure of $P_C = 15$ bar for stoichiometric mixture in air. The dashed line for each isomer is a least squares fit to the data. The vertical error bars are two standard deviations of the measurements of the ignition delay. The standard deviation is computed based on all the runs at a particular compressed temperature and pressure condition, as discussed in Sec. 2.1.3. The uncertainty in T_C was estimated in Sec. 2.1.8.5 to be approximately 2 % to 3 %.

Figure 3.2 demonstrates the differences in reactivity between the isomers for stoichiometric fuel/air mixtures at compressed pressure $P_C = 15$ bar. *n*-Butanol is clearly the most reactive, followed by *s*- and *i*-butanol, which have very similar reactivities in this temperature and pressure range. *t*-Butanol is the least reactive.

The order of reactivity found in the RCM at 15 bar agrees with the ST study at higher temperatures (approximately 1275 K to 1667 K) and lower pressure (1.5 atm) by Stranic et al. [59] but differs slightly from the studies of Moss et al. [55] who measured ignition delays in a ST near 1.5 atm and between 1275 K to 1400 K, and Veloo and Egolfopoulos [31] who measured atmospheric-pressure laminar flame speeds. In particular, Moss et al. [55] and Veloo and Egolfopoulos [31] found distinct differences in reactivity between *s*- and *i*-butanol, but the present study and the study by Stranic et al. [59] found that they were nearly indistinguishable in terms of reactivity under the conditions investigated. In addition, Stranic et al. [59] noted some disagreement between their ST ignition data and the data of Moss et al. [55] but their attempts to isolate the cause could not discern what the difference might be caused by.

Further, the order of the reactivity of the butanol isomers shows complex temperature and pressure dependence. This is demonstrated by the results shown in Fig. 3.3. In Fig. 3.3, the order of reactivity is different than in Fig. 3.2, where the only variation between the plots is the compressed

Figure 3.2: Ignition delays of the four isomers of butanol at compressed pressure $P_C = 15$ bar. Dashed lines are least squares fits to the data.
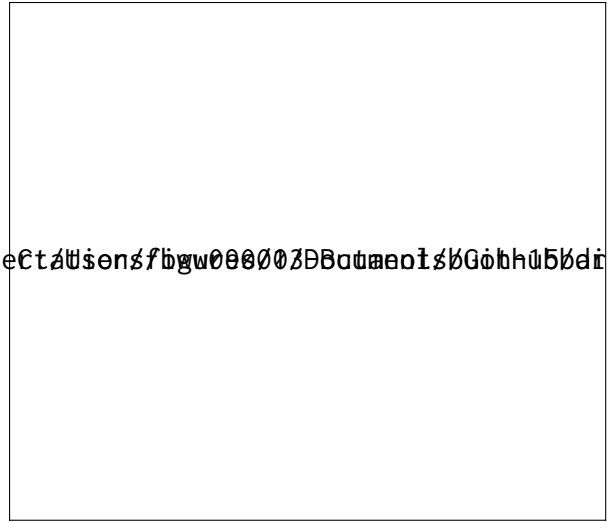
Figure 3.3: Ignition delays of the four isomers of butanol at compressed pressure $P_C = 30$ bar. Dashed lines are least squares fits to the data.

pressure; in Fig. 3.3 the compressed pressure is $P_C = 30$ bar. Fig. 3.3 shows *i*-butanol to be the least reactive, *s*-butanol to be less reactive than but similar to *t*-butanol, and *n*-butanol to be the most reactive. Interestingly, the results of the ST study by Stranic et al. [59] differ from those in the current study at higher pressure, despite the agreement at lower pressure. In their study, Stranic et al. [59] found *i*- and *n*-butanol to have similar reactivity near 43 atm in the temperature range of 1020 K to 1280 K, whereas in the present study we find *i*-butanol to be the least reactive of all four isomers at a pressure of 30 bar and over the temperature range (715 K to 910 K) investigated.

3.3.2   Ignition of *t*-Butanol

The fact that *t*-butanol becomes relatively more reactive than *i*- and *s*-butanol as pressure increases is surprising at first glance, and the reasons are not immediately apparent. Closer examination of the pressure traces for each experiment gives one clue as to the cause of the increased reactivity. Figure 3.4 shows the pressure traces for the *t*-butanol experiments at 15 bar for stoichiometric mixtures in air. It is evident that there is some pre-ignition heat release, because the reactive pressure trace diverges from the non-reactive case prior to the ignition event. Of the other isomers of butanol,
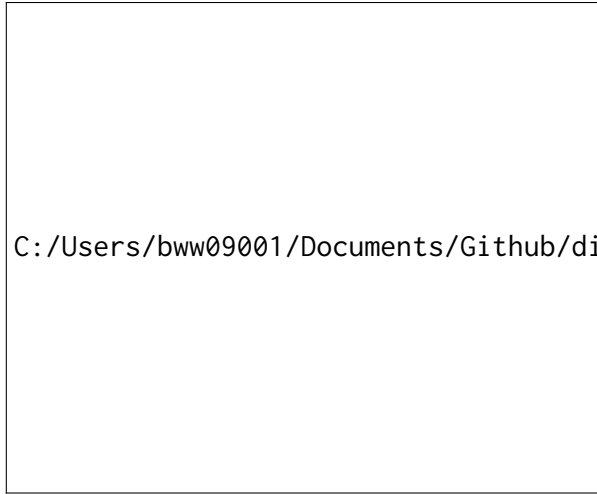
Figure 3.4: Pressure traces of the 15 bar *t*-butanol experiments, in stoichiometric air.
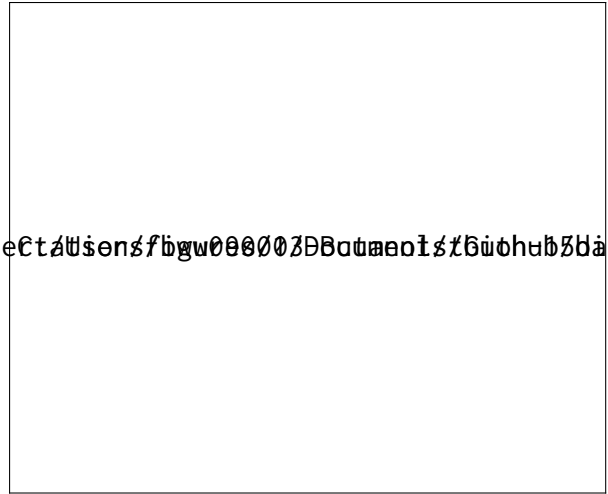
Figure 3.5: Pressure traces of the 30 bar *t*-butanol experiments, in stoichiometric air.

only *n*-butanol shows any visible heat release prior to the main ignition event at 15 bar.

Figure 3.5 shows the pressure traces for *t*-butanol experiments at 30 bar for stoichiometric mixtures in air. The effect of pre-ignition heat release is even more striking in this figure, with substantial changes in the slope of the pressure trace during the reactive runs. Comparison to the pressure traces of the other isomers once again shows that the magnitude of the pre-ignition heat release for *t*-butanol is much greater. Despite the appearance of early pressure rise, which is typically indicative of two-stage ignition and low temperature chain branching, we do not find a negative temperature coefficient region in terms of the ignition delay response for any *t*-butanol experiments. Therefore, we adopt the phrase "pre-ignition heat release" rather than "two-stage ignition" in this work.

In an effort to understand the reactions causing the pre-ignition heat release, further experiments are conducted for *t*-butanol at $P_C = 30$ bar, for equivalence ratios of 0.5 and 2.0 in air. Figure 3.6 shows Arrhenius plots of the ignition delays for the three equivalence ratios. As with the previous *n*-butanol experiments at 15 bar [64] $\phi = 0.5$ is the least reactive and $\phi = 2.0$ is the most reactive. The slopes are similar, indicating that the overall activation energies are similar for the conditions investigated.

A more interesting comparison is of the pressure traces of the three equivalence ratios. It is
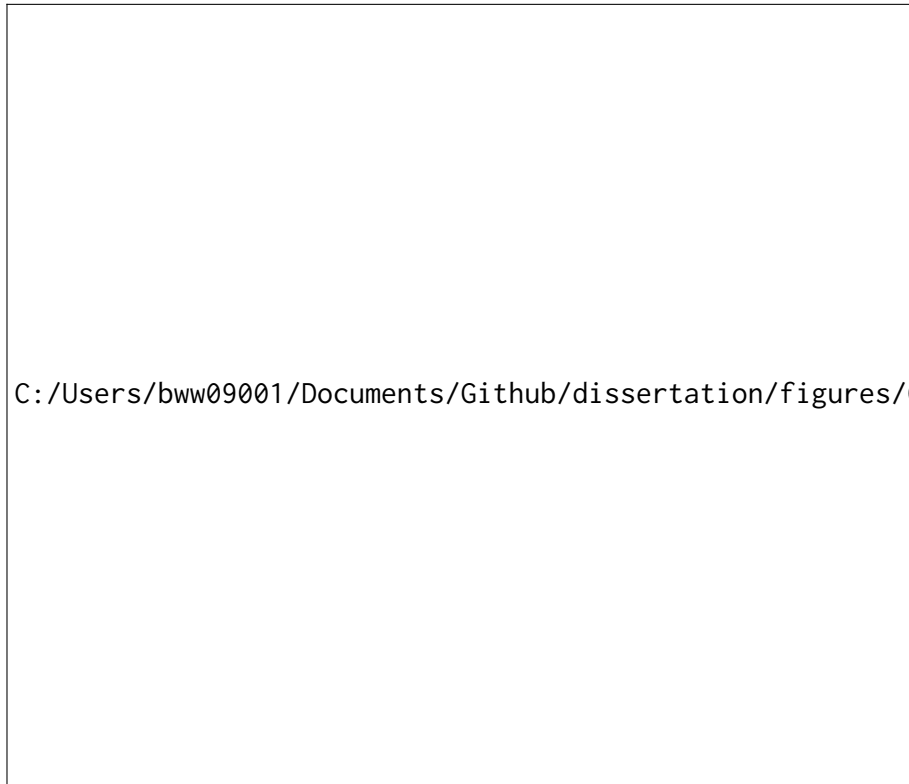
Figure 3.6: Ignition delays of three equivalence ratios of *t*-butanol in air, for $P_C = 30$ bar. Lines represent least squares fits to the data.
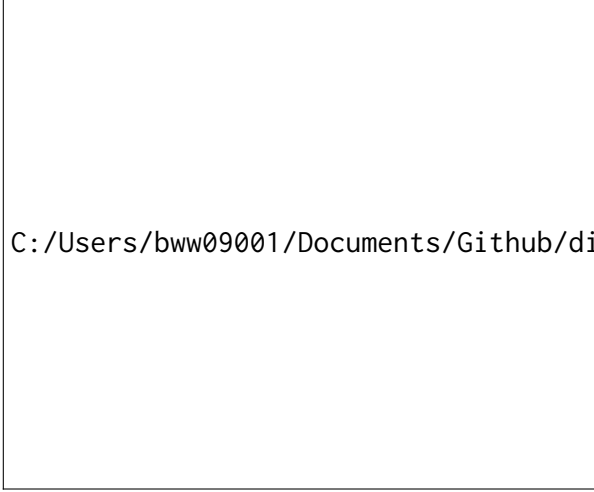
Figure 3.7: Pressure traces of the 30 bar t-butanol experiments, $\phi = 0.5$ in air.

Figure 3.8: Pressure traces of the 30 bar t-butanol experiments, $\phi = 2.0$ in air.

clear from Figs. 3.5, 3.7, and 3.8 that there are qualitative differences in the pre-ignition heat release between the three equivalence ratios. This is most likely due to the effect of the increased (reduced) fuel mole fraction in the $\phi = 2.0$ ($\phi = 0.5$) case, since the mole fraction of fuel is changed by +93 % (-49 %) compared to the $\phi = 1.0$ case, while the mole fraction of oxygen changes by only -3 % (+2 %) compared to the $\phi = 1.0$ case, as shown in Table 3.2. Therefore, it appears that the qualitative change in pre-ignition behavior is due to the change of fuel mole fraction, where higher fuel loading promotes pre-ignition heat release.

3.3.3   Ignition of i-Butanol

The experimental ignition delays of i-butanol measured at $P_C = 15$ bar and 30 bar and $\phi = 0.5$ in oxygen/nitrogen air are shown in Fig. 3.9. The error bars are equal to twice the standard deviation of all the runs at that condition. The lines are curve fits to the data. The circles represent the 15 bar data, while the squares represent the 30 bar data. Also shown in Fig. 3.9 are the experimental ignition delays presented in Sec. 3.3.1 at $\phi = 1.0$ and $P_C = 15$ bar and 30 bar. The $\phi = 0.5$ cases are shown in blue and the $\phi = 1.0$ cases are shown in red.

For both equivalence ratios, the 15 bar cases are less reactive than the 30 bar cases, as judged

C:/Users/bww09001/Documents/Github/dissertation/figures/03-Butanol/ibuoh-expt
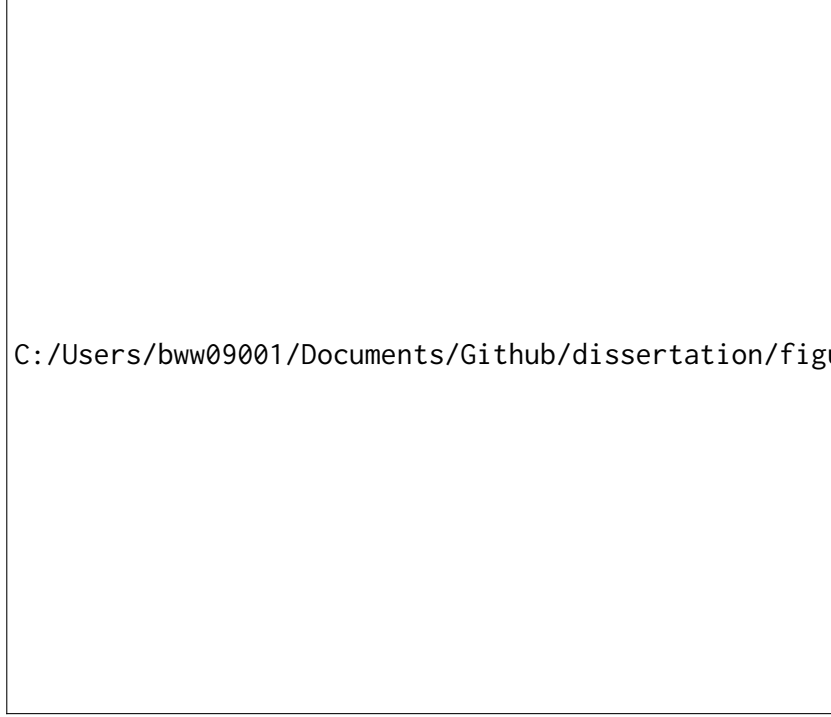
Figure 3.9: Comparison of the experimentally measured ignition delays of i-butanol at two compressed pressures, $P_C = 15\,\text{bar}$ (circles) and $P_C = 30\,\text{bar}$ (squares), and two equivalence ratios, $\phi = 0.5$ (blue) and $\phi = 1.0$ (red).

by the inverse of the ignition delay. Furthermore, in comparing the $\phi = 1.0$ data to the $\phi = 0.5$ data at the same compressed pressure, it is seen that the strong equivalence ratio dependence of the ignition delays previously measured for two other isomers of butanol, n-butanol [64] and t-butanol (Sec. 3.3.2), is also present for i-butanol.

Figures 3.10 and 3.11 show the ignition delays of i-butanol at three equivalence ratios $\phi = 0.5$, 1.0, and 2.0 and $P_C = 15\,\text{bar}$ and 30 bar respectively. In these figures, the equivalence ratio is varied by holding the initial fuel mole fraction constant and varying the oxygen and nitrogen mole fractions. The ignition delay of i-butanol depends strongly on the initial oxygen mole fraction, similar to the trend shown for n-butanol [64].

Figure 3.10: Comparison of the experimentally measured ignition delays of *i*-butanol at three equivalence ratios and P_C = 15 bar. The equivalence ratio is changed by varying the initial oxygen mole fraction at constant initial fuel mole fraction.

Figure 3.11: Comparison of the experimentally measured ignition delays of *i*-butanol at three equivalence ratios and P_C = 30 bar. The equivalence ratio is changed by varying the initial oxygen mole fraction at constant initial fuel mole fraction.

3.4 Simulation Results

3.4.1 Comparison of Simulated Butanol Isomers Ignition

Simulations are performed with the kinetic mechanism from Sarathy et al. [144] denoted as the Sarathy et al. mechanism. Other recent mechanisms, such as the mechanism from Frassoldati et al. [145] do not include low temperature chemistry and are therefore unable to reproduce the low-temperature ignition delays measured in this study. The study by Sarathy et al. [144] validated their model for a wide set of the existing experimental data. In terms of ignition delays, this included the data from the study of Stranic et al. [59] up to 48 atm, our previous study on *n*-butanol [64], and the data being published in this study at 15 bar. Importantly, the mechanism of Sarathy et al. [144] was validated only for the 15 bar RCM data for all four isomers, but not the 30 bar data also being published here. The MIT mechanism [34, 146] was validated for *i*-butanol experiments, including pyrolysis and low pressure premixed flames; although the model includes all four isomers of butanol as reactants, it has not been optimized for any of the isomers except *i*-butanol.
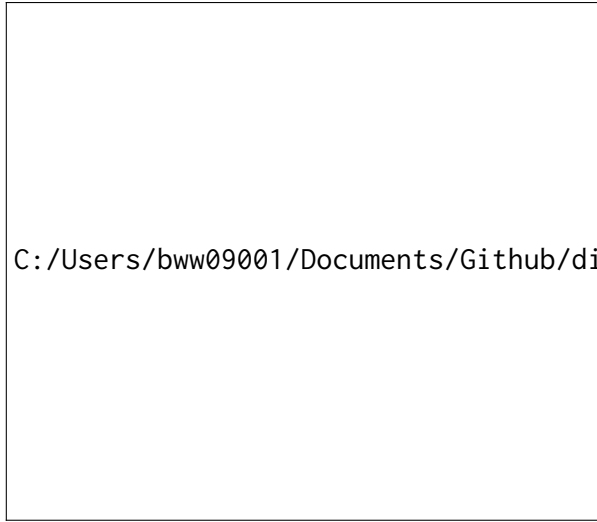
Figure 3.12: $P_C = 15$ bar, stoichiometric mixtures in air. Comparison of VPRO simulations using the kinetic mechanism of Sarathy et al. [144] with experimental ignition delays.
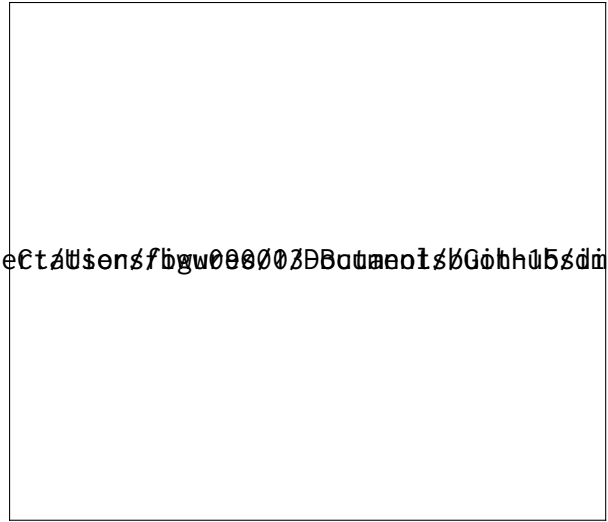
Figure 3.13: $P_C = 30$ bar, stoichiometric mixtures in air. Comparison of VPRO simulations using the kinetic mechanism of Sarathy et al. [144] with experimental ignition delays.

Figures 3.12 and 3.13 show comparison of the VPRO simulations with the experimental data using the mechanism of Sarathy et al. [144]. As Sarathy et al. [144] showed in their work (and as we show here in Fig. 3.12), they found good agreement of the model predictions with the present RCM data at 15 bar. At $P_C = 30$ bar (Fig. 3.13), similar degree of agreement is found for t-butanol and s-butanol compared to $P_C = 15$ bar, although the s-butanol results are under-predicted at high temperature and over-predicted at low temperature. While the model of Sarathy et al. [144] is able to well capture the overall activation energy of i-butanol, it under-predicts the experimental data by about a factor of 2 to 3. The n-butanol data are over-predicted by a factor of about 1.5. Nevertheless, this agreement is quite good, especially considering that the model is not validated for these conditions.

3.4.2 Simulated t-Butanol Ignition

The agreement of the mechanism by Sarathy et al. [144] with the off-stoichiometric mixtures of t-butanol is also quite good, as shown in Fig. 3.14. Figures 3.15a, 3.15b, and 3.15c show more detailed comparisons of the simulated pressure traces and the experimental results, for similar
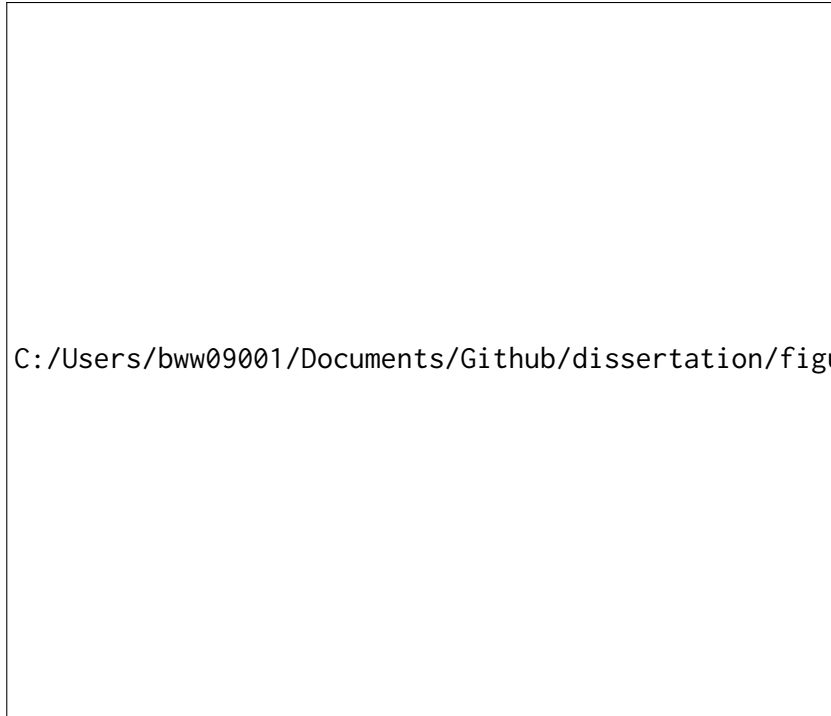
Figure 3.14: Comparison of the simulations using the kinetic mechanism of Sarathy et al. [144] for three equivalence ratio mixtures of *t*-butanol in air at $P_C = 30\,\text{bar}$.

temperatures at the three equivalence ratios, respectively. Clearly, the simulations also exhibit some pre-ignition heat release. In general, the simulations qualitatively predict the pre-ignition heat release behavior at all three equivalence ratios. The $\phi = 0.5$ case has the least heat release and the $\phi = 2.0$ case has the most. Although the simulations are unable to match the heat release behavior quantitatively, they match the experimental ignition delays quite well. Considering the model is not validated for this temperature, pressure, and equivalence ratio regime, the mismatch of the pre-ignition behavior may not be of critical importance, depending on the application.

3.4.3 Simulated *i*-Butanol Ignition

In addition to the model by Sarathy et al. [144] which is validated for all four isomers of butanol, a kinetic model for the combustion of *i*-butanol has been developed and presented by Hansen et al. [34] and Merchant et al. [146]. This model has been validated for species profiles measured in a low-pressure, premixed flame by Hansen et al. [34], an atmospheric pressure diffusion flame by

| (a) $\phi = 0.5$ in air. | (b) $\phi = 1.0$ in air. | (c) $\phi = 2.0$ in air. |
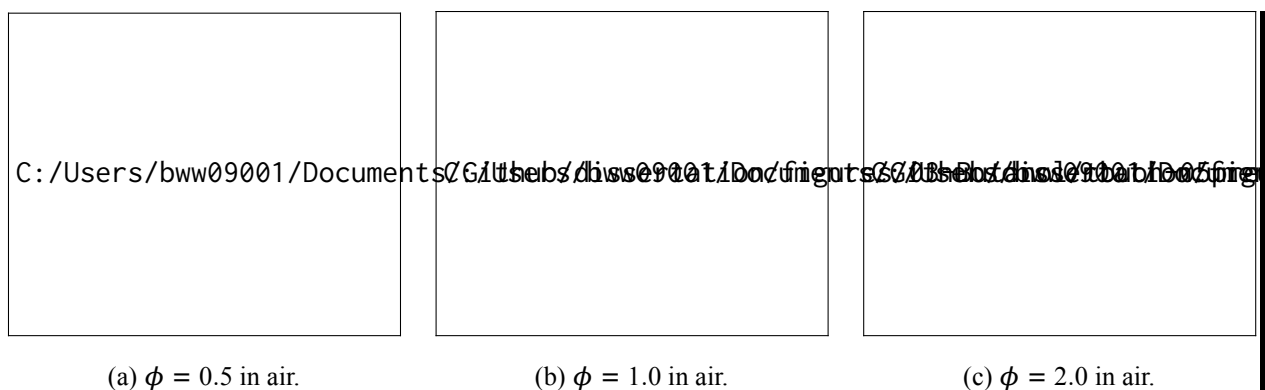
Figure 3.15: Pressure traces of selected *t*-butanol experiments compared with the corresponding non-reactive and simulated traces, using the mechanism of Sarathy et al. [144].

Grana et al. [35], and a doped methane flame by McEnally and Pfefferle [147], ignition delays measured by Stranic et al. [59], JSR species profiles measured by Togbé et al. [148], laminar flame speeds measured by Veloo and Egolfopoulos [31] and Liu et al. [149], and species profiles from a pyrolysis reactor Merchant et al. [146].

Recently, the *i*-butanol model developed by Hansen et al. [34] and Merchant et al. [146] has been updated with new reaction rates and pathways. The updates are detailed in the work of Weber et al. [66]. The primary updates were to add detailed low-temperature peroxy pathways involving *i*-butanol and its primary radicals. This model is still undergoing validation, but is presented here as the state-of-the-art in butanol modeling. This kinetic model will be referred to as the MIT mechanism.

In Fig. 3.16, VPRO simulations at 15 bar and 30 bar using the Sarathy et al. mechanism [144] and the MIT mechanism [66] are shown for *i*-butanol. Some conditions using the MIT mechanism did not ignite during the simulated time (approximately 800 ms), so those points are not shown in Fig. 3.16. The mechanism by Sarathy et al. is in better agreement with the experiments at 15 bar than the MIT model. At 30 bar the MIT model over-predicts the ignition delay—as at 15 bar—while the Sarathy et al. mechanism under-predicts the ignition delay.

Figures 3.17 and 3.18 show comparisons of VPRO simulations using the MIT mechanism with the experimental data at three equivalence ratios with constant initial fuel mole fraction. In general, the model is unable to predict the oxygen concentration dependence of the ignition delays. A similar

Figure 3.16: Comparison of VPRO simulations using the kinetic mechanism of Sarathy et al. [144] (gray) and the MIT mechanism [34, 146] (red) with the experimental ignition delay results (blue) for stoichiometric mixtures of i-butanol in air at $P_C = 15$ bar (squares) and $P_C = 30$ bar (circles).

result was found for the comparison of n-butanol experiments with a model constructed using the same principles as the present model for i-butanol [64]. Moreover, comparing the experimental results with modeling results using the mechanism of Sarathy et al. [144] reveals a similar qualitative discrepancy, although the Sarathy et al. model tends to under-predict the experimental ignition delays whereas the MIT model tends to over-predict the experimental values. The reason for these diverging predictions will be explored and discussed in Sec. 3.5.1.

3.5 Discussion

The relatively good agreement of the mechanism of Sarathy et al. [144] with the experimental data as shown in Figs. 3.12 and 3.13, even for conditions at which the mechanism has not been validated, suggests that using the mechanism to further interpret the experimental data is a worthwhile exercise. In particular, Figs. 3.19–3.22 show the initial steps of the fuel breakdown process for each isomer.

Figure 3.17: Comparison of the experimentally measured ignition delays of *i*-butanol at three equivalence ratios and $P_C = 15$ bar with VPRO simulations using the MIT mechanism.
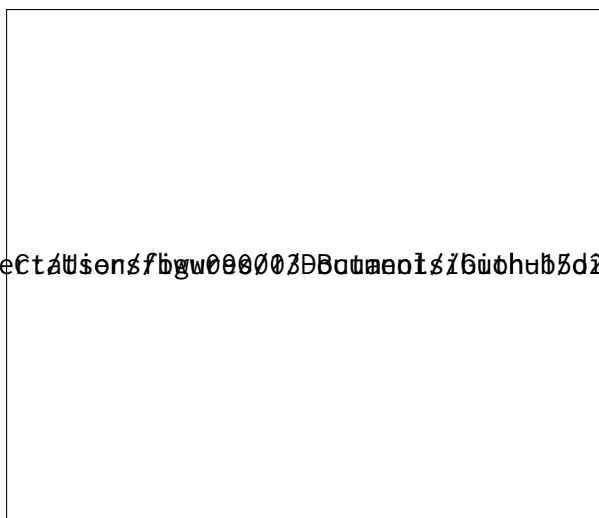
Figure 3.18: Comparison of the experimentally measured ignition delays of *i*-butanol at three equivalence ratios and $P_C = 30$ bar with VPRO simulations using the MIT mechanism.

The percentages listed are the percent of the reactant that is consumed to produce the product shown, by all the reactions that can produce that product from the reactant, except where one particular reaction is noted. These numbers are determined by integrating the rate of production or consumption of each species by each reaction up to the point of 20 % fuel consumption, and normalizing each reaction by the total produced or consumed of each species up to that point. The 20 % fuel consumption point is chosen because it is before small molecule chemistry takes over to drive the ignition, and it has been used previously [64, 144]. The rates of production are taken from a CONV simulation, with initial conditions of 750 K and 15 bar as well as 750 K and 30 bar. These conditions are representative of typical conditions after compression in the present RCM experiments. The plain text percentages on top of the arrows are the 15 bar case and the bold numbers underneath are for the 30 bar case.

In the following discussion, carbon-centered radicals are labeled according to their distance from the hydroxyl moiety in the fuel molecule, as shown in Fig. 3.1. As expected at the relatively low temperature of this analysis, H-abstraction reactions dominate over unimolecular decomposition for all four isomers. It is also expected that *n*-, *s*-, and *i*-butanol react primarily to their respective α-hydroxybutyl radicals, since the α C-H bond has the lowest energy [144]. Due to its unique

63
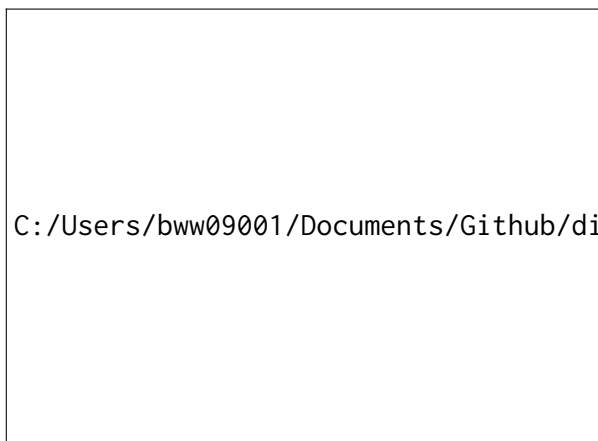
Figure 3.19: Pathway analysis for simulations of *n*-butanol at temperature of 750 K, in stoichiometric air, using the mechanism of Sarathy et al. [144]. Percentages in normal text represent an initial condition of 15 bar; bold text is for 30 bar.
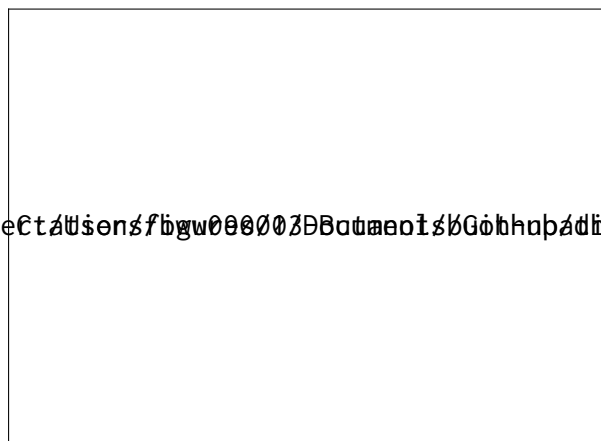
Figure 3.20: Pathway analysis for simulations of *s*-butanol at temperature of 750 K, in stoichiometric air, using the mechanism of Sarathy et al. [144]. Percentages in normal text represent an initial condition of 15 bar; bold text is for 30 bar.
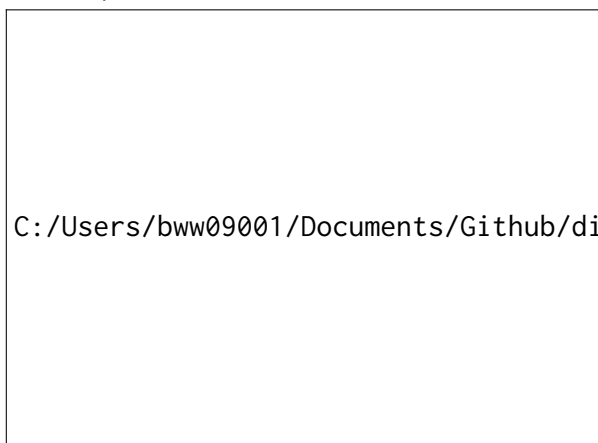
Figure 3.21: Pathway analysis for simulations of *t*-butanol at temperature of 750 K, in stoichiometric air, using the mechanism of Sarathy et al. [144]. Percentages in normal text represent an initial condition of 15 bar; bold text is for 30 bar.
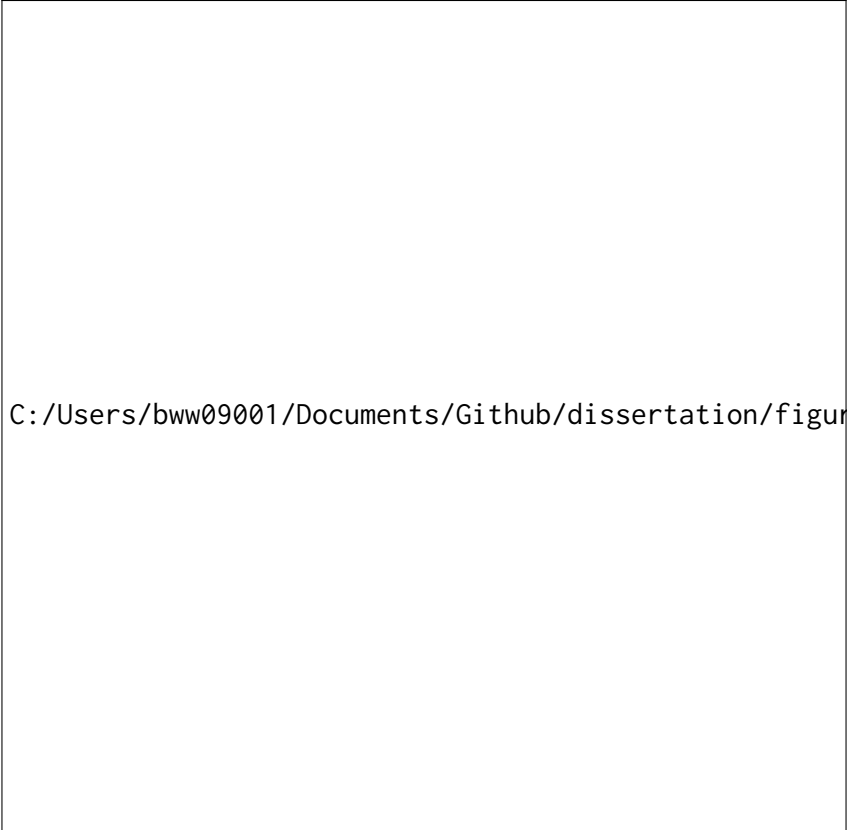
Figure 3.22: Pathway analysis for simulations of *i*-butanol at temperature of 750 K, in stoichiometric air, using the mechanism of Sarathy et al. [144]. Percentages in normal text represent an initial condition of 15 bar; bold text is for 30 bar.

structure, t-butanol does not have an α-hydroxybutyl radical that can be formed by H-abstraction, so t-butanol is primarily consumed to form the β-hydroxybutyl radical, because the O-H bond energy is much higher than β C-H bond energies.

The unique structure of t-butanol continues to affect the second level of reactions. In the temperature and pressure regime investigated, t-butanol tends to add to molecular oxygen at the carbon radical site, forming a hydroxybutylperoxy (RO_2) species. That this pathway is dominant is due to the fact that t-butanol has no α-hydroxybutyl radical. For the other three butanol isomers that do have an α-hydroxybutyl radical, the second level of reactions primarily produces an aldehyde + HO_2 by direct reaction—no hydroxybutylperoxy adduct is formed in this reaction, and there is no possibility for typical hydrocarbon low-temperature chain branching. Therefore, it is hypothesized that the pre-ignition heat release seen in t-butanol is caused by the oxygen addition to the fuel radical to form β-hydroxybutylperoxy, which is an exothermic reaction.

Figure 3.23 shows the total cumulative heat release of each isomer and the cumulative heat release of an important reaction for each of the isomers (inset), from a CONV simulation with initial conditions of 750 K and 30 bar; analysis of 15 bar results is substantially similar. The cumulative heat release in the inset is found by integrating the heat release by each reaction with respect to time, while the reactions shown are the respective reactions that have released the most heat up to the 20 % fuel consumption point for each isomer. The abscissa of the plot is the fuel conversion, in percent. This choice of x-axis allows a fair comparison of the heat release, because the ignition delays of each isomer are markedly different, so comparing the heat release with a time axis is more difficult. In Fig. 3.23, exothermicity is represented by positive quantities.

In Fig. 3.23, it is clear that t-butanol has higher heat release at low fuel consumption (during the induction period) than the other three isomers. In addition, the primary heat release reaction for t-butanol has created much more heat than the primary reactions of the other three isomers. As the reactions proceed, and the temperature increases, the reverse reaction in the t-butanol case becomes more important, and the heat release contribution of this oxygen-addition reaction levels off. The dominance of this reaction at early times is unique to t-butanol ignition, and appears to be driving

65

Figure 3.23: Total cumulative heat release and cumulative heat release by important reactions (inset) as a function of fuel consumption from a simulation using the mechanism of Sarathy et al. [144] with initial conditions of 750 K and 30 bar, in stoichiometric air. See Fig. 3.24 for definitions of reactions in the inset.

the pre-ignition heat release.

Other researchers have also undertaken studies of the low to intermediate temperature combustion of *t*-butanol. Lefkowitz et al. [39] performed a study in the Variable Pressure Flow Reactor (VPFR) at Princeton University on the oxidation of *t*-butanol over the temperature range from 680 K to 950 K, at 12.5 atm and stoichiometric mixture conditions. It is interesting to note that they found no evidence of traditional hydrocarbon low temperature chemistry. They did, however, find significant quantities of acetone, peaking at approximately 800 K. Lefkowitz et al. [39] concluded that the primary pathways of acetone formation are tautomerization of propen-2-ol and β-scission of the alkoxy radical, based on an analysis of the mechanism from Grana et al. [35]. Both of these pathways are dependent on unimolecular decomposition of the hydroxybutyl radicals. However, this mechanism has only been validated for flame studies; indeed, an updated version of this model (by Frassoldati

R1:

R2:

R3:

R4:

Figure 3.24: Reactions causing the most heat release in the ignition of the butanol isomers. The reaction number refers to Fig. 3.23.

et al. [145]) is unable to predict the low-temperature ignition delays measured in this study and hence is not considered for analysis.

In contrast to the study of Lefkowitz et al. [39], path analysis of the mechanism by Sarathy et al. [144] shows that unimolecular decomposition of the hydroxybutyl radicals is not the most important pathway; as mentioned earlier, the most important pathway is the formation of β-hydroxybutylperoxy. Further analysis shows that the primary pathway of reaction of the t-butanol β-hydroxybutylperoxy species is through the Waddington mechanism. The Waddington mechanism has been shown experimentally to be an important pathway for β-hydroxypentylperoxy radicals in the low temperature combustion of i-pentanol [76], as well as the β-hydroxybutylperoxy radicals of i- and t-butanol [150]. t-Butanol only produces β-hydroxybutyl radicals, and one of the products of the Waddington pathway in t-butanol is acetone (the others are formaldehyde and hydroxyl radical); over 88 % of the acetone produced up to the 20 % fuel consumption point is produced by the Waddington reaction. The study in the VPFR thus provides further evidence of the importance of low-temperature hydroxybutylperoxy chemistry in t-butanol, although it is not traditional hydrocarbon low-temperature chemistry.

Up to this point, the discussion has focused mainly on the importance of hydroxybutylperoxy

chemistry in *t*-butanol. Nevertheless, the chemistry of the hydroxybutylperoxy species is important in the combustion of the other isomers of butanol as well. Using the high pressure ST at RWTH Aachen University, Vranckx et al. [62] showed the importance of peroxy chemistry pathways in the autoignition of *n*-butanol. By adding a lumped peroxy model to an existing kinetic model for *n*-butanol combustion, they were able to substantially improve agreement of the model with their experiments at high pressure and low temperature [62].

3.5.1   Comparison of *i*-Butanol Mechanisms

As discussed in Sec. 3.4.3, the Sarathy et al. mechanism [144] tends to under-predict the experimental ignition delays of *i*-butanol, whereas the MIT mechanism [66] tends to over-predict the experimental data. Some of the differences between the mechanisms are demonstrated by the path flux diagram shown in Fig. 3.25. The diagram is produced by the same procedure as Figs. 3.19–3.22, except the initial conditions of the simulation considered in Fig. 3.25 are 810 K and 30 bar for a stoichiometric mixture of *i*-butanol with air. The percentages in plain text are the results from a simulation with the MIT mechanism [66]; the percentages in italics are from a simulation with the Sarathy et al. mechanism [144].

Only the pathways for the α- and β-hydroxybutyl radicals are shown in Fig. 3.25; analysis of the γ-hydroxybutyl and isobutoxy radicals shows similar important pathways for both mechanisms. Figure 3.25 shows that there is a good agreement between the mechanisms in the first step of fuel decomposition, although the MIT mechanism tends to form slightly more β-hydroxybutyl and slightly less α-hydroxybutyl than the Sarathy et al. mechanism. The subsequent reactions of the primary fuel radicals are also similar between the mechanisms, although the formation of α-hydroxybutylperoxy occurs nearly twice as much in the Sarathy et al. mechanism as in the MIT mechanism.

In the third level of reactions, large differences between the models can be noted from Fig. 3.25. In the pathway of the β-hydroxybutyl radical, it can be seen that the breakdown of the β-hydroxybutylperoxy radical occurs partially via the Waddington mechanism to form acetone, formaldehyde and hydroxyl
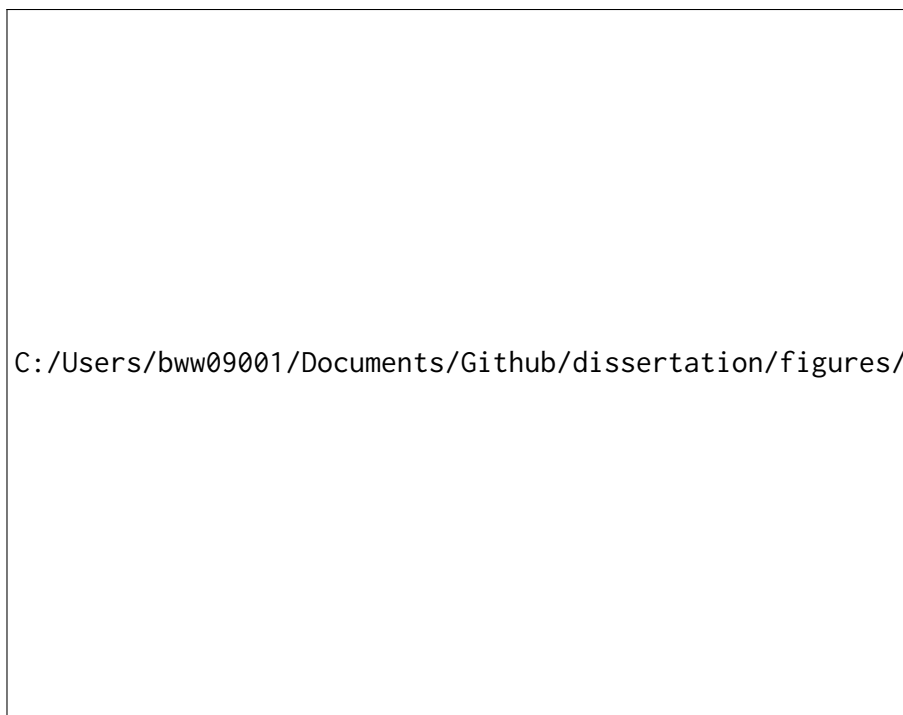
Figure 3.25: Path flux diagram for i-butanol/O_2/N_2, $\phi = 1.0$, $810\,\mathrm{K}$, $30\,\mathrm{bar}$. Plain text indicates the MIT mechanism [66]; italic text indicates the Sarathy et al. mechanism [144].

(OH) in the Sarathy et al. mechanism, whereas this pathway is not active in the MIT mechanism. This pathway is included in the MIT model but is not active under the conditions of this simulation.

Moreover, the fate of the α-hydroxybutylperoxy species is among the most important pathways in controlling the reactivity of the model and shows significant differences between the models. In the MIT mechanism, nearly all of the α-hydroxybutylperoxy goes to form isobutyraldehyde, which is itself the primary product of reactions of α-hydroxybutyl. This means that over 99 % of the α-hydroxybutyl radical is directed into the formation of isobutyraldehyde and hydroperoxyl (HO_2) in the MIT mechanism. However, in the Sarathy et al. mechanism, only about a quarter of the α-hydroxybutylperoxy goes to form isobutyraldehyde, and the rest is directed into traditional hydrocarbon low-temperature chain branching pathways leading to the formation of the hydroxyl radical.

The pathways involving α-hydroxybutyl and its products is of critical importance because the radical species produced from these pathways control the reactivity of the model. In the mechanism of Sarathy et al. [144], the radical that primarily controls i-butanol decomposition is hydroxyl,

whereas in the MIT model [66], the reactivity is controlled by the hydroperoxyl radical.

In their work, Sarathy et al. [144] used the reaction rates computed by Silva et al. [151] for the hydroxyethyl system (i.e. ethanol as the parent fuel) to determine the rate of direct reaction of α-hydroxybutyl and oxygen to form aldehyde and HO_2, and then set the rate of oxygen addition to the α-hydroxybutyl radical (to form α-hydroxybutylperoxy) so that the total rate was less than the collisional limit. The rates of oxygen addition for the other radicals were prescribed depending on the type of carbon (primary, secondary, or tertiary) based on studies of butane and i-octane [144]. Based on the well-known importance of hydroxyl in driving the reactivity of combustion systems, and the sources of the estimates for the reaction rates of oxygen addition to hydroxybutyl (i.e. the entry to the pathway that controls the rate of hydroxyl formation), it can be hypothesized that the rates of hydroxybutylperoxy formation are overestimated in the mechanism of Sarathy et al. [144], as the simulated results under-predict the experimental data of i-butanol.

This hypothesis is supported by the results shown in Fig. 3.26, which shows the linear brute force sensitivity of the ignition delay (τ) of i-butanol with respect to changes in the A-factor of the rate coefficient, using the mechanism from Sarathy et al. [144]. The percent sensitivity is defined as the difference between the ignition delay when the A-factor of each reaction is halved and the nominal ignition delay, normalized by the nominal ignition delay, as shown below:

$$S_i = \frac{\tau(0.5A_i) - \tau(A_i)}{\tau(A_i)} \times 100\,\% \tag{3.1}$$

Therefore, negative sensitivity means that halving the A-factor of a reaction decreases the ignition delay, and positive sensitivity indicates the ignition delay increases. These results are for CONV simulations with initial conditions of 750 K and 30 bar as well as 1200 K and 30 bar.

The most sensitive reaction at the lower temperature is the initiation reaction of the fuel with hydroperoxyl radical to form the primary fuel radical and the second most sensitive reaction is the addition of oxygen to the primary radical. Both of these reactions have positive sensitivities, indicating that reducing the rate of these reactions increases the ignition delay and improves the agreement of the simulations relative to the experiments in this case. It is apparent, then, that

70

C:/Users/bww09001/Documents/Github/dissertation/figures/03-Butanol/buoh-sen

Figure 3.26: Linear brute force sensitivity analysis of the ignition delay with respect to the A-factors of the listed reactions in the mechanism from Sarathy et al. [144]. Positive quantities indicate the ignition delay is increased when the A-factor is halved.

reducing the amount of fuel propagating into the low temperature chain branching pathway of oxygen addition to the primary α-radical improves the simulated results. Interestingly, the i-butanol system is not sensitive to the rates of oxygen addition to the hydroxybutyl radicals other than the α-radical. At the higher temperature of 1200 K, there is little sensitivity on the ignition delay by changing the rate of the oxygen-addition reaction, demonstrating its lack of influence at higher temperatures.

As a final comparison, we have modified this pathway in the mechanism from Sarathy et al. [144] so that the rate of oxygen addition to the primary fuel radical is arbitrarily set to zero; that is, the rate of the reaction ic4h8oh-1+o2=ic4h8oh-1o2 is set to zero by zeroing the A-factor, while the rates of the other oxygen addition reactions were unchanged. This unphysical situation substantially changes the results of simulations for i-butanol—removing this pathway in the mechanism from Sarathy et al. [144] brings the simulations into close agreement with the ignition delay results from the MIT mechanism. In the MIT mechanism, the reactions of α-hydroxybutylperoxy exclusively produce i-butyraldehyde, whereas in the Sarathy et al. mechanism, some of the α-hydroxybutylperoxy radicals enter chain-branching pathways. Since the other oxygen addition reactions were unchanged, it is apparent that the addition of oxygen to α-hydroxybutyl is one of the controlling reactions for the high-pressure, low-temperature ignition of i-butanol using the mechanism of Sarathy et al. [144]. It is therefore concluded that a detailed examination of the rates of direct formation of aldehyde+HO$_2$ and oxygen addition to the α-hydroxybutyl radical are required to better predict the low-temperature ignition behavior of i-butanol. Furthermore, based on the other results of this study, a detailed analysis of the oxygen addition reactions to all the isomers of butanol is probably warranted.

3.6 Conclusions

In this work, ignition delays for all four isomers of butanol in stoichiometric mixture with air have been presented over the low to intermediate temperature range, and at two compressed pressures of 15 bar and 30 bar. The order of reactivity of the isomers is n-butanol$>$$s$-butanol$\approx$$i$-butanol$>$$t$-butanol

at the lower pressure, but changes to n-butanol>t-butanol>s-butanol>i-butanol at the higher pressure. This unexpected result is partially explained by the fact that there is substantial pre-ignition heat release present for t-butanol. To help understand the nature of the pre-ignition heat release of t-butanol, studies at off-stoichiometric conditions, $\phi = 0.5$ and $\phi = 2.0$ in air, are also conducted.

Comparisons of the experimentally measured ignition delays with two kinetic mechanisms show good agreement for certain isomers, but relatively poorer agreement for others. The kinetic mechanism of Sarathy et al. [144] is used to further elucidate the chemical processes controlling the autoignition of these butanol isomers. Pathway analysis of the fuel decomposition shows that n-, s-, and i-butanol primarily form α-hydroxybutyl radicals, because the proximity of the α carbon to the hydroxyl group reduces the C-H bond energy. The α-hydroxybutyl radicals tend to form an aldehyde plus HO_2 directly, without forming a hydroxybutylperoxy complex. However, due to its unique structure, t-butanol can only form β-radicals; these radicals do not have the tendency to react with oxygen to directly form HO_2 and an aldehyde. Rather, t-butanol preferentially adds oxygen to the fuel radical site. It is hypothesized that this reaction, O_2 addition to form hydroxybutylperoxy, causes the pre-ignition heat release in t-butanol and leads to a chain propagation pathway through the Waddington mechanism. The fact that this oxygen-addition reaction is preferred is unique to t-butanol, although a detailed understanding of the peroxy chemistry of alcohols is still of vital importance to the other butanol isomers. This is further demonstrated in this work for the case of i-butanol, where the ignition delay is quite sensitive to both the rate of primary fuel radical formation and to the rate of oxygen addition to the primary fuel radical. It is also noted that n-butanol autoignition was quite sensitive to peroxy chemistry in the study of Vranckx et al. [62].

All together, these analyses show the importance of the peroxy chemistry pathways in the autoignition of the butanols. Further experimental studies, such as species profiles from the low temperature ignition of the butanol isomers, could help reduce uncertainty in the pathways of fuel breakdown. Finally, further understanding of the rates of the peroxy pathways is important and therefore further theoretical and quantum chemical studies are warranted.

Chapter 4

i-Pentanol

Table 4.1: HHV of Ethanol, *i*-Pentanol, and Gasoline

Compound	Ethanol [21]	*i*-Pentanol [21]	Gasoline [22]
HHV [MJ/kg]	29.67	37.73	48.46

```
C:/Users/bww09001/Documents/Github/
```

Figure 4.1: Skeletal structure of *i*-pentanol

4.1 Structure of *i*-Pentanol

i-Pentanol (3-methyl-1-butanol) is a five-carbon alcohol whose skeletal structure is shown in Fig. 4.1. The carbon atoms in Fig. 4.1 are labeled according to their distance from the hydroxyl moeity, with α being the closest and δ being the farthest. The Greek letter notation will be used to refer to the carbon-centered radicals in Sec. 4.5. *i*-Pentanol can be produced biologically [20], and offers several similar advantages as the butanol isomers compared to ethanol. Table 4.1 compares the HHV of ethanol, *i*-pentanol, and gasoline.

Table 4.2: *i*-pentanol Experimental Conditions

Reactant (Purity)			Equivalence Ratio ϕ	Compressed Pressure P_C (bar)
i-pentanol (99.6 %)	O$_2$ (99.994 %)	N$_2$ (99.999 %)		
Mole Percentage				
2.41	20.50	77.09	1.0	40
1.22	20.75	78.03	0.5	40
4.71	20.01	75.27	2.0	40

4.2 Procedures

Experiments for *i*-pentanol in the RCM have been performed at the conditions listed in Table 4.2. Homogeneous fuel and air pre-mixtures are prepared in an approximately 17 L mixing tank. The mixing tank and all tubes and manifolds connecting the tank with the RCM are heated, allowing the study of relatively low vapor pressure fuels. The initial temperature is set above the saturation temperature of *i*-pentanol for each mixture studied. The mixing tank is equipped with a magnetic stirrer to ensure complete homogeneity of the mixture.

Prior to mixture preparation, the mixing tank is vacuumed to less than 1 torr, whereupon liquid fuel (*i*-pentanol, Sigma-Aldrich, 99.6 % purity) is injected by a syringe through a septum. The syringe is massed before and after the injection, with the difference being the amount of fuel in the mixing tank. Based on this mass, required proportions of the gaseous oxidizer (O2, 99.994 % purity, N2, 99.999 % purity) are calculated. The gases are added to the mixing tank sequentially at room temperature and the total pressure is monitored to ensure that the proper mixture concentrations are attained. Finally, the heaters and stirring vane are switched on and the system is allowed approximately 1.5 h to reach steady state.

4.3 Model Improvements

Through collaboration with researchers at Lawrence Livermore National Laboratory, many improvements to the chemical kinetic model for *i*-pentanol were made relative to the work of Tsujimura et al. [77]. Some of the major improvements are highlighted below; see the article for more detail [75].

1. The model was restructured based on work with C_4 and C_5 alcohols [144, 152]

2. The most stable conformers of *i*-pentanol were calculated using quantum chemistry software

3. The BDEs of the of the C-C, C-H, C-O, and O-H bonds were calculated using quantum chemistry software

4. The model includes the Waddington pathway shown to be important in low-temperature decomposition of *i*-pentanol by Welz et al. [76]

5. New reaction pathways were added based on the work of Welz et al. [76, 153], including the unconventional water-elimination pathway discussed in Welz et al. [153]

Moreover, the following data sets from the literature and presented in the work of Sarathy et al. [75] were used to validate the newly updated model, in addition to the new data at $P_C = 40$ bar presented here.

1. Ignition delays measured in a ST and an RCM[77, 78]

2. JSR species data [73]

3. New ignition delays measured in STs [75]

4. New JSR species data [75]

5. New flame speed and flame extinction measurements [75]

4.4 Experimental & Modeling Results

The experimental ignition delays measured in the RCM are shown in Figs. 4.2, 4.3, and 4.4, along with ignition delays measured in the ST and comparison with the model simulations. There is no $\phi = 2.0$ data set for 7 atm because no conditions at which ignition occurred could be found. In Figs. 4.2–4.4, solid lines represent adiabatic, constant volume simulations, and dashed lines represent volume-profile simulations.

At 7 atm (Fig. 4.2), the high-temperature ignition delays measured in the ST are generally predicted to within a factor of 1.5. The RCM experiments are also well predicted at low temperature—within a factor of 2—but the disagreement grows to approximately a factor of 4 in the intermediate temperature regime. At 20 atm (Fig. 4.3), the high-temperature ignition delays are well predicted, including capturing the equivalence ratio sensitivity of the ignition delays. The ignition delays measured in the RCM are fairly well predicted at the lean and stoichiometric conditions, but are over-predicted at the rich condition.

At 40 atm (Fig. 4.4), the model is able to reproduce the high-temperature ignition delays fairly well, including capturing the equivalence ratio dependence of the ignition delays. Ignition delay data near 40 atm and temperatures ranging from 651 K to 776 K were also acquired using the RCM. The ignition data in the RCM and ST are in good qualitative agreement, displaying the expected decrease in ignition delay with increasing temperature. The model well predicts the observed trend of decreasing ignition delay time with increasing equivalence ratio, which occurs because a higher fuel concentration results in greater radical production at these conditions. Constant volume and volume history simulations at the 40 atm RCM conditions (Fig. 4.4) indicate the model can well predict ignition delay times at stoichiometric conditions, but cannot well predict RCM ignition delay data at lean and rich conditions. The difference (i.e., spread) in ignition delay times across various equivalence ratios is similar to that observed for other alcohols in the same facilities (e.g., *n*-butanol at 15 bar [64] and *t*-butanol at 30 bar [65]). The primary issue with the model is its equivalence ratio sensitivity; predicted ignition delay times need to be increased at lean conditions yet decreased

C:/Users/bww09001/Documents/Github/dissertation/figures/04-Pentanol/ipeoh-7

Figure 4.2: ST and RCM ignition delay times from Tsujimura et al. [77] at 7 atm compared with model predictions by the model from Sarathy et al. [75].

C:/Users/bww09001/Documents/Github/dissertation/figures/04-Pentanol/ipeoh-2

Figure 4.3: ST and RCM ignition delay times from Tsujimura et al. [77] at 20 atm compared with model predictions by the model from Sarathy et al. [75].

C:/Users/bww09001/Documents/Github/dissertation/figures/04-Pentanol/ipeoh-4

Figure 4.4: ST and RCM ignition delay times from Sarathy et al. [75] at 40 atm compared with model predictions by the model from Sarathy et al. [75].

C:/Users/bww09001/Documents/Github/dissertation/figures/04-Pentanol/ipeoh-p

Figure 4.5: Experimental reactive (red), simulated reactive (blue), and experimental non-reactive (gray) pressure profiles at 40 atm for lean *i*-pentanol/air mixtures.

C:/Users/bww09001/Documents/Github/dissertation/figures/04-Pentanol/ipeoh-p

Figure 4.6: Experimental reactive (red), simulated reactive (blue), and experimental non-reactive (gray) pressure profiles at 40 atm for stoichiometric *i*-pentanol/air mixtures.

C:/Users/bww09001/Documents/Github/dissertation/figures/04-Pentanol/ipeoh-p

Figure 4.7: Experimental reactive (red), simulated reactive (blue), and experimental non-reactive (gray) pressure profiles at 40 atm for rich *i*-pentanol/air mixtures.

at rich conditions, implying that the system's reactivity is controlled by different phenomenon at different equivalence ratios. At these low temperatures the model's reactivity is driven by the overall peroxy reaction sequence, $R+O_2=ROO=QOOH(+O_2)=OOQOOH=2OH+products$, including the inhibitive direct (i.e., concerted) HO_2 elimination and QOOH decomposition routes. An increase (or decrease) in any reaction rate constant along this reaction sequence will move the reactivity of the system in the same direction at all equivalence ratios. Therefore, we were unable to identify a single reaction rate constant modification that would decrease overall reactivity at lean conditions while increase it at rich conditions.

Representative experimental and simulated pressure profiles for the lean, stoichiometric, and rich conditions are shown in Figs. 4.5, 4.6, and 4.7 respectively, with the profiles shifted so EOC occurs at 0 s. Interestingly, the experimental pressure traces after the induction period do not show a sharp increase in pressure (i.e., heat release is more gradual, similar to two-stage ignition). For the lean case, there is a moderate heat release 25 ms after EOC followed by a larger heat release event, and similar behavior is observed at other equivalence ratios. It is noted that similar heat release prior to the main ignition event was found in an HCCI engine experiment using *i*-pentanol by Yang et al. [81] and was termed Intermediate Temperature Heat Release (ITHR) in their work.

The pressure profile of the present simulations qualitatively agrees with the experimental data, in that the simulated pressure traces deviate from the non-reactive trace prior to the main ignition event, although the ignition delay itself does not necessarily agree very well. For lean and stoichiometric cases the simulated ignition delay times are fast compared to the data, whereas at rich conditions they are too slow.

4.5 Discussion

The sensitivity of the ignition delay to changes in the reaction rate coefficients is shown in Fig. 4.8 for a constant volume, adiabatic simulation at 20 atm, 800 K, and for equivalence ratios varying

from $\phi = 0.5$ to 2.0. The percent sensitivity is computed by the formula:

$$S = \frac{\tau(2k_i) - \tau(k_i)}{\tau(k_i)} \times 100\,\% \tag{4.1}$$

where $\tau(2k_i)$ is the ignition delay when the rate coefficient of reaction i is doubled, and $\tau(k_i)$ is the nominal ignition delay. Positive sensitivities therefore represent an increase in the ignition delay when the rate coefficient of reaction i is increased. Both the forward and reverse rates of each reaction are increased simultaneously. Since the reaction 2ho2⇔h2o2+o2 is represented by two sets of A, b, and E_a in the reaction mechanism, both Arrhenius coefficients were simultaneously doubled to give the sensitivity value shown in Fig. 4.8.

It is seen from Fig. 4.8 that the most sensitive reaction under these conditions is H-abstraction by OH to form the α-hydroxypentyl radical (ic5h10oh-1). Increasing the rate of abstraction by OH from the α site increases the ignition delay because subsequent reaction of the fuel radical with O_2 leads to the formation of HO_2 and i-pentanal, which is an OH terminating pathway. The next most sensitive reaction is H-abstraction by OH to form the γ-hydroxypentyl radical (ic5h10oh-3). The ignition delay is also sensitive to the rates of isomerization of the ROO radicals formed by the other hydroxypentyl radicals. This indicates that, except for the α radical, the other hydroxypentyl radicals undergo typical low-temperature chain branching reactions. This observation is further corroborated by a reaction path analysis, discussed below. Furthermore, Fig. 4.8 shows that the ignition delay is also sensitive to some low temperature chain terminating pathways, such as formation of an enol + HO_2 from ROO or QOOH radicals.

A sensitivity analysis of the ignition delay to changes in the reaction rate coefficients for initial conditions of 40 atm and 689 K, for three equivalence ratios, is shown in Fig. 4.9. As before, positive sensitivity indicates that increasing the rate coefficient of that reaction increases the ignition delay. Similar to the 20 atm sensitivity analysis, the most sensitive reactions are the H-abstractions from the fuel and the subsequent reactions of these initial fuel radicals. However, stronger equivalence ratio dependence of the sensitivity results is seen in Fig. 4.9 compared to Fig. 4.8. It is interesting to note

that the most sensitive reaction, formation of the α-hydroxypentyl radical through H-abstraction by OH, is nearly twice as sensitive at $\phi = 0.5$ than at $\phi = 2.0$, while most of the other reactions have nearly the same sensitivity for the three equivalence ratios.

In addition, the reaction of formaldehyde and hydroxyl radical to form formyl radical and water is somewhat sensitive, especially for the lean case. The importance of this reaction is demonstrated by the path analysis shown in Fig. 4.10 (similar results are obtained for a path analysis at 40 atm as at 20 atm). Formaldehyde is a significant product in the decomposition of the β- and γ-hydroxypentyl radicals, as well as the pentoxy radical. Furthermore, the reaction of two hydroperoxyl molecules to form hydrogen peroxide and oxygen molecule is the seventh most sensitive reaction. This reaction is important as it releases the most heat during the ITHR period prior to the main ignition for all three equivalence ratios and because the rapid reaction of the α-hydroxypentyl radical to form i-pentanal and hydroperoxyl is important in alcohol combustion. In view of the equivalence ratio dependence shown in Fig. 4.9, these sensitivity analysis results suggest that it may be possible to adjust multiple reaction rates in the low temperature chain branching pathways to decrease reactivity at lean conditions but increase reactivity at rich conditions, which warrants further investigation.

The main i-pentanol reaction pathways after 20 % fuel consumption at 800 K, 20 atm, and for three equivalence ratios are shown in Fig. 4.10, describing the key low temperature reaction pathways. The percent flux of each reaction path is the contribution of that path to destroying the reactant, integrated up to 20 % fuel consumption. The fuel is mainly consumed by the H atom abstraction at the α site because i-pentanol has a weak C-H bond at the α site. As discussed previously, subsequent reactions of α-hydroxypentyl with O_2 generate i-pentanal + HO_2, an OH terminating pathway. The other hydroxypentyl radicals tend to add to molecular oxygen and form hydroxyalkylperoxy (ROO) radicals. These radicals are mainly isomerized to hydroxyalkylhydroperoxide (QOOH) or decomposed to enol species by the concerted elimination of HO_2. Approximately 18 % of β-hydroxyalkylperoxy radicals are decomposed to produce i-butanal (2-methylpropanal), formaldehyde, and OH radical via ROO isomerization and β-scission reactions by the Waddington mechanism [154, 155]. It is also interesting to note that a similar pathway involving hydrogen

C:/Users/bww09001/Documents/Github/dissertation/figures/04-Pentanol/ipeoh-2
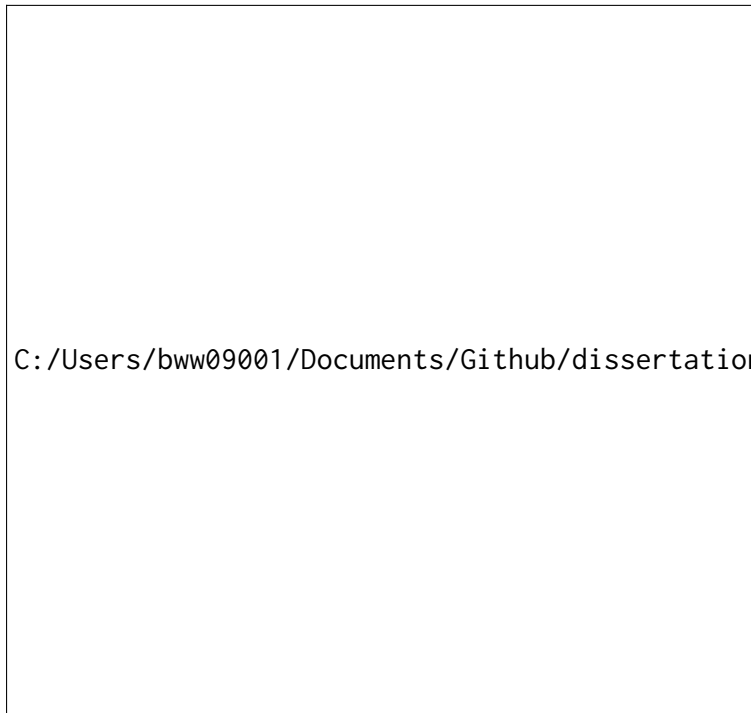
Figure 4.8: Sensitivity of the ignition delay to changes in the reaction rate coefficients for three equivalence ratios. Initial conditions for constant-volume adiabatic simulations are 800 K and 20 atm.

C:/Users/bww09001/Documents/Github/dissertation/figures/04-Pentanol/ipeoh-4

Figure 4.9: Sensitivity of the ignition delay to changes in the reaction rate coefficients for three equivalence ratios. Initial conditions for constant-volume adiabatic simulations are 689 K and 40 atm.

C:/Users/bww09001/Documents/Github/dissertation/figures/04-Pentanol/ipeoh-20path.pdf

Figure 4.10: Reaction path analysis for i-pentanol at 800 K, 20 atm, and three equivalence ratios, based on constant-volume adiabatic simulations. Plain text: $\phi = 0.5$. Bold text: $\phi = 1.0$. Italic text: $\phi = 2.0$. The flux is integrated up to 20 % fuel consumption.

transfer from the OH group is important for the γ-ROO (6 %) via a 7-membered transition state ring, which is a reaction sequence we included based on the work of Welz et al. [76].

4.6 Conclusions

New experimental ignition delay data have been collected in an RCM at conditions of 40 atm, $\phi = 0.5$ to 2.0, and temperatures below 800 K. The measured pressure histories showed interesting behavior of slow initial pressure rise prior to a sharp pressure rise indicating overall ignition. This pressure rise may be attributed to the role of the Waddington mechanism in consuming the fuel via the production and recycling of OH radicals during the pre-ignition phase.

An existing model [77] for i-pentanol combustion has been updated with newly calculated reaction rate coefficients and newly discovered reaction pathways. The updated model was able

to predict the ignition delays measured in the RCM and STs fairly well, although it was unable to reproduce the equivalence ratio sensitivity of the low-temperature RCM ignition delay measurements. The model was also able to qualitatively capture the slow initial pressure rise measured during the RCM experiments, although the model was unable to reproduce the quantitative timing of the pressure rise.

Pathway and sensitivity analyses were conducted to understand the important reactions in the decomposition of *i*-pentanol. The most important path for consumption of fuel radicals at low and intermediate temperatures was the reaction of the α-hydroxypentyl radical with O_2 to form *i*-pentanal and HO_2, a path that does not contribute to the low temperature branching. However, sufficient low temperature chain branching involving the γ and δ fuel radicals occurred in the model that it was able to reasonably reproduce low-temperature ignition and reactivity observed in the experiments. Sensitivity analysis showed that no single reaction can be modified to improve agreement of the model with all of the conditions, and further experimental or computational study is required to identify the cause of the discrepancy in predictions of ignition delay at off-stoichiometric, low-temperature conditions.

Chapter 5

Methylcyclohexane

Table 5.1: Molar Proportions of Reactants in MCH Experiments

Mix #	ϕ	MCH	O_2	N_2	Ar
1	1.0	1	10.5	12.25	71.75
2	0.5	1	21.0	0.00	73.50
3	1.5	1	7.0	16.35	71.15

C:/Users/bww09001/Documents/Githul
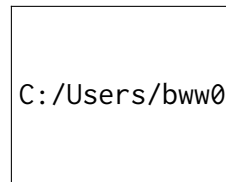
Figure 5.1: Skeletal structure of methylcyclohexane

5.1 Structure of Methylcyclohexane

Methylcyclohexane (MCH) is the simplest branched cycloalkane, and as such, represents an excellent target to use as the base for models of larger branched cycloalkanes. MCH has the elemental composition C_7H_{14}, and its skeletal structure is shown in Fig. 5.1.

5.2 Procedures

The liquid fuel (methylcyclohexane, 99.0 % purity) is massed to a precision of 0.01 g in a syringe before being injected into the mixing tank through a septum. The proportions of oxygen (99.9999 % purity), nitrogen (99.9995 % purity), and argon (99.9999 % purity) are determined by specifying

the oxidizer composition, the equivalence ratio, and the total mass of fuel. The gases are added to the mixing tank manometrically at room temperature.

Three different mixtures of MCH/O$_2$/N$_2$/Ar are prepared in this study, as outlined in Table 5.1. These mixtures (denoted as Mix #1–3) match the mixtures prepared in our previous work with MCH in the RCM [89]. The equivalence ratios corresponding to Mix #1–3 are $\phi = 1.0, 0.5,$ and $1.5,$ respectively. As in the previous RCM experiments, the mole fraction of MCH is held constant and the mole fraction of O$_2$ is varied to adjust the equivalence ratio. This experimental design allows these data to be used to validate chemical kinetic models for changes in O$_2$ concentration, which is an important variable in internal combustion engines where exhaust gas recirculation is used to reduce the oxygen concentrations to avoid NOx formation. Few validation data for ignition are available for changing oxygen concentrations. In addition, the relative proportions of O$_2$, N$_2$, and Ar are adjusted so that the same specific heat ratio is maintained in the three mixtures. As discussed in Sec. 2.1.6, P_C and T_C are assumed to only depend on the temperature-dependent specific heat ratio of the reactants, the compression ratio, and the initial conditions. Thus, for given P_C, compression ratio, and initial conditions, the T_C will be similar for all the equivalence ratios in these experiments.

5.3 Model Improvements

Through collaboration with researchers at Lawrence Livermore National Laboratory (LLNL), many improvements to the chemical kinetic model for MCH were made. Some of the major improvements are highlighted below; see the article for more detail [90]. It should be noted that the improvement relative to the model from 2007 by Pitz et al. [14] is substantial.

1. The base C$_1$–C$_4$ chemistry has been updated with the AramcoMech version 1.3 [9].

2. The aromatics base chemistry was updated with the latest LLNL-NUIG model [156].

3. The cyclohexane sub-model was updated with a new version from Silke et al. [157].

4. Rates of abstraction reactions from MCH have been updated with recently measured experimental values [158] and standardized according to the LLNL reaction rate rules [159].

5. Products of MCH breakdown with unsaturated rings such as methylcyclohexene were previously lumped into one species for simplicity. In the new model, they have been unlumped and provide improved fidelity in modeling these species. [160].

6. The reaction rates of some low-temperature specific reactions were updated using new quantum chemical calculations to compute the rate. Other reaction rates were updated from similar calculations performed by Fernandes et al. [161].

7. The activation energy of the ketohydroperoxide decomposition reactions was increased to bring it into closer agreement with the activation energy used by Metcalfe et al. [9]. This change has a dramatic effect on the low-temperature ignition delays, as shown in Sec. 5.5.

5.4 Experimental Results

The experimental ignition delays measured at the three equivalence ratios and compressed pressure of 50 bar are shown in Fig. 5.2. The open symbols are the overall ignition delays, and the filled symbols are the first stage ignition delays. The vertical error bars on the experimental data represent twice the standard deviation of all of the experiments at that condition as discussed in Sec. 2.1.3. Detailed uncertainty analysis of the deduced compressed temperature was conducted as reported in Sec. 2.1.8.6 where the uncertainty of the compressed temperature was estimated to be approximately 1 %.

The negative temperature coefficient (NTC) region is an important feature of low temperature ignition where the ignition delay time increases with increasing temperature. The NTC region of the overall ignition delay is evident in Fig. 5.2 for the $\phi = 1.5$ case (Mix #3) and approximately includes the temperature range of $T_C = 775\,\text{K}$ to $840\,\text{K}$. For $\phi = 1.5$, first stage ignition is evident for conditions in the range of $T_C = 740\,\text{K}$ to $800\,\text{K}$.

C:/Users/bww09001/Documents/Github/dissertation/figures/05-MCH/mch-expts
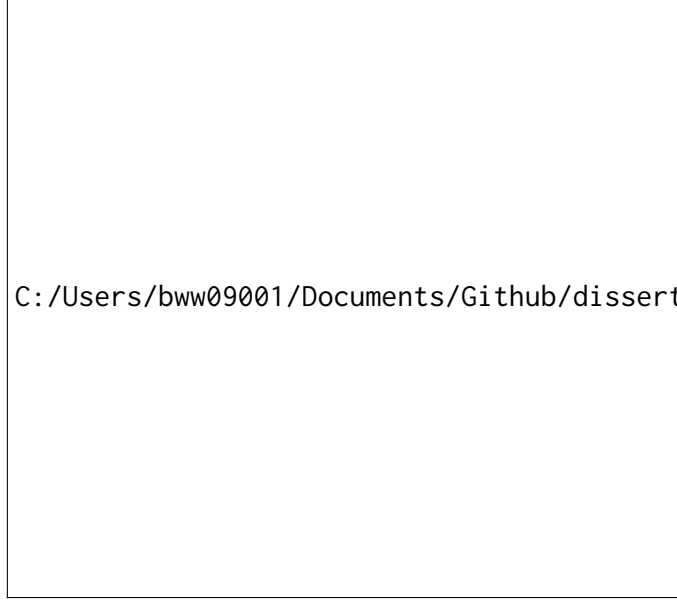
Figure 5.2: Experimentally measured ignition delays at $P_C = 50$ bar for the mixture conditions in Table 5.1

For $\phi = 1.0$ (Mix #1), the NTC region of the overall ignition delay could not be completely resolved. Only three conditions in the low temperature region and three conditions in the high temperature region are shown in Fig. 5.2. The experimental pressure traces during the compression stroke for intermediate temperature conditions deviated from their non-reactive counterparts, demonstrating appreciable reactivity therein. Hence, those data are not included in Fig. 5.2.

For the experiments at $\phi = 0.5$ (Mix #2), only three data points in the low temperature region are reported and none of them exhibit two-stage ignition response. As the temperature is increased further, noticeable reactivity during the compression stroke is evident.

As stated earlier, the mole fraction of MCH is held constant in this study, while the mole fraction of the oxidizer is changed to modify the equivalence ratio. Figure 5.2 demonstrates that the $\phi = 0.5$ case is the most reactive (as judged by the inverse of the ignition delay) and the $\phi = 1.5$ case is the least reactive. As has been shown for other fuels, including *n*-butanol [64] and Jet-A [127], decreasing the equivalence ratio by increasing the oxygen mole fraction but holding the fuel mole fraction constant increases the reactivity.

5.5 Comparison to Model

A comparison of the experimentally measured first stage ignition delays (open symbols) and the first stage ignition delays computed using the updated model (lines) is shown in Figs. 5.3a, 5.4a, and 5.5a for Mix #1, #2, and #3. In addition, a comparison of the experimentally measured overall ignition delays (open symbols) and the overall ignition delay computed by the updated model (lines) is shown in Figs. 5.3b, 5.4b, and 5.5b. The experiments include the new work being presented here at $P_C = 50$ bar in addition to the previous RCM experiments at $P_C = 15.1$ bar and 25.5 bar [89]. The simulations are of the VPRO type. For some computational cases, substantial heat release during the compression stroke caused the computed pressure to depart from the non-reactive profile prior to EOC. Therefore, these cases are not shown in Figs. 5.3–5.5. For these conditions, the experimental pressure trace did not exhibit significant heat release during the compression stroke and the experimental pressure at EOC for the reactive case matched that of the non-reactive counterpart.

At 15.1 bar and 25.5 bar for Mix #1 and #2, the overall ignition delay is very well predicted for temperatures above approximately 715 K. For lower temperatures at these two equivalence ratios, the experimental ignition delays are under-predicted by the model, but the predictions are nevertheless within a factor of two of the data. For the rich case (Mix #3), the simulations under-predict the ignition delay over a wider temperature range but the results improve as temperature increases. Again, the experimental ignition delays are predicted to within approximately a factor of two. At 50 bar, the ignition delays are under-predicted for all of the equivalence ratios studied here, but the agreement is within a factor of two.

The first stage ignition delays for all of the pressure and equivalence ratios are under-predicted, but are within a factor of three of the experimental values. Furthermore, for all of the equivalence ratios tested at $P_C = 50$ bar, it is of interest to note that there are several cases where simulated ignition delays show two-stage response where the experiment shows only a single stage ignition. Nevertheless, the present mechanism is a marked improvement from the comparison performed by

(a) First stage ignition delays   (b) Overall ignition delays

Figure 5.3: Comparison of experimental and simulated ignition delays for three pressures for Mix #1. The data at 15.1 bar and 25.5 bar are from the study of Mittal and Sung [89].

(a) First stage ignition delay   (b) Overall ignition delay

Figure 5.4: Comparison of experimental and simulated ignition delays for three pressures for Mix #2. The data at 15.1 bar and 25.5 bar are from the study of Mittal and Sung [89].

(a) First stage ignition delay   (b) Overall ignition delay

Figure 5.5: Comparison of experimental and simulated ignition delays for three pressures for Mix #3. The data at 15.1 bar and 25.5 bar are from the study of Mittal and Sung [89].

Mittal and Sung [89] who found that the ignition delays were strongly and uniformly over-predicted by the previous LLNL mechanism by Pitz et al. [14].

Figure 5.6 shows a comparison of selected simulated and experimentally measured pressure traces for Mix #1, #2, and #3 at $P_C = 50$ bar. Also shown in Fig. 5.6 is the simulated non-reactive pressure trace corresponding to each experimental condition. Small differences in the heat loss profile for different temperatures are apparent in the non-reactive pressure traces. These differences arise from the changing surface area to volume ratio of the reaction chamber at the end of compression as the compression ratio is changed to vary the compressed temperature. This highlights the importance of using VPRO simulations to compare predictions of ignition delay with the experimental data.

For Mix #1, it is clear that the simulated reactive pressure trace in Fig. 5.6a at $T_C = 866$ K (red dashed line) deviates from the non-reactive pressure trace (red dot-dot-dashed line) prior to the end of compression. The same is also true of the 797 K case shown for Mix #3 in Fig. 5.6c. Remarkably, the simulated case for Mix #1 at $T_C = 866$ K (Fig. 5.6a, red dashed line) predicts the overall ignition delay quite well. However, due to the heat release prior to EOC, this simulated result is not plotted in Fig. 5.3. The simulated case for Mix #3 at $T_C = 797$ K is also not plotted on Fig. 5.5 due to the heat release prior to EOC; interestingly, this case under-predicts the first stage ignition delay but over-predicts the overall ignition delay. For the other simulated cases (black lines), the reactive pressure traces closely follow their non-reactive counterparts until the ignition event begins. The experimental ignition delays of these cases are under-predicted by the model. It is also seen in Fig. 5.6c for $T_C = 729$ K that the model predicts two-stage ignition, although two-stage ignition is not observed experimentally.

The current mechanism is also compared to shock tube ignition delays from the studies of Vasu et al. [83] and Vanderover and Oehlschlaeger [84]. Those studies considered the autoignition of stoichiometric mixtures of MCH with O_2/N_2 air. The comparison is shown in Fig. 5.7 for the near 50 atm data from those studies. Note that the experimental data shown are the raw data and are not scaled to a constant pressure, whereas the simulated ignition delays are at a constant initial pressure of 50 atm. It can be seen that the ignition delays are over-predicted over nearly the entire

(a) Mix #1   (b) Mix #2   (c) Mix #3

Figure 5.6: Comparison of selected simulated and experimental pressure traces at $P_C = 50$ bar. Red lines indicate that the pressure profile of the reactive simulation deviates from the non-reactive case prior to EOC. Solid lines: experiment; dashed lines: reactive simulation; dot-dot-dashed lines: non-reactive simulation.

temperature range of 795 K to 1160 K studied. Nevertheless, the predicted ignition delays are within approximately a factor of 1.5 of the experiments, indicating good agreement overall and a substantial improvement from the previous version of the model. Furthermore, the simulations shown here are of the CONV type and do not account for any facility dependent effects present in the experiments. Although the experimentalists noted in their studies [83, 84] that the effect of such considerations is minimal, including facility dependent effects will tend to make the simulations ignite sooner and improve the agreement, especially for cases with ignition delays longer than approximately 1000 μs.

As discussed in Sec. 5.3, one of the updates to the model was to increase the activation energy of ketohydroperoxide decomposition, from $E_a = 39 \, \text{kcal} \, \text{mol}^{-1}$ (163.2 kJ mol^{-1}) to 41.6 kcal mol^{-1} (174.1 kJ mol^{-1}). This update substantially improved the prediction of the low-temperature ignition delays, including the first stage and overall ignition delays. As mentioned by Curran et al. [162], "the high activation energy [of ketohydroperoxide decomposition] ensures an induction period during which the ketohydroperoxide concentration builds up." Furthermore, updating this activation energy does not affect the high-temperature ignition delays. A comparison of calculated ignition delays demonstrating the effect of this update is shown in Fig. 5.8.

C:/Users/bww09001/Documents/Github/dissertation/fi C:/Users/bww09001/Documents/Github/dissertation/fi
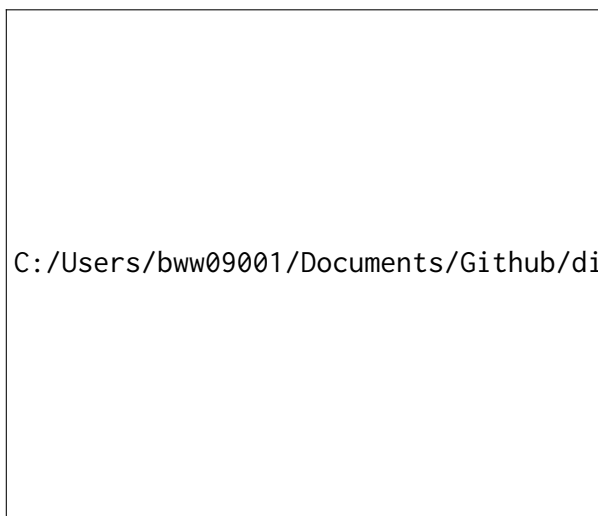
Figure 5.7: Comparison of the present model with the experiments from Vasu et al. [83] and Vanderover and Oehlschlaeger [84] near 50 atm and for stoichiometric mixtures in O_2/N_2 air.
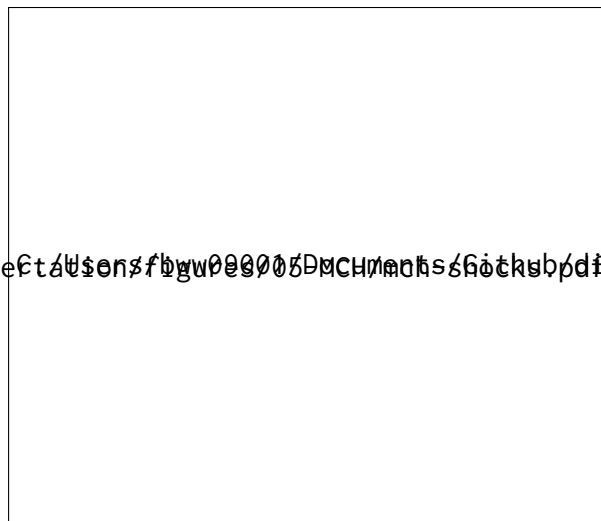
Figure 5.8: Comparison of mechanism performance with the activation energy of ketohydroperoxide decomposition set at $41.6\,\mathrm{kcal\,mol^{-1}}$ (blue) and $39.0\,\mathrm{kcal\,mol^{-1}}$ (red). Experimental ignition delays are shown in green symbols.

5.6 Discussion

5.6.1 Path Analysis

The relatively good agreement of the updated model with the experimental data suggests that a more detailed analysis of the mechanism is a worthwhile exercise and such analysis may point the way to further improvements to the mechanism. We begin with a reaction path analysis. The present reaction path analysis is conducted using a CONV (adiabatic, constant-volume) type simulation for three initial temperatures (700 K, 800 K, and 900 K), at 25.5 bar and for Mix #1 (the stoichiometric case). For the other mixture conditions and pressures considered in this work, the absolute percentages for each channel change slightly. However, the analysis of the reaction pathways is the same for all of the equivalence ratios and pressures considered in the experiments presented previously. The three temperatures considered in this analysis correspond to the low-temperature, peak of the NTC, and high-temperature portions of the ignition delay curve illustrated in Fig. 5.8; their results are shown in Fig. 5.9 with plain text, bold text, and italic text, respectively.

The path analysis presented in Fig. 5.9 is an integrated analysis where the rate of production (ROP) of each species by each reaction has been integrated with respect to time up to 20 % fuel consumption. The integrated ROPs from each reaction are normalized by the total production or destruction of that species up to 20 % fuel decomposition, such that reactions that produce a species are normalized by the total production of the species and reactions that consume a species are normalized by the total consumption of that species. The percentages in Fig. 5.9 therefore represent the percent of the given reactant that is consumed to form the given product by all reactions that can form a particular product. Species such as hydroperoxyalkyl radicals (QOOH), alkyl hydroperoxides (ROOH), and methylcyclohexenes (MCH-ene) are shown as lumped on the path diagram; however, these species are unlumped in the mechanism and presented as a lumped sum for simplicity in this diagram. Note that not all of the pathways present in the mechanism for each species are presented in Fig. 5.9, again for simplicity; the pathways that are shown in Fig. 5.9 typically account for more than 95 % of the consumption of each species.

The first step of fuel breakdown occurs by H-atom abstraction at these pressure and temperature conditions. None of the fuel is directly decomposed by unimolecular reactions. Each of the seven possible radicals are formed in comparable quantities; however, due to the symmetry of MCH, sites 2 and 3 are equivalent to sites 6 and 5, respectively, so mchr2 and mchr3 have close to double the production rate compared to the other radicals. It is interesting to note that the production of mchr2, mchr3, and mchr4 increase as the initial temperature increases and the production of mchr1 and cychexch2 decrease to compensate. However, the change is small, no more than 2 percentage points for each radical.

The most important second step is oxygen addition (i.e. formation of ROO) at all of the initial temperatures in this analysis. The importance of this reaction diminishes for each radical as the initial temperature increases due to the increasing importance of β-scission reactions. At 700 K, less than 0.05 % of each of the fuel radicals is consumed via β-scission. Between 800 K and 900 K, the percentages of mchr1, mchr2, mchr3, and mchr4 that are decomposed via β-scission increase by several thousand percent each; nevertheless, the absolute change is small and the consumption

96

C:/Users/bww09001/Documents/Github/dissertation/figures/05-MCH/mch-path.pdf

Figure 5.9: Path analysis of MCH combustion. Initial conditions are 25.5 bar and Mix #1 ($\phi = 1.0$) and 700 K (plain text), 800 K (bold text), 900 K (italic text). Note that not all possible reaction pathways are shown for each species.

of these radicals still occurs mostly by oxygen addition. The mchr1, mchr3, and mchr4 radicals undergo scission of the cyclohexyl ring, whereas mchr2 primarily undergoes scission at the methyl-cyclohexyl bond. This beta scission of mchr2 competes significantly with its consumption by O_2 at 900 K. Furthermore, the increasing importance of the ring opening reactions from 800 K to 900 K means that chain propagation pathways (instead of effective chain termination pathways forming methylcyclohexene and hydroperoxyl) are available, increasing the reactivity. Finally, even at the elevated initial temperature of 900 K, cychexch2 does not undergo significant ring opening. Instead, it will scission an H atom from site 1 or steal an oxygen atom from hydroperoxyl to form an alkoxy radical (RO) when it does not undergo oxygen addition (these pathways each only consume about 0.3 % of cychexch2 and hence are not shown in Fig. 5.9).

Returning to the low temperature pathways, there are four important classes of reactions that consume the ROO radicals in the current mechanism. These classes are: C1) internal H-atom transfer (isomerization) to form QOOH; C2) direct elimination of hydroperoxyl and methylcyclohexene; C3) H-abstraction by ROO from either the fuel or hydroperoxyl to form ROOH; and, C4) reactions among the ROO radicals. Class C4 consumes less than ≈ 5 % of each of the ROO radicals at 700 K and less than ≈ 0.1 % for the other temperatures and this class is therefore not shown on the path diagram in Fig. 5.9. Of the other three classes, C1 (formation of QOOH) is the predominant pathway in the low temperature ignition process. Nevertheless, the direct elimination of methylcyclohexene and hydroperoxyl and the formation of ROOH are important at low temperatures as well.

For all of the temperatures considered here, a majority of the ROOH is formed by reactions of ROO with hydroperoxyl to give ROOH and an oxygen molecule. At the initial temperature of 700 K, approximately 15 % of the fuel reacts to form ROOH, indicating its importance in low-temperature MCH combustion. The primary route of ROOH formation in this mechanism (H-abstraction from hydroperoxyl by ROO) has not been well studied at combustion relevant temperatures [163] and is therefore a good candidate for further investigation given its importance in the model for MCH combustion.

As the temperature increases, the formation of ROOH becomes substantially less important

while the direct HO_2 elimination reaction becomes more important. The increase in production of methylcyclohexene and hydroperoxyl plays a role in the NTC region of ignition delay because this is effectively a chain terminating channel until the temperature increases enough that the sequence $MCH+HO_2=R+H_2O_2$; $H_2O_2(+M)=2OH(+M)$ becomes important and drives the overall ignition.

Interestingly, for most of the ROO radicals, the change in the fraction of ROO consumed to form QOOH is non-monotonic as temperature increases. That is, for mch1oo, mch3oo, and mch4oo the production of QOOH increases in going from 700 K to 800 K, then decreases going from 800 K to 900 K due to the increasing importance of the HO_2 elimination channel (due to nuances in the various reaction paths, mch2oo and chxch2oo do not follow this trend). Furthermore, the branching ratios in the decomposition of the QOOH species change as the temperature is increased (not shown in Fig. 5.9). At the lowest temperature (700 K), the formation of hydroperoxyalkylperoxy radicals (OOQOOH) is favored, leading to low-temperature chain branching and the two-stage ignition phenomenon. However, at 800 K and 900 K, the QOOH tends to decompose into a heptenone and a hydroxyl radical, or one of two epoxide species. Due to the apparent importance of these species in the intermediate temperature decomposition of MCH, further investigation of their pathways is warranted.

5.6.2 Sensitivity Analysis

Our second type of analysis is a brute force, one-at-a-time sensitivity analysis. In this work, the sensitivity of the ignition delay to the reaction rates is considered. Due to the size of the mechanism, only the reactions of the fuel and the fuel radicals up to the OOQOOH species are considered. This approach is justified because many of the reactions of the C_0–C_4 base mechanism are important to the ignition process (e.g., $H_2O_2(+M)=2OH(+M)$), but we are more interested in the effect of updates to the fuel specific sub-mechanism. The sensitivity index is defined in Eq. (5.1),

$$S_i = \frac{\ln\left(\tau_{i,2}/\tau_{i,1}\right)}{\ln\left(k_{i,2}/k_{i,1}\right)} \tag{5.1}$$

where τ is the ignition delay time, either first stage or overall, k is the reaction rate, and subscript i indicates the reaction number. The numbered subscripts in Eq. (5.1) indicate the type of modification that has been made to the rate of reaction i when computing the ignition delay, as discussed in the following.

The reaction rates are modified by multiplying and dividing the pre-exponential constant by a factor f. Thus, the forward and reverse rates are simultaneously modified. Special care is taken to properly modify reaction rates with pressure dependence and explicit reverse parameters. Each rate is modified sequentially and the ignition delay is computed; the pre-exponential constant is reset to its nominal value before modifying the next reaction. Finally, the nominal ignition delay with no rate modification is computed. Thus, each set of reactor input conditions requires $2N + 1$ model evaluations, where N is the number of reactions considered in the sensitivity analysis and N may be less than or equal to the total number of reactions.

The $2N + 1$ model evaluations result in $4N + 2$ ignition delays if two-stage ignition is present and $2N + 1$ ignition delays otherwise. These ignition delays are used to compute the sensitivity indices according to Eq. (5.1). In the case of bidirectional sensitivity indices, the subscript 2 in Eq. (5.1) is associated with multiplication by f and the subscript 1 is associated with division by f, resulting in $2N$ sensitivity indices if two-stage ignition is present and N indices otherwise. In the case of unidirectional sensitivity indices, the subscript 2 is associated with either multiplication or division by f and the subscript 1 is associated with the nominal ignition delay, $\tau_{i,1} = \tau_1$. For unidirectional sensitivity indices, $4N$ indices are obtained if two-stage ignition is present and $2N$ indices are obtained otherwise.

In this work, the bidirectional sensitivity is used with $f = 10$. For all of the reactions considered here, multiplying and dividing a given rate had opposite effects on the ignition delay. Thus, if the ignition delay increased (relative to the nominal case) when the rate of a certain reaction was multiplied, the ignition delay decreased (relative to the nominal case) when the rate of the same reaction was divided and vice versa. Since $k_{i,2}$ is greater than $k_{i,1}$ by definition, the sensitivity index S_i will be positive if $\tau_{i,2} > \tau_{i,1}$ (i.e. increasing the rate increases the ignition delay) and

negative if $\tau_{i,2} < \tau_{i,1}$ (i.e. increasing the rate decreases the ignition delay). The sensitivity analysis is run at the same conditions of the path analysis: CONV simulation, initial temperatures of 700 K, 800 K, and 900 K, initial pressure of 25.5 bar, and Mix #1. As with the path analysis, similar results are obtained for other pressures and mixtures.

Figure 5.10 shows the sensitivity indices for the five reactions (among all the reactions considered in the present sensitivity analysis) to which the overall ignition delay is most sensitive for each temperature studied (700 K, 800 K, and 900 K). For the results at 700 K and 800 K, the bidirectional sensitivity of the first stage ignition delay to the same reactions is also shown, except for two reactions at 800 K for which the unidirectional sensitivity is plotted. The reasons for this will be discussed in due course. It should be noted that the sensitivity indices of the first stage ignition delay have a slightly different ranking than the indices of the overall ignition delay. Therefore, the rank of the first stage sensitivity index of the reactions shown is given in parentheses next to the bar. At 700 K, the sensitivity of the overall ignition delay is in red and the sensitivity of the first stage ignition delay is in blue; at 800 K, the sensitivity of the overall ignition delay is in grey and the sensitivity of the first stage ignition delay is in green. The most sensitive reaction affecting the first stage ignition delay at 800 K is found to be MCH+OH=mchr3+H2O, although it is not listed in Fig. 5.10. At 900 K, there is no first stage ignition, and thus no sensitivity of the first stage ignition delay.

Under the pressure/stoichiometry conditions of the present simulations, 800 K is approximately the highest initial temperature at which distinct two-stage ignition (i.e. two inflection points in the temperature or pressure trace) is found for MCH with the current mechanism. As such, several reactions affect the ignition strongly enough to eliminate the first inflection point. These reactions are given in Table 5.2 for either multiplication or division of the rate by the factor $f = 10$. The naming convention of the species listed in Table 5.2 can be found in Figs. 5.9 and 5.11 and Appendix A. Two reactions shown in Table 5.2 also appear in Fig. 5.10, namely ($R1$) mch2oo=mch2ene+ho2 and ($R2$) mch2qx+o2=mch2qxqj. For these reactions at 800 K, the unidirectional sensitivity index is shown in Fig. 5.10, where $\tau_{i,2}$ in Eq. (5.1) is found by division of the rate for $i = R1$ and by multiplication of the rate for $i = R2$.

101

Table 5.2: Reactions that eliminate the first inflection point for a nominal case with two-stage ignition.

Multiplication	Division
mch2oo = mch2ene + ho2	mch2qx + o2 = mch2qxqj
mch3oo = mch2ene + ho2	
mch3oo = mch3ene + ho2	
mch + oh = mchr1 + h2o	
mch + oh = mchr4 + h2o	
mch + oh = mchr3 + h2o	

The role of the ROO=methylcyclohexene+HO$_2$ reactions in the left column of Table 5.2 in eliminating the first stage of ignition is clear—this set of reactions diverts ROO radicals from entering the low-temperature chain branching pathway via QOOH that leads to the two-stage ignition. Similarly, in the right column, decreasing the rate of the reaction of oxygen with QOOH to form OOQOOH reduces the rate of chain branching that leads to two-stage ignition. Concerning the reactions of the fuel with OH in the left column of Table 5.2, increasing these rates increases the formation of fuel radicals that are less reactive at low temperature than the cychexch2 and mchr2 radicals. For example, the mchr2 radical adds to O$_2$ and forms a peroxy radical (mch2oo) that has a fast RO2 isomerization path to QOOH involving the abstraction of an H atom from the methyl group. This ROO isomerization is the path calculated and discussed in Section 4.1 of the work by Weber et al. [90]. QOOH subsequently adds to O$_2$ and leads to chain branching. The high reactivity of cychexch2 and mchr2 at low temperature is reflected by the high percentages at 800 K (>70 %) leading to QOOH from cychexch2oo and mch2oo in Fig. 5.9.

In general, Fig. 5.10 shows that the ignition delay is sensitive to different sets of reactions at the three temperatures, although there is some overlap. The overlapping reactions confound simple recommendations for rate improvements. For instance, at 700 K, increasing the overall ignition delay will improve agreement with the experimental data, but at 800 K, the agreement is already quite good. Therefore, adjusting any of the rates to improve the agreement with the overall ignition delay at 700 K will probably make the agreement worse at 800 K. However, the first stage ignition delays at 700 K and 800 K are both under-predicted; furthermore, two-stage ignition is predicted

C:/Users/bww09001/Documents/Github/dissertation/figures/05-MCH/mch-sens.pdf

C:/Users/bww09001/Documents/Gith
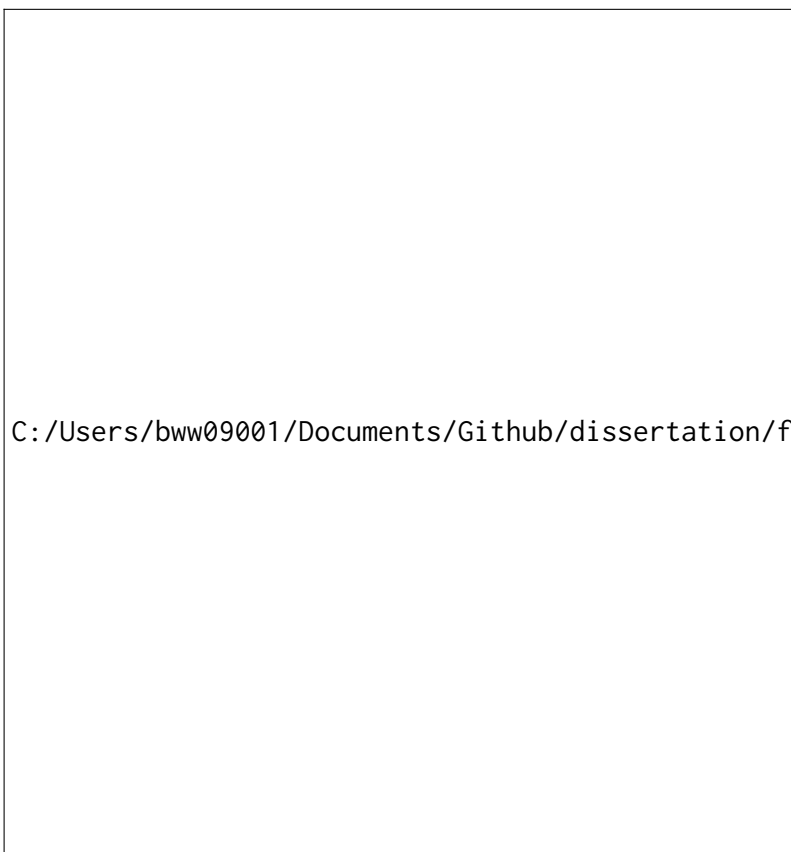
Figure 5.10: Sensitivity of the ignition delay to various reaction rates for Mix #1 (ϕ = 1.0), 25.5 bar and three temperatures (700 K, 800 K, and 900 K). At 700 K, the sensitivity of the overall ignition delay is in red and the sensitivity of the first stage ignition delay is in blue. At 800 K, the sensitivity of the overall ignition delay is in grey and the sensitivity of the first stage ignition delay is in green. At 900 K, the sensitivity of the overall ignition delay is in black. Numbers in parentheses represent the ranking of the first stage sensitivity indices.
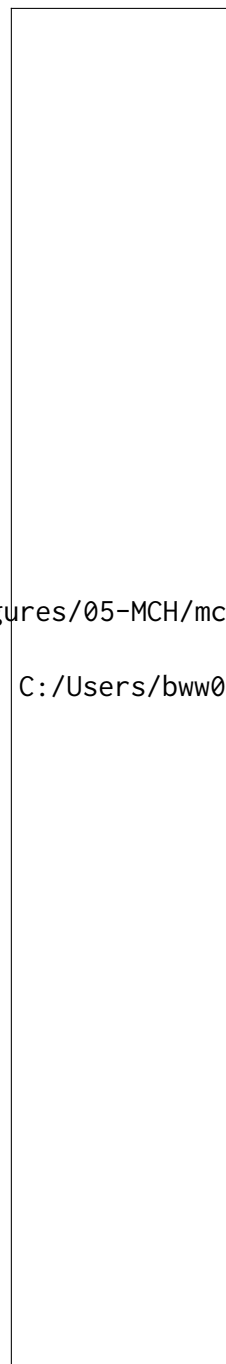
Figure 5.11: Species mentioned in Fig. 5.10 or Table 5.2 and not included in Fig. 5.9.

at temperatures for which the experimental ignition is single stage. It should therefore be possible to adjust several rate constants simultaneously to improve agreement with the first stage ignition delay and not deteriorate agreement with the overall ignition delay. To accomplish the simultaneous improvement of agreement of first stage and overall ignition delays, the rate constants of reactions that control the second stage ignition delay may also need to be adjusted (where second stage ignition delay is the difference between the overall ignition delay and the first stage ignition delay).

Interestingly, the formation and destruction reactions of ROOH species do not appear in Fig. 5.10, despite their importance in the destruction of ROO radicals, particularly at 700 K (see Fig. 5.9). This may be due to the fact that formation of ROOH by reaction with HO_2 followed by consumption of ROOH is a chain propagation path through the reactions $ROO+HO_2=ROOH+O_2$; $ROOH=RO+OH$. In this sequence two radicals are formed (RO, OH) and two radicals are consumed (ROO, HO_2). Thus, the formation of ROOH by reaction with HO_2 and its subsequent destruction has a somewhat neutral effect on the radical pool.

At 900 K, the overall ignition delay is particularly sensitive to reactions that form hydrogen peroxide, which decomposes to two hydroxyl radicals as the temperature increases during the induction period. Therefore, increasing the rate of formation of hydrogen peroxide will increase the formation of hydroxyl radical and decrease the overall ignition delay. At 900 K, the overall ignition delay is over-predicted, so to improve the results, the overall ignition delay should be reduced (i.e. increasing the rates of reactions with negative sensitivity will improve the comparison). In addition, many of the reactions that are important at 900 K are not important at 700 K and 800 K, implying that changes made to the rates to improve the high-temperature agreement will not significantly change the agreement at lower temperature. In particular, the MCH+HO_2 rate constants have not been measured or calculated to our knowledge and are based on acyclic alkane rate constants [164]. They have uncertainties of at least a factor of 2 and as much as a factor of 10 based on the work of Aguilera-Iparraguirre et al. [164]. Increasing these rate constants would improve the agreement with the experimental ignition data at 900 K in the RCM and shock tube. Experimental measurements and theoretical calculations are needed for the fuel+HO_2 reaction class to reduce this uncertainty in

the rate constants.

5.7 Conclusions

In this study, new experimental data are collected for methylcyclohexane autoignition in a heated RCM. Following the work of Mittal and Sung [89], three mixtures of MCH/O$_2$/ N$_2$/Ar at equivalence ratios of $\phi = 0.5$, 1.0, and 1.5 are used and the ignition delays are measured at compressed pressure of 50 bar, for compressed temperatures in the range of 690 K to 900 K. Two-stage ignition phenomena are reported for the stoichiometric and rich mixtures. However, substantial reactivity during the compression stroke limited the temperature range over which ignition delays could be reported, especially for the lean case. For these mixtures where the fuel concentration was kept constant, the order of reactivity, in terms of inverse overall ignition delay, is $\phi = 0.5 > \phi = 1.0 > \phi = 1.5$.

In addition, an existing model for the combustion of MCH developed by Pitz et al. [14] is updated with new reaction rates and pathways. The new model shows good agreement with the overall ignition delays measured in this study, as well as the overall ignition delays measured in the studies of Vasu et al. [83], Vanderover and Oehlschlaeger [84], and Mittal and Sung [89]. However, the first stage ignition delays are uniformly under-predicted and in several cases, first stage ignition is predicted by the model where experimental ignition response shows no two-stage character. To help understand the fuel decomposition pathways and the reactions controlling the ignition, further analysis of the present mechanism is conducted.

First, reaction path analysis is conducted for low-, intermediate-, and high-temperature ignition considered in this study. The results show that MCH primarily decomposes by H-abstraction reactions involving OH and HO$_2$ radicals, followed by oxygen addition reactions. At low temperatures, the oxygen addition is followed by isomerization to QOOH species and second oxygen addition, leading to the low-temperature chain branching characteristic of two-stage ignition. At intermediate temperatures, the elimination of methylcyclohexene and HO$_2$ becomes competitive with the isomerization reaction, leading to the NTC region of the overall ignition delay. Finally, at high

temperatures, MCH+HO$_2$ reactions form H$_2$O$_2$ and end the NTC region.

Second, a brute force sensitivity analysis is conducted to identify the reactions of the fuel and primary fuel radicals that control the ignition process. The overall and first stage ignition events at low and intermediate temperatures are primarily controlled by the initial reactions to form fuel radicals, especially H-abstraction by OH. At high temperatures, the controlling reactions are still the fuel radical formation reactions, but now the ignition process is controlled by H-abstraction by hydroperoxyl instead of hydroxyl. Combined, these analyses suggest that further investigation of several of the low-temperature fuel decomposition pathways is required and more accurate rate constants for fuel+HO$_2$ reactions are needed.

Chapter 6

Conclusions and Future Directions

The detailed conclusions relevant to each of the experimental works considered in this study are presented in their respective chapters. The following gives a general summary of the previous works and provides recommendations for future work, including descriptions of ongoing investigations using a new sampling system.

6.1 Conclusions

The studies reported in this work are the first experiments exploring the low-to-intermediate temperature autoignition of the butanol isomers. These data provide a unique look into the behavior of these fuels under engine-relevant conditions. For the stoichiometric condition at two pressures, *n*-butanol was the most reactive of the isomers. However, the order of the reactivity of the other isomers depended on the prevailing pressure conditions during the induction period. *t*-butanol became the second most reactive isomer at the higher pressure condition and showed unique behavior during the induction period. Analysis of a detailed kinetic model for combustion of the butanol isomers elucidated the controlling chemistry during the autoignition of the four isomers, and indicated that the different behavior of *t*-butanol is due to a unique set of controlling reactions for *t*-butanol.

6.2 Fast Sampling System

The fast sampling system (FSS) used in this work is a commercial system supplied by SME-Tec Gmbh. from Germany. The FSS is composed of two parts, the gas sampling valve (GSV) and the Controller. A schematic of the GSV is shown in **??**. Gases are admitted from the reaction chamber into the heated carrying tubes through the poppet-style valve on the left of the GSV. The sampled gases are then conducted through the GSV outlet into the 15 mL sampling bottle.

A schematic of the GSV assembly is shown in **??**. The GSV is mounted to the RCM by a custom-made end plug. The reaction chamber is sealed by an O-ring on the small- and large-diameter portions of the GSV. The depth that the GSV is inserted into the reaction chamber is adjustable by adding or removing shims in the end plug assembly. The insertion depth is chosen so that the tip of the GSV is outside the boundary layer on the end wall.

The portion of the GSV protruding into the reaction chamber has minimal effect on the homogeneity of the reaction chamber. Moreover, the removal of samples has minimal effect on the measured ignition delay. This has been verified experimentally by measuring the ignition delay with and without the GSV present, and with and without sampling occurring. In both cases, the difference in ignition delay was statistically insignificant for $\alpha = 0.05$.

The close-open-close (COC) cycle of the GSV is controlled by a mass-spring system. The poppet face is connected to a rod running the length of the GSV and connected to the mass at the rear of the valve. To open the poppet, the mass is accelerated forward by passing current through the coil around the mass. The rod is also connected to a spring that is used to restore the poppet to its original position after being extended.

The GSV has an adjustable COC time, by adjusting the distance the plate is allowed to move. Furthermore, the GSV has the ability to measure the displacement of the mass, allowing the direct measurement of the COC time and the absolute time of opening.

The GSV controller is triggered by a 5 V signal from the cDAQ. The timing of the trigger signal is controlled by the LabView VI. The pressure signal from the reaction chamber is read from

the cDAQ in 1 ms chunks in a loop. On each loop iteration, the maximum pressure is checked against a desired trigger pressure; when the reaction chamber pressure exceeds the trigger pressure, the cDAQ sends the trigger to the GSV controller. The GSV controller has an adjustable delay (4.5 ms to 70 ms) that is used to control the timing of the opening of the GSV during the induction period. The absolute opening time of the GSV is thus dependent on three parameters:

1. The cable delays from the PC to the cDAQ; from the cDAQ to the GSV controller; and from the GSV controller to the GSV itself

2. The processing time of the LabView VI

3. The delay set in the GSV controller.

However, since the absolute opening time of the GSV can be measured by the signal sent from the GSV to the controller (and thence to the cDAQ), the uncertainty in the opening time is actually quite small, and is related to the cable delay in sending the COC signal from the GSV to the cDAQ and the precision of the A/D conversion in the cDAQ. The uncertainty of the absolute opening time is thus estimated as $\pm 1\,\mu s$.

Verify this number

Furthermore, the correspondence of the COC signal from the valve with the physical valve movements has been experimentally verified by high speed video. Frames from these videos are shown in **??**. The frames show that the opening and closing times of the valve face correspond closely with repeatable points in the peak of the voltage.

Missing figure

GSV Video

6.2.1 Experimental Procedure

Prior to an experiment, the GSV and sampling bottle are vacuumed to less than 1 torr. The reaction chamber is vacuumed and filled in the same procedure as described previously, and the compression is triggered. For a given trigger pressure and controller delay, the GSV opens at some time after the EOC and removes a gas sample from the reaction chamber. The sample is diluted by high purity helium. Then the sample bottle is disconnected from the GSV and transported to the Gas Chromatograph/Mass Spectrometer, where the sample undergoes analysis.

References

[1]   Sims, R., Schock, R., Adegbululgbe, A., Fenhann, J., Konstantinaviciute, I., Moomaw, W., et al. In: *Clim. Chang. 2007 Mitig.* Ed. by Metz, B., Davidson, O., Bosch, P., Dave, R., and Meyer, L. New York, NY, 2007. URL: http://www.ipcc.ch/pdf/assessment-report/ar4/wg3/ar4-wg3-chapter4.pdf.

[2]   US Energy Information Administration. *International Energy Outlook 2013*. Tech. rep. July 2013. URL: http://www.eia.gov/forecasts/ieo/pdf/0484(2013).pdf.

[3]   US Energy Information Administration. *EIA Monthly Energy Review*. Tech. rep. May 2013. URL: http://www.eia.gov/totalenergy/data/monthly/archive/00351305.pdf.

[4]   Avakian, M. D., Dellinger, B., Fiedler, H., Gullet, B., Koshland, C., Marklund, S., et al. *Environ. Health Perspect.*, vol. 110, no. 11 (Nov. 2002), pp. 1155–1162. URL: http://www.pubmedcentral.nih.gov/articlerender.fcgi?artid=1241073%5C&tool=pmcentrez%5C&rendertype=abstract.

[5]   Owen, N. A., Inderwildi, O. R., and King, D. A. *Energy Policy*, vol. 38, no. 8 (Aug. 2010), pp. 4743–4749. DOI: 10.1016/j.enpol.2010.02.026.

[6]   Westbrook, C. K. and Dryer, F. L. *Prog. Energy Combust. Sci.*, vol. 10, no. 1 (Jan. 1984), pp. 1–57. DOI: 10.1016/0360-1285(84)90118-7.

[7]   Smith, G. P., Golden, D. M., Frenklach, M., Moriarty, N. W., Eiteneer, B., Goldenberg, M., et al. *GRI-Mech 3.0*. URL: http://www.me.berkeley.edu/gri-mech/ (visited on 02/19/2010).

[8] Wang, H., You, X., Joshi, A. V., Davis, S. G., Laskin, A., Egolfopoulos, F. N., et al. *USC-Mech Version II. High-Temperature Combustion Reaction Model of H2/CO/C1-C4 Compounds*. 2007. URL: http://ignis.usc.edu/Mechanisms/USC-Mech%20II/USC%5C_Mech%20II.htm (visited on 04/08/2014).

[9] Metcalfe, W. K., Burke, S. M., Ahmed, S. S., and Curran, H. J. *Int. J. Chem. Kinet.*, vol. 45, no. 10 (Oct. 2013), pp. 638–675. DOI: 10.1002/kin.20802.

[10] Kohse-Höinghaus, K., Oßwald, P., Cool, T. A., Kasper, T., Hansen, N., Qi, F., et al. *Angew. Chemie*, vol. 49, no. 21 (May 2010), pp. 3572–3597. DOI: 10.1002/anie.200905335.

[11] Pitz, W. J. and Mueller, C. J. *Prog. Energy Combust. Sci.*, vol. 37, no. 3 (June 2011), pp. 330–350. DOI: 10.1016/j.pecs.2010.06.004.

[12] Dooley, S., Won, S. H., Heyne, J. S., Farouk, T. I., Ju, Y., Dryer, F. L., et al. *Combust. Flame*, vol. 159, no. 4 (Apr. 2012), pp. 1444–1466. DOI: 10.1016/j.combustflame.2011.11.002.

[13] Anand, K., Ra, Y., Reitz, R. D., and Bunting, B. *Energy Fuel*, vol. 25, no. 4 (Apr. 2011), pp. 1474–1484. DOI: 10.1021/ef101719a.

[14] Pitz, W. J., Naik, C. V., Mhaoldúin, T. N., Westbrook, C. K., Curran, H. J., Orme, J., et al. *Proc. Combust. Inst.*, vol. 31, no. 1 (Jan. 2007), pp. 267–275. DOI: 10.1016/j.proci.2006.08.041.

[15] Briker, Y., Ring, Z., Iacchelli, A., McLean, N., Rahimi, P. M., Fairbridge, C., et al. *Energy Fuel*, vol. 15, no. 1 (Jan. 2001), pp. 23–37. DOI: 10.1021/ef000106f.

[16] Farrell, J. T., Cernansky, N. P., Dryer, F. L., Friend, D. G., Hergart, C. A., Law, C. K., et al. *Development of an Experimental Database and Kinetic Models for Surrogate Diesel Fuels*. Tech. rep. SAE International, 2007. DOI: 10.4271/2007-01-0201.

[17]   Edwards, T., Colket, M. B., Cernansky, N., Dryer, F. L., Egolfopoulos, F. N., Friend, D., et al. "Development of an Experimental Database and Kinetic Models for Surrogate Jet Fuels". In: *45th AIAA Aerosp. Sci. Meet. Exhib.* American Institute of Aeronautics and Astronautics. Reno, NV, Jan. 2007. DOI: 10.2514/6.2007-770.

[18]   Bieleveld, T., Frassoldati, A., Cuoci, A., Faravelli, T., Ranzi, E., Niemann, U., et al. *Proc. Combust. Inst.*, vol. 32, no. 1 (Jan. 2009), pp. 493–500. DOI: 10.1016/j.proci.2008.06.214.

[19]   Naik, C. V., Pitz, W. J., Westbrook, C. K., Sjöberg, M., Dec, J. E., Orme, J., et al. *Detailed Chemical Kinetic Modeling of Surrogate Fuels for Gasoline and Application to an HCCI Engine*. Tech. rep. Warrendale, PA: SAE International, 2005. DOI: 10.4271/2005-01-3741.

[20]   Peralta-Yahya, P. P., Zhang, F., Cardayre, S. B. del, and Keasling, J. D. *Nature*, vol. 488, no. 7411 (Aug. 2012), pp. 320–328. DOI: 10.1038/nature11478.

[21]   Afeefy, H., Liebman, J., and Stein, S. In: *NIST Chem. WebBook, NIST Stand. Ref. Database Number 69*. Ed. by Linstrom, P. and Mallard, W. Gaithersburg MD, 2014. URL: http://webbook.nist.gov.

[22]   Davis, S. C., Diegel, S. W., and Boundy, R. G. *Transportation Energy Data Book*. 32nd ed. Oak Ridge, Tennessee, 2013. URL: http://cta.ornl.gov/data/index.shtml.

[23]   Niven, R. *Renew. Sustain. Energy Rev.*, vol. 9, no. 6 (Dec. 2005), pp. 535–555. DOI: 10.1016/j.rser.2004.06.003.

[24]   Somma, D., Lobkowicz, H., and Deason, J. P. *Clean Technol. Environ. Policy*, vol. 12, no. 4 (June 2009), pp. 373–380. DOI: 10.1007/s10098-009-0234-3.

[25]   Harvey, B. G. and Meylemans, H. A. *J. Chem. Technol. Biotechnol.*, vol. 86, no. 1 (Jan. 2011), pp. 2–9. DOI: 10.1002/jctb.2540.

[26]   Nigam, P. S. and Singh, A. *Prog. Energy Combust. Sci.*, vol. 37, no. 1 (Feb. 2011), pp. 52–68. DOI: 10.1016/j.pecs.2010.01.003.

[27] Smith, K. M., Cho, K.-M., and Liao, J. C. *Appl. Microbiol. Biotechnol.*, vol. 87, no. 3 (July 2010), pp. 1045–1055. DOI: 10.1007/s00253-010-2522-6.

[28] Dernotte, J., Mounaim-Rousselle, C., Halter, F., and Seers, P. *Oil Gas Sci. Technol.*, vol. 65, no. 2 (Nov. 2009), pp. 345–351. DOI: 10.2516/ogst/2009034.

[29] Szwaja, S. and Naber, J. *Fuel*, vol. 89, no. 7 (July 2010), pp. 1573–1582. DOI: 10.1016/j.fuel.2009.08.043.

[30] Kim, D. H., Lee, J. M., Park, E. H., Song, J. H., and Park, S. I. *Int. J. Automot. Technol.*, vol. 12, no. 3 (May 2011), pp. 409–416. DOI: 10.1007/s12239-011-0048-2.

[31] Veloo, P. S. and Egolfopoulos, F. N. *Proc. Combust. Inst.*, vol. 33, no. 1 (Sept. 2011), pp. 987–993. DOI: 10.1016/j.proci.2010.06.163.

[32] Dagaut, P. and Togbé, C. *Energy Fuel*, vol. 23, no. 7 (July 2009), pp. 3527–3535. DOI: 10.1021/ef900261f.

[33] Hansen, N., Harper, M. R., and Green, W. H. *Phys. Chem. Chem. Phys.*, vol. 13, no. 45 (Dec. 2011), pp. 20262–20274. DOI: 10.1039/c1cp21663e.

[34] Hansen, N., Merchant, S. S., Harper, M. R., and Green, W. H. *Combust. Flame*, vol. 160, no. 11 (Nov. 2013), pp. 2343–2351. DOI: 10.1016/j.combustflame.2013.05.013.

[35] Grana, R., Frassoldati, A., Faravelli, T., Niemann, U., Ranzi, E., Seiser, R., et al. *Combust. Flame*, vol. 157, no. 11 (June 2010), pp. 2137–2154. DOI: 10.1016/j.combustflame.2010.05.009.

[36] Van Geem, K. M., Pyl, S. P., Marin, G. B., Harper, M. R., and Green, W. H. *Ind. Eng. Chem. Res.*, vol. 49, no. 21 (Nov. 2010), pp. 10399–10420. DOI: 10.1021/ie1005349.

[37] Cai, J., Zhang, L., Zhang, F., Wang, Z., Cheng, Z., Yuan, W., et al. *Energy Fuel*, vol. 26, no. 9 (Sept. 2012), pp. 5550–5568. DOI: 10.1021/ef3011965.

[38] Cai, J., Yuan, W., Ye, L., Cheng, Z., Wang, Y., Zhang, L., et al. *Combust. Flame*, vol. 160, no. 10 (Oct. 2013), pp. 1939–1957. DOI: 10.1016/j.combustflame.2013.04.010.

[39] Lefkowitz, J. K., Heyne, J. S., Won, S. H., Dooley, S., Kim, H. H., Haas, F. M., et al. *Combust. Flame*, vol. 159, no. 3 (Mar. 2012), pp. 968–978. DOI: 10.1016/j.combustflame.2011.10.004.

[40] Heyne, J. S., Dooley, S., and Dryer, F. L. *J. Phys. Chem. A*, vol. 117, no. 37 (Oct. 2013), pp. 8997–9004. DOI: 10.1021/jp404143f.

[41] Stranic, I., Pang, G. A., Hanson, R. K., Golden, D. M., and Bowman, C. T. *J. Phys. Chem. A*, vol. 117, no. 23 (June 2013), pp. 4777–4784. DOI: 10.1021/jp402176e.

[42] Pang, G. A., Hanson, R. K., Golden, D. M., and Bowman, C. T. *J. Phys. Chem. A*, vol. 116, no. 19 (May 2012), pp. 4720–4725. DOI: 10.1021/jp302719j.

[43] Pang, G. A., Hanson, R. K., Golden, D. M., and Bowman, C. T. *J. Phys. Chem. A*, vol. 116, no. 10 (Mar. 2012), pp. 2475–2483. DOI: 10.1021/jp211885p.

[44] Seal, P., Oyedepo, G. A., and Truhlar, D. G. *J. Phys. Chem. A*, vol. 117, no. 2 (Jan. 2013), pp. 275–282. DOI: 10.1021/jp310910f.

[45] Pang, G. A., Hanson, R. K., Golden, D. M., and Bowman, C. T. *J. Phys. Chem. A*, vol. 116, no. 39 (Oct. 2012), pp. 9607–9613. DOI: 10.1021/jp306977e.

[46] El-Nahas, A. M., Mangood, A. H., El-Shereafy, E.-S. E., and El-Meleigy, A. B. *Fuel* (Nov. 2012), pp. 29–33. DOI: 10.1016/j.fuel.2012.10.054.

[47] Zhou, C.-W., Simmie, J. M., and Curran, H. J. *Combust. Flame*, vol. 158, no. 4 (Apr. 2011), pp. 726–731. DOI: 10.1016/j.combustflame.2010.11.002.

[48] Moc, J. and Simmie, J. M. *J. Phys. Chem. A*, vol. 114, no. 17 (May 2010), pp. 5558–5564. DOI: 10.1021/jp1009065.

[49] Vasu, S. S., Davidson, D. F., Hanson, R. K., and Golden, D. M. *Chem. Phys. Lett.*, vol. 497, no. 1-3 (Aug. 2010), pp. 26–29. DOI: 10.1016/j.cplett.2010.08.001.

[50] Zhou, C.-W., Simmie, J. M., and Curran, H. J. *Int. J. Chem. Kinet.*, vol. 44, no. 3 (Jan. 2012), pp. 155–164. DOI: 10.1002/kin.20708.

[51] Alecu, I. M., Zheng, J., Papajak, E., Yu, T., and Truhlar, D. G. *J. Phys. Chem. A*, vol. 116, no. 50 (Dec. 2012), pp. 12206–12213. DOI: 10.1021/jp308460y.

[52] Black, G. and Simmie, J. M. *J. Comput. Chem.*, vol. 31, no. 6 (Apr. 2010), pp. 1236–1248. DOI: 10.1002/jcc.21410.

[53] Katsikadakos, D., Zhou, C.-W., Simmie, J. M., Curran, H. J., Hunt, P., Hardalupas, Y., et al. *Proc. Combust. Inst.*, vol. 34, no. 1 (Jan. 2013), pp. 483–491. DOI: 10.1016/j.proci.2012.06.015.

[54] Katsikadakos, D., Hardalupas, Y., Taylor, A., and Hunt, P. *Phys. Chem. Chem. Phys.*, vol. 14, no. 27 (July 2012), pp. 9615–9629. DOI: 10.1039/c2cp24074b.

[55] Moss, J. T., Berkowitz, A. M., Oehlschlaeger, M. A., Biet, J., Warth, V., Glaude, P.-A., et al. *J. Phys. Chem. A*, vol. 112, no. 43 (Oct. 2008), pp. 10843–10855. DOI: 10.1021/jp806464p.

[56] Black, G., Curran, H. J., Pichon, S., Simmie, J. M., and Zhukov, V. P. *Combust. Flame*, vol. 157, no. 2 (Feb. 2010), pp. 363–373. DOI: 10.1016/j.combustflame.2009.07.007.

[57] Noorani, K. E., Akih-Kumgeh, B., and Bergthorson, J. M. *Energy Fuel*, vol. 24, no. 11 (Nov. 2010), pp. 5834–5843. DOI: 10.1021/ef1009692.

[58] Zhang, J., Wei, L., Man, X., Jiang, X., Zhang, Y., Hu, E., et al. *Energy Fuel*, vol. 26, no. 6 (June 2012), pp. 3368–3380. DOI: 10.1021/ef3005042.

[59] Stranic, I., Chase, D. P., Harmon, J. T., Yang, S., Davidson, D. F., and Hanson, R. K. *Combust. Flame*, vol. 159, no. 2 (Feb. 2012), pp. 516–527. DOI: 10.1016/j.combustflame.2011.08.014.

[60] Yasunaga, K., Mikajiri, T., Sarathy, S. M., Koike, T., Gillespie, F., Nagy, T., et al. *Combust. Flame*, vol. 159, no. 6 (June 2012), pp. 2009–2027. DOI: 10.1016/j.combustflame.2012.02.008.

[61] Heufer, K. A., Fernandes, R. X., Olivier, H., Beeckmann, J., Röhl, O., and Peters, N. *Proc. Combust. Inst.*, vol. 33, no. 1 (Aug. 2011), pp. 359–366. DOI: `10.1016/j.proci.2010.06.052`.

[62] Vranckx, S., Heufer, K. A., Lee, C., Olivier, H., Schill, L., Kopp, W., et al. *Combust. Flame*, vol. 158, no. 8 (Aug. 2011), pp. 1444–1455. DOI: `10.1016/j.combustflame.2010.12.028`.

[63] Zhu, Y., Davidson, D. F., and Hanson, R. K. *Combust. Flame*, vol. 161, no. 3 (Mar. 2014), pp. 634–643. DOI: `10.1016/j.combustflame.2013.06.028`.

[64] Weber, B. W., Kumar, K., Zhang, Y., and Sung, C.-J. *Combust. Flame*, vol. 158, no. 5 (Mar. 2011), pp. 809–819. DOI: `10.1016/j.combustflame.2011.02.005`.

[65] Weber, B. W. and Sung, C.-J. *Energy Fuel*, vol. 27, no. 3 (Mar. 2013), pp. 1688–1698. DOI: `10.1021/ef302195c`.

[66] Weber, B. W., Merchant, S. S., Sung, C.-J., and Green, W. H. "An Autoignition Study of iso-Butanol: Experiments and Modeling". In: *8th US Natl. Tech. Meet. Combust. Inst.* University of Utah. Park City, UT, May 2013, Paper 3A01.

[67] Karwat, D. M. A., Wagnon, S. W., Teini, P. D., and Wooldridge, M. S. *J. Phys. Chem. A*, vol. 115, no. 19 (May 2011), pp. 4909–4921. DOI: `10.1021/jp200905n`.

[68] Cook, R. D., Davidson, D. F., and Hanson, R. K. *Int. J. Chem. Kinet.*, vol. 44, no. 5 (May 2012), pp. 303–311. DOI: `10.1002/kin.20713`.

[69] Stranic, I., Pyun, S. H., Davidson, D. F., and Hanson, R. K. *Combust. Flame*, vol. 159, no. 11 (Nov. 2012), pp. 3242–3250. DOI: `10.1016/j.combustflame.2012.06.005`.

[70] Stranic, I., Pyun, S. H., Davidson, D. F., and Hanson, R. K. *Combust. Flame*, vol. 160, no. 6 (June 2013), pp. 1012–1019. DOI: `10.1016/j.combustflame.2013.01.015`.

[71] Rosado-Reyes, C. M. and Tsang, W. *J. Phys. Chem. A*, vol. 116, no. 40 (Oct. 2012), pp. 9825–9831. DOI: `10.1021/jp305120h`.

[72] Rosado-Reyes, C. M. and Tsang, W. *J. Phys. Chem. A*, vol. 116, no. 39 (Oct. 2012), pp. 9599–606. DOI: 10.1021/jp306975s.

[73] Dayma, G., Togbé, C., and Dagaut, P. *Energy Fuel*, vol. 25, no. 11 (Nov. 2011), pp. 4986–4998. DOI: 10.1021/ef2012112.

[74] Togbé, C., Halter, F., Foucher, F., Mounaim-Rousselle, C., and Dagaut, P. *Proc. Combust. Inst.*, vol. 33, no. 1 (2011), pp. 367–374. DOI: 10.1016/j.proci.2010.05.003.

[75] Sarathy, S. M., Park, S., Weber, B. W., Wang, W., Veloo, P. S., Davis, A. C., et al. *Combust. Flame*, vol. 160, no. 12 (Dec. 2013), pp. 2712–2728. DOI: 10.1016/j.combustflame.2013.06.022.

[76] Welz, O., Zádor, J., Savee, J. D., Ng, M. Y., Meloni, G., Fernandes, R. X., et al. *Phys. Chem. Chem. Phys.*, vol. 14, no. 9 (Mar. 2012), pp. 3112–3127. DOI: 10.1039/c2cp23248k.

[77] Tsujimura, T., Pitz, W. J., Gillespie, F., Curran, H. J., Weber, B. W., Zhang, Y., et al. *Energy Fuel*, vol. 26, no. 8 (Aug. 2012), pp. 4871–4886. DOI: 10.1021/ef300879k.

[78] Tang, C., Wei, L., Man, X., Zhang, J., Huang, Z., and Law, C. K. *Combust. Flame*, vol. 160, no. 3 (Mar. 2013), pp. 520–529. DOI: 10.1016/j.combustflame.2012.11.018.

[79] Tsujimura, T., Pitz, W. J., Yang, Y., and Dec, J. E. *Int. J. Fuels Lubr.*, vol. 4, no. 2 (Dec. 2011), pp. 257–270. DOI: 10.4271/2011-24-0023.

[80] Yacoub, Y., Bata, R. M., and Gautam, M. *Proc. Inst. Mech. Eng. Part A J. Power Energy*, vol. 212, no. 5 (Jan. 1998), pp. 363–379. DOI: 10.1243/0957650981536934.

[81] Yang, Y., Dec, J. E., Dronniou, N., and Simmons, B. A. *Int. J. Fuels Lubr.*, vol. 3, no. 2 (2010), pp. 725–741. DOI: 10.4271/2010-01-2164.

[82] Rotavera, B. and Petersen, E. L. *Proc. Combust. Inst.*, vol. 34, no. 1 (Jan. 2013), pp. 435–442. DOI: 10.1016/j.proci.2012.06.042.

[83] Vasu, S. S., Davidson, D. F., and Hanson, R. K. *Combust. Flame*, vol. 156, no. 4 (Apr. 2009), pp. 736–749. DOI: 10.1016/j.combustflame.2008.09.006.

[84] Vanderover, J. and Oehlschlaeger, M. A. *Int. J. Chem. Kinet.*, vol. 41, no. 2 (Feb. 2009), pp. 82–91. DOI: 10.1002/kin.20370.

[85] Hawthorn, R. D. and Nixon, A. C. *AIAA J.*, vol. 4, no. 3 (Mar. 1966), pp. 513–520. DOI: 10.2514/3.3466.

[86] Orme, J., Curran, H. J., and Simmie, J. M. *J. Phys. Chem. A*, vol. 110, no. 1 (Jan. 2006), pp. 114–131. DOI: 10.1021/jp0543678.

[87] Hong, Z., Lam, K.-Y., Davidson, D. F., and Hanson, R. K. *Combust. Flame*, vol. 158, no. 8 (Aug. 2011), pp. 1456–1468. DOI: 10.1016/j.combustflame.2010.12.019.

[88] Tanaka, S., Ayala, F., Keck, J. C., and Heywood, J. B. *Combust. Flame*, vol. 132, no. 1-2 (Jan. 2003), pp. 219–239. DOI: 10.1016/S0010-2180(02)00457-1.

[89] Mittal, G. and Sung, C.-J. *Combust. Flame*, vol. 156, no. 9 (Sept. 2009), pp. 1852–1855. DOI: 10.1016/j.combustflame.2009.05.009.

[90] Weber, B. W., Pitz, W. J., Mehl, M., Silke, E. J., Davis, A. C., and Sung, C.-J. *Combust. Flame* (Feb. 2014), In Press. DOI: 10.1016/j.combustflame.2014.01.018.

[91] Das, A. K., Sung, C.-J., Zhang, Y., and Mittal, G. *Int. J. Hydrogen Energy*, vol. 37, no. 8 (Apr. 2012), pp. 6901–6911. DOI: 10.1016/j.ijhydene.2012.01.111.

[92] Uddi, M., Das, A. K., and Sung, C.-J. *Appl. Opt.*, vol. 51, no. 22 (Aug. 2012), pp. 5464–5476. URL: http://www.ncbi.nlm.nih.gov/pubmed/22859037.

[93] Withrow, L., Lovell, W. G., and Boyd, T. A. *Ind. Eng. Chem.*, vol. 22, no. 9 (Sept. 1930), pp. 945–951. DOI: 10.1021/ie50249a013.

[94] Brooks, D. B. "Chemistry of Internal-Combustion Engines". M.S. Thesis. The Ohio State University, 1922. URL: http://library.ohio-state.edu/record=b2828123~S7.

[95] Callendar, H. L. *Dopes and Detonation*. Tech. rep. London, UK: Aeronautical Research Council, 1926. URL: http://naca.central.cranfield.ac.uk/reports/arc/ar/.

[96]   Egerton, A. and Gates, S. F. *Report on anti-knock investigations*. Tech. rep. London, UK: Aeronautical Research Council, 1926. URL: http://naca.central.cranfield.ac.uk/reports/arc/ar/.

[97]   Lovell, W. G., Coleman, J. D., and Boyd, T. A. *Ind. Eng. Chem.*, vol. 19, no. 3 (Mar. 1927), pp. 372–376. DOI: 10.1021/ie50207a014.

[98]   Ricardo, H. R. and Thornycroft, O. "Petrol Engines and Their Fuels". In: *Trans. Fuel Conf. World Power Conf. Vol III*. The Institution of Petroleum Technologists. London, UK, 1928, pp. 662–684. URL: https://archive.org/details/transactionsoffu03worl.

[99]   Steele, S. *Ind. Eng. Chem. Anal. Ed.*, vol. 5, no. 3 (May 1933), pp. 202–206. DOI: 10.1021/ac50083a025.

[100] Egerton, A., Smith, F. L., and Ubbelohde, A. R. *Philos. Trans. R. Soc. A Math. Phys. Eng. Sci.*, vol. 234, no. 744 (July 1935), pp. 433–521. DOI: 10.1098/rsta.1935.0013.

[101] Downs, D., Walsh, A. D., and Wheeler, R. W. *Philos. Trans. R. Soc. London. Ser. A, Math. Phys. Sci.*, vol. 243, no. 870 (July 1951), pp. 463–524. URL: http://www.jstor.org/stable/91560.

[102] Pahnke, A. J., Cohen, P. M., and Sturgis, B. M. *Ind. Eng. Chem.*, vol. 46, no. 5 (May 1954), pp. 1024–1029. DOI: 10.1021/ie50533a058.

[103] Roblee, L. *Combust. Flame*, vol. 5 (Mar. 1961), pp. 229–234. DOI: 10.1016/0010-2180(61)90101-8.

[104] Martinengo, A., Melczer, J., and Schlimme, E. *Symp. Combust.*, vol. 10, no. 1 (Jan. 1965), pp. 323–330. DOI: 10.1016/S0082-0784(65)80179-5.

[105] Affleck, W. and Fish, A. *Symp. Combust.*, vol. 11, no. 1 (Jan. 1967), pp. 1003–1013. DOI: 10.1016/S0082-0784(67)80227-3.

[106] Beeley, P., Griffiths, J. F., and Gray, P. *Combust. Flame*, vol. 39, no. 3 (Nov. 1980), pp. 269–281. DOI: 10.1016/0010-2180(80)90023-1.

[107] Minetti, R., Ribaucour, M., Carlier, M., Fittschen, C., and Sochet, L. R. *Combust. Flame*, vol. 96, no. 3 (Feb. 1994), pp. 201–211. DOI: 10.1016/0010-2180(94)90009-4.

[108] Minetti, R., Carlier, M., Ribaucour, M., Therssen, E., and Sochet, L. R. *Combust. Flame*, vol. 102, no. 3 (Aug. 1995), pp. 298–309. DOI: 10.1016/0010-2180(94)00236-L.

[109] Minetti, R., Carlier, M., Ribaucour, M., Therssen, E., and Sochet, L. R. *Symp. Combust.*, vol. 26, no. 1 (1996), pp. 747–753. DOI: 10.1016/S0082-0784(96)80283-9.

[110] Lemaire, O., Ribaucour, M., Carlier, M., and Minetti, R. *Combust. Flame*, vol. 127, no. 1-2 (Oct. 2001), pp. 1971–1980. DOI: 10.1016/S0010-2180(01)00301-7.

[111] Ribaucour, M., Lemaire, O., and Minetti, R. *Proc. Combust. Inst.*, vol. 29, no. 1 (Jan. 2002), pp. 1303–1310. DOI: 10.1016/S1540-7489(02)80160-2.

[112] He, X. "An investigation of iso-octane auto-ignition using a rapid compression facility". Dissertation. University of Michigan, 2005. URL: http://search.proquest.com/docview/305422688?accountid=14518.

[113] Mittal, G. "A Rapid Compression Machine - Design, Characterization, and Autoignition Investigations". Dissertation. Case Western Reserve University, 2006. URL: http://etd.ohiolink.edu/send-pdf.cgi/Mittal%20Gaurav.pdf?acc%5C_num=case1130184196.

[114] Mittal, G. and Sung, C.-J. *Combust. Sci. Technol.*, vol. 179, no. 3 (2007), pp. 497–530. DOI: 10.1080/00102200600671898.

[115] He, X., Walton, S. M., Zigler, B. T., Wooldridge, M. S., and Atreya, A. *Int. J. Chem. Kinet.*, vol. 39, no. 9 (Sept. 2007), pp. 498–517. DOI: 10.1002/kin.20254.

[116] Walton, S. M. "Experimental investigation of the auto-ignition characteristics of oxygenated reference fuel compounds". Dissertation. University of Michigan, 2008. URL: http://search.proquest.com/docview/304574882?accountid=14518.

[117] Walton, S. M., Karwat, D. M. A., Teini, P. D., Gorny, A. M., and Wooldridge, M. S. *Fuel*, vol. 90, no. 5 (May 2011), pp. 1796–1804. DOI: 10.1016/j.fuel.2011.01.028.

[118] Karwat, D. M. A., Wagnon, S. W., Wooldridge, M. S., and Westbrook, C. K. *J. Phys. Chem. A*, vol. 116, no. 51 (Dec. 2012), pp. 12406–12421. DOI: 10.1021/jp309358h.

[119] Karwat, D. M. A., Wagnon, S. W., Wooldridge, M. S., and Westbrook, C. K. *Combust. Flame*, vol. 160, no. 12 (Dec. 2013), pp. 2693–2706. DOI: 10.1016/j.combustflame.2013.06.029.

[120] Kumar, K., Mittal, G., and Sung, C.-J. *Combust. Flame*, vol. 156, no. 6 (June 2009), pp. 1278–1288. DOI: 10.1016/j.combustflame.2009.01.009.

[121] Das, A. K., Uddi, M., and Sung, C.-J. *Combust. Flame*, vol. 159, no. 12 (Dec. 2012), pp. 3493–3501. DOI: 10.1016/j.combustflame.2012.06.020.

[122] Mittal, G., Sung, C.-J., and Yetter, R. A. *Int. J. Chem. Kinet.*, vol. 38, no. 8 (2006), pp. 516–529. DOI: 10.1002/kin.20180.

[123] Mittal, G., Chaos, M., Sung, C.-J., and Dryer, F. L. *Fuel Process. Technol.*, vol. 89, no. 12 (Dec. 2008), pp. 1244–1254. DOI: 10.1016/j.fuproc.2008.05.021.

[124] Kumar, K. and Sung, C.-J. *Int. J. Chem. Kinet.*, vol. 43, no. 4 (Apr. 2011), pp. 175–184. DOI: 10.1002/kin.20546.

[125] Mittal, G. and Sung, C.-J. *Combust. Flame*, vol. 150, no. 4 (2007), pp. 355–368. DOI: 10.1016/j.combustflame.2007.04.014.

[126] Mittal, G. and Sung, C.-J. *Combust. Flame*, vol. 155, no. 3 (Nov. 2008), pp. 431–439. DOI: 10.1016/j.combustflame.2008.05.003.

[127] Kumar, K. and Sung, C.-J. *Combust. Flame*, vol. 157, no. 4 (Apr. 2010), pp. 676–685. DOI: 10.1016/j.combustflame.2010.01.001.

[128] Dooley, S., Won, S. H., Chaos, M., Heyne, J. S., Ju, Y., Dryer, F. L., et al. *Combust. Flame*, vol. 157, no. 12 (Dec. 2010), pp. 2333–2339. DOI: 10.1016/j.combustflame.2010.07.001.

[129] Hui, X., Kumar, K., Sung, C.-J., Edwards, T., and Gardner, D. *Fuel*, vol. 98 (Aug. 2012), pp. 176–182. DOI: 10.1016/j.fuel.2012.03.040.

[130] Kéromnès, A., Metcalfe, W. K., Heufer, K. A., Donohoe, N., Das, A. K., Sung, C.-J., et al. *Combust. Flame*, vol. 160 (Mar. 2013), pp. 995–1011. DOI: `10.1016/j.combustflame.2013.01.001`.

[131] Kukkadapu, G., Kumar, K., Sung, C.-J., Mehl, M., and Pitz, W. J. *Proc. Combust. Inst.*, vol. 34, no. 1 (Jan. 2013), pp. 345–352. DOI: `10.1016/j.proci.2012.06.135`.

[132] Kukkadapu, G., Kumar, K., Sung, C.-J., Mehl, M., and Pitz, W. J. *Combust. Flame*, vol. 159, no. 10 (Oct. 2012), pp. 3066–3078. DOI: `10.1016/j.combustflame.2012.05.008`.

[133] Yaws, C. *Chemical Properties Handbook*. 1999. URL: `http://knovel.com/web/portal/browse/display?%5C_EXT%5C_KNOVEL%5C_DISPLAY%5C_bookid=49%5C&VerticalID=0`.

[134] Lee, D. and Hochgreb, S. *Combust. Flame*, vol. 114, no. 3-4 (Aug. 1998), pp. 531–545. DOI: `10.1016/S0010-2180(97)00327-1`.

[135] Mittal, G. and Sung, C.-J. *Combust. Flame*, vol. 145, no. 1-2 (Apr. 2006), pp. 160–180. DOI: `10.1016/j.combustflame.2005.10.019`.

[136] Desgroux, P., Gasnot, L., and Sochet, L. R. *Appl. Phys. B Laser Opt.*, vol. 61, no. 1 (July 1995), pp. 69–72. DOI: `10.1007/BF01090974`.

[137] *CHEMKIN-PRO*. San Diego, 2013.

[138] Corless, R. M., Gonnet, G. H., Hare, D. E. G., Jeffrey, D. J., and Knuth, D. E. *Adv. Comput. Math.*, vol. 5, no. 1 (Dec. 1996), pp. 329–359. DOI: `10.1007/BF02124750`.

[139] Taylor, J. R. *An Introduction to Error Analysis*. Mill Valley, CA, 1982.

[140] Dalton, J. *A Journal of Natural Philosophy, Chemistry, and the Arts*, vol. 5 (Oct. 1801), pp. 241–244. URL: `https://archive.org/details/journalofnatural04lond`.

[141] Gillespie, L. *Phys. Rev.*, vol. 36, no. 1 (July 1930), pp. 121–131. DOI: `10.1103/PhysRev.36.121`.

[142]   Sparkman, O. D., Penton, Z. E., and Kitson, F. G. *Gas Chromatography and Mass Spectrometry: A Practical Guide* (2011), pp. 15–83. DOI: 10.1016/b978-0-12-373628-4.00002-2.

[143]   Sparkman, O. D., Penton, Z. E., and Kitson, F. G. *Gas Chromatography and Mass Spectrometry: A Practical Guide* (2011), pp. 89–148. DOI: 10.1016/b978-0-12-373628-4.00004-6.

[144]   Sarathy, S. M., Vranckx, S., Yasunaga, K., Mehl, M., Oßwald, P., Metcalfe, W. K., et al. *Combust. Flame*, vol. 159, no. 6 (June 2012), pp. 2028–2055. DOI: 10.1016/j.combustflame.2011.12.017.

[145]   Frassoldati, A., Grana, R., Faravelli, T., Ranzi, E., Oßwald, P., and Kohse-Höinghaus, K. *Combust. Flame*, vol. 159, no. 7 (July 2012), pp. 2295–2311. DOI: 10.1016/j.combustflame.2012.03.002.

[146]   Merchant, S. S., Zanoelo, E. F., Speth, R. L., Harper, M. R., Van Geem, K. M., and Green, W. H. *Combust. Flame*, vol. 160, no. 10 (Oct. 2013), pp. 1907–1929. DOI: 10.1016/j.combustflame.2013.04.023.

[147]   McEnally, C. S. and Pfefferle, L. D. *Proc. Combust. Inst.*, vol. 30, no. 1 (Jan. 2005), pp. 1363–1370. DOI: 10.1016/j.proci.2004.07.033.

[148]   Togbé, C., Mzé-Ahmed, A., and Dagaut, P. *Energy Fuel*, vol. 24, no. 9 (Sept. 2010), pp. 5244–5256. DOI: 10.1021/ef1008488.

[149]   Liu, W., Kelley, A. P., and Law, C. K. *Proc. Combust. Inst.*, vol. 33, no. 1 (Sept. 2011), pp. 995–1002. DOI: 10.1016/j.proci.2010.05.084.

[150]   Welz, O., Savee, J. D., Eskola, A. J., Sheps, L., Osborn, D. L., and Taatjes, C. A. *Proc. Combust. Inst.*, vol. 34, no. 1 (June 2013), pp. 493–500. DOI: 10.1016/j.proci.2012.05.058.

[151]   Silva, G. da, Bozzelli, J. W., Liang, L., and Farrell, J. T. *J. Phys. Chem. A*, vol. 113, no. 31 (Aug. 2009), pp. 8923–8933. DOI: 10.1021/jp903210a.

[152] Heufer, K. A., Sarathy, S. M., Curran, H. J., Davis, A. C., Westbrook, C. K., and Pitz, W. J. *Energy Fuel*, vol. 26, no. 11 (Oct. 2012), pp. 6678–6685. DOI: `10.1021/ef3012596`.

[153] Welz, O., Klippenstein, S. J., Harding, L. B., Taatjes, C. A., and Zádor, J. *J. Phys. Chem. Lett.*, vol. 4, no. 3 (Feb. 2013), pp. 350–354. DOI: `10.1021/jz302004w`.

[154] Ray, D. and Waddington, D. *Combust. Flame*, vol. 20, no. 3 (June 1973), pp. 327–334. DOI: `10.1016/0010-2180(73)90024-2`.

[155] Sway, M. I. and Waddington, D. J. *J. Chem. Soc. Perkin Trans. 2*, no. 2 (1983), p. 139. DOI: `10.1039/p29830000139`.

[156] Nakamura, H., Darcy, D., Mehl, M., Tobin, C. J., Metcalfe, W. K., Pitz, W. J., et al. *Combust. Flame*, vol. 161, no. 1 (Jan. 2014), pp. 49–64. DOI: `10.1016/j.combustflame.2013.08.002`.

[157] Silke, E. J., Pitz, W. J., Westbrook, C. K., and Ribaucour, M. *J. Phys. Chem. A*, vol. 111, no. 19 (May 2007), pp. 3761–3775. DOI: `10.1021/jp067592d`.

[158] Sivaramakrishnan, R. and Michael, J. *Combust. Flame*, vol. 156, no. 5 (May 2009), pp. 1126–1134. DOI: `10.1016/j.combustflame.2008.10.010`.

[159] Sarathy, S. M., Westbrook, C. K., Mehl, M., Pitz, W. J., Togbé, C., Dagaut, P., et al. *Combust. Flame*, vol. 158, no. 12 (Dec. 2011), pp. 2338–2357. DOI: `10.1016/j.combustflame.2011.05.007`.

[160] Pitz, W. J., Skeen, S. A., Mehl, M., Hansen, N., and Silke, E. J. "Chemical Kinetic Modeling of Low Pressure Methycyclohexane Flames". In: *8th US Natl. Tech. Meet. Combust. Inst.* University of Utah. Park City, UT, May 2013, Paper 1B12.

[161] Fernandes, R. X., Zádor, J., Jusinski, L. E., Miller, J. A., and Taatjes, C. A. *Phys. Chem. Chem. Phys.*, vol. 11, no. 9 (Mar. 2009), pp. 1320–1327. DOI: `10.1039/b819825j`.

[162] Curran, H. J., Gaffuri, P., Pitz, W. J., and Westbrook, C. K. *Combust. Flame*, vol. 129, no. 3 (May 2002), pp. 253–280. DOI: `10.1016/S0010-2180(01)00373-X`.

[163] Zádor, J., Taatjes, C. A., and Fernandes, R. X. *Prog. Energy Combust. Sci.*, vol. 37, no. 4 (Aug. 2011), pp. 371–421. DOI: 10.1016/j.pecs.2010.06.006.

[164] Aguilera-Iparraguirre, J., Curran, H. J., Klopper, W., and Simmie, J. M. *J. Phys. Chem. A*, vol. 112, no. 30 (July 2008), pp. 7047–7054. DOI: 10.1021/jp8012464.

Appendix A

Definition of Species Names in

the Methylcyclohexane Mechanism

The following is also available as supplemental material to the associated article [90]. It was generated by Dr. William J. Pitz, Lawrence Livermore National Laboratory.

includes/mch-species.pdf

includes/mch-species.pdf

includes/mch-species.pdf

includes/mch-species.pdf

includes/mch-species.pdf

includes/mch-species.pdf

includes/mch-species.pdf

includes/mch-species.pdf

includes/mch-species.pdf

includes/mch-species.pdf

includes/mch-species.pdf

includes/mch-species.pdf

includes/mch-species.pdf

includes/mch-species.pdf

includes/mch-species.pdf

includes/mch-species.pdf

includes/mch-species.pdf

includes/mch-species.pdf

includes/mch-species.pdf

includes/mch-species.pdf

includes/mch-species.pdf

includes/mch-species.pdf

Appendix B

CanSen

CanSen is a Python script that I wrote to simplify the transition from Senkin-style, input-file-based usage to the Cantera-style script-based usage. The documentation included below is also available on the Web at http://bryanwweber.github.io/CanSen/html/index.html.

includes/CanSen.pdf

includes/CanSen.pdf

includes/CanSen.pdf

includes/CanSen.pdf

includes/CanSen.pdf

includes/CanSen.pdf

includes/CanSen.pdf

includes/CanSen.pdf

includes/CanSen.pdf

includes/CanSen.pdf

includes/CanSen.pdf

includes/CanSen.pdf

includes/CanSen.pdf

includes/CanSen.pdf

includes/CanSen.pdf

includes/CanSen.pdf

includes/CanSen.pdf

includes/CanSen.pdf

includes/CanSen.pdf

includes/CanSen.pdf

includes/CanSen.pdf

includes/CanSen.pdf

includes/CanSen.pdf

includes/CanSen.pdf

Appendix C

pysens

This appendix contains the code for `pysens`. `pysens` is a Python wrapper for sensitivity analysis in CHEMKIN-Pro. This program runs a brute force, one-at-a-time sensitivity analysis of the ignition delay for a given mechanism. It was used to conduct the sensitivty analyses in Chapters 4 and 5

Usage:
Download the repository by using git

`git clone git://github.com/bryanwweber/pysens.git`

No other compilation is necessary. Python 3 is required. The runtime behavior of the script is configured by setting options in the `pysens.conf` file. A sample `pysens.conf` is included in the distribution and reproduced below.

The script can be run on Linux either by setting the executable bit and executing the program from the shell e.g.

`./run_sens.py`

or by calling

`python3 run_sens.py.`

On Windows, it should be run by

`py run_sens.py`

Note: I haven't tested this on Windows

`pysens.conf` options:
The `pysens.conf` file must either have `[DEFAULT]` on the first line, or one of the following options. No other text is supported on the first line. If options are given that aren't specified below, they will be ignored.

The options can be specified by:

`option = value or option : value`

The following options are available:

`reactions – The set of reactions to be analyzed. Can be one of:`

all - use all of the reactions in the mechanism
comma-separated list (e.g. 1,2,3) - use the specified reactions
colon-separated values - specify a range of reactions
                         with either start:stop or
                         start:interval:stop syntax.
                         If stop is not given, it
                         defaults to the number of
                         reactions in the mechanism.
                         Thus, all and 1: are
                         equivalent. end is a
                         synonym for the number
                         of reactions. E.g. 1:10 or
                         1:2:10 or 1:2: or 1:2:end

mech input file - The mechanism to be analyzed.

thermo input file - Optional if the thermo information
                    is specified in the mech input file.

outputfile - The base name of the output file. The full
             output file name will be set by concatenating
             outputfile + rfactor + sim input file.

factors - The multiplication factors to be considered.
          Multiple multiplication factors should be
          separated by commas.

sim input files - Valid CHEMKIN-Pro input files for the
                  test cases desired.

chemkin root - The root directory of the CHEMKIN-Pro
               install. Accepts shell variables, including
               those set by the CHEMKIN setup script
               that should run at logon.

Sample pysens.conf **file:**

```
reactions : 1,2
mech input file : Burke-H2-2012.inp
thermo input file :
outputfile = tignsens
factors : 1, 2
sim input files : test.inp
chemkin root : $REACTION_DIR/chemkin15131_linuxx8664
```

The following is the code that makes up this script.

run_sens.py, the main driver script

```python
#! /usr/bin/python3 -u

# System imports
import re
import os
import subprocess
import shutil
import sys
from itertools import product
from decimal import *

# Local imports
from mechinterp import mechinterp
from sens_helper import *

def main():
    # Read the configuration file.
    config = NoSectionConfigParser()
    config.read('pysens.conf')
    default = config['DEFAULT']

    # Set the location of the CHEMKIN executable files. Expand any shell
    # variables in the input.
    reactiondir = default['chemkin root']
    if '$' in reactiondir:
        reactiondir = os.path.expandvars(reactiondir)
        if os.path.isdir(reactiondir):
            reactor = os.path.join(reactiondir,'bin','CKReactorGenericClosed')
            ckinterp = os.path.join(reactiondir,'bin','chem')
            if not os.path.isfile(reactor) or not os.path.isfile(ckinterp):
                print("Error: The reactor and CHEMKIN interpreter must "
                        "exist at CHEMKIN_ROOT/bin/")
                sys.exit(1)
        else:
            print("Error: The proper path to the CHEMKIN root "
                    "directory must be specified")
            sys.exit(1)

    # Set the mechanism to be used.
    if ('mech input file' in default and
            os.path.isfile(default['mech input file'])):
        inputfilename = default['mech input file']
    else:
        print("Error: the mechanism file must be specified in the "
                "configuration file, and it must exist")
        sys.exit(1)
```

```python
47
        # Set the simulation input file to be used.
49      if 'sim input files' in default:
            siminputfiles = [x.strip() for x in
51                              default['sim input files'].split(',')
                             ]
53          for fname in siminputfiles:
                if not os.path.isfile(fname):
55                  print("Error: the specified input file {} does not "
                          "exist".format(fname))
57                  sys.exit(1)
        else:
59          print("Error: the simulation input file must be specified in "
                  "the configuration file")
61          sys.exit(1)

63      # Set the multiplication factors to be used.
        if 'factors' in default:
65          multfactors = [x.strip for x in default['factors'].split(',')]
        else:
67          print("Error: at least one multiplication factor must be "
                  "specified in the configuration file")
69          sys.exit(1)

71      #Set the base of the csv output file name.
        if 'outputfile' in default:
73          sensfilenamebase = default['outputfile']
        else:
75          print("Error: the base of the csv output filename must be "
                  "specified in the configuration file")
77          sys.exit(1)

79      # Compile the required regular expressions
        commentmatch = re.compile(r'^\!')
81      newlinematch = re.compile(r'^\n')

83      # The following regular expressions match the keywords we expect to
        #see. The `(?i)` indicates case insensitive. For certain keywords,
85      # we want to match the keyword even if there is space at the
        # beginning of the line; these keywords have `^[\s]*`.
87      lowmatch = re.compile(r'(?i)^[\s]*LOW')
        highmatch = re.compile(r'(?i)^[\s]*HIGH')
89      dupmatch = re.compile(r'(?i)\bDUP\b|\bDUPLICATE\b')
        endmatch = re.compile(r'(?i)^END')
91      revmatch = re.compile(r'(?i)^[\s]*REV')
        plogmatch = re.compile(r'(?i)^[\s]*PLOG')
93      Amatch = re.compile(r'((?<![\w\-])([-+]?[0-9]+(\.[0-9]+)?'
```

178

```python
                        '([eE][-+]?[0-9]+)?)(?!\w))'
95                      )
        reacmatch = re.compile(r'((^|^[\s]+)[\s\w\d()+=<>\- *.]+?(?=\s\d))')
97

        # Open, read, and close the input file. The lines of the input file
99      # are stored in the list `lines`.
        try:
101         with open(inputfilename, 'rt') as inputfile:
                lines = inputfile.readlines()
103     except UnicodeDecodeError:
            with open(inputfilename,'rt', encoding='latin-1') as inputfile:
105             lines = inputfile.readlines()
        else:
107         print("Error: I can't decode the input file. Try saving it "
                  "as UTF-8")
109         sys.exit(1)

111     # Call the mechanism interpreter module. The mechinterp function
        # returns a tuple of lists plus a boolean. The lists contain the
113     # line numbers in the input file of the reactions, the lines between
        # each reaction, and whether a reaction has auxiliary information.
115     # The boolean checks whether the thermo data is available in the
        # chemistry file or if it should be taken from a separate file.
117     # These are stored, respectively, in `reacLines`, `searchLines`,
        # `extraInfo` and `thermInChem`.
119     reacLines, searchLines, extraInfo, thermInChem, = mechinterp(lines)

121     # Set the thermo file, if necessary.
        if (not thermInChem and 'thermo input file' in default and
123             os.path.isfile(default['thermo input file'])):
            thermfilename = default['thermo input file']
125     elif (not thermInChem and (not 'thermo input file' in default or not
                os.path.isfile(default['thermo input file']))):
127         print("Error: the thermo file must be specified in the "
                  "configuration file, and it must exist")
129         sys.exit(1)

131     # Set the reactions we want to work with.
        numRxns = len(reacLines)-1
133     if not 'reactions' in default:
            print("Error: the reactions to study must be specified in the "
135             "configuration file")
            sys.exit(1)
137     else:
            wantrxns = default['reactions']
139
        if wantrxns == all:
```

```python
            wantreactions = [x + 1 for x in range(numRxns)]
            print("All {} reactions are considered in these "
                  "analyses".format(numRxns))
        elif ',' in wantrxns and ':' in wantrxns:
            print("Error: use one of commas or colons to separate the wanted "
                  "reactions")
            sys.exit(1)
        elif ',' in wantrxns:
            wantreactions = [int(number) for number in wantrxns.split(',') if
                number]
            print("The reactions considered in these analyses are "
                  "{}".format(wantreactions))
        elif ':' in wantrxns:
            if wantrxns.endswith(':') or wantrxns.endswith('end'):
                spl = list(map(int, wantrxns.split(':')[:-1]))
                spl.append(numRxns)
            else:
                spl = list(map(int, wantrxns.split(':')))

            if len(spl) == 2:
                wantreactions = list(range(spl[0], spl[1] + 1))
            elif len(spl) == 3:
                if spl[1] >= 1:
                    wantreactions = list(range(spl[0], spl[2] + 1, spl[1]))
                else:
                    print("Error: the interval in the reactions specification "
                          "must be >= 1")
                    sys.exit(1)
            else:
                print("Error: Specify either start:stop or start:interval:stop "
                      "for reactions")
                sys.exit(1)
            print("The reactions considered in these analyses are "
                  "{}".format(wantreactions))
        else:
            wantreactions = list(int(wantrxns))
            print("The reaction considered in these analyses is "
                  "{}".format(wantreactions))

        # Set filenames of simulation and output files.
        simoutputfile = 'test.out'
        chemoutput = 'chem.out'
        chemasc = 'chem.asc'
        totalCases = len(wantreactions)*len(siminputfiles)*len(multfactors)
        for (j, (inpfile, multfactor) in
                enumerate(product(siminputfiles, multfactors))):
            csvoutput = (sensfilenamebase + '_' + inpfile.strip('.inp') + '_' +
```

```
                multfactor + 'x.csv')
189        with open(csvoutput, 'at') as tignsens:

191            # Loop through the reaction numbers in `wantreaction`. `i`
               # is the loop variable.
193            for i, wantreaction in enumerate(wantreactions):

195                # Python is zero-based, so we have to subtract 1 from
                   # the numbers in `wantreaction` to properly find the
197                # index of the other lists
                   rxnNum = wantreaction - 1
199
                   # outLines is the list of lines to write to the chem.inp
201                # file to be run in the simulation. It needs to be reset
                   # on every loop or more than one reaction will be
203                # modified at a time. Python is "pointer-based", so we
                   # have to set `outLines` equal to a slice of `lines`,
205                # the input list of lines (the slice happens to be the
                   # whole list).
207                outLines = lines[:]

209                # Grab the line from the input file that matches the
                   # reaction we're working on.
211                line = lines[reacLines[rxnNum]]

213                # Find the Arrhenius coefficient on this line.
                   Afactor = Amatch.search(line)
215
                   # Set `x` to the arbitrary precision conversion of the
217                # first matching string from the Afactor match. Multiply
                   # `x` by `multfactor`. Reassemble the modified reaction
219                # line with the new Arrhenius coefficient, and set the
                   # correct line in `outLines` to the modified line.
221                x = Decimal(Afactor.group(1))
                   x = Decimal(multfactor)*x
223                modline = line[:Afactor.start()] + str(x) +
                       line[Afactor.end():]
225                outLines[reacLines[rxnNum]] = modline

227                # Check if there is auxiliary information for the
                   # current reaction.
229                if extraInfo[rxnNum] > 0:

231                    # If there is auxiliary information, initialize a
                       # list for input lines that will be sent for
233                    # modification. Then loop through the lines in the
                       # searchLines list for the correct reaction number
```

```python
                        # and construct the list to send for modification.
                        sendLines = [0]*len(searchLines[rxnNum])
                        for n in range(len(searchLines[rxnNum])):
                            sendLines[n] = lines[searchLines[rxnNum][n]]

                        # If structure to check which type of auxiliary
                        # information is present and send the proper
                        # compiled regular expression to auxcheck. `ret` is
                        # the returned list of modified lines.
                        if extraInfo[rxnNum] == 1:
                            ret = auxcheck(sendLines, lowmatch, multfactor)
                        elif extraInfo[rxnNum] == 2:
                            ret = auxcheck(sendLines, highmatch, multfactor)
                        elif extraInfo[rxnNum] == 3:
                            ret = auxcheck(sendLines, revmatch, multfactor)
                        elif extraInfo[rxnNum] == 4:
                            ret = auxcheck(sendLines, plogmatch, multfactor)
                        elif extraInfo[rxnNum] == 5:
                            ret = chebcheck(sendLines, multfactor)

                        # Loop through the returned lines and set the
                        # correct line in the `outLines` list to the
                        # modified lines.
                        for n in range(len(searchLines[rxnNum])):
                            outLines[searchLines[rxnNum][n]] = ret[n]

                # Create a folder in which simulations will be run,
                # after checking for its existence.
                chemfolder = 'Reaction' + str(rxnNum + 1)
                if not os.path.exists(chemfolder):
                    os.makedirs(chemfolder)

                # Copy the various files we will need to run the
                # simulation into the simulation directory.
                shutil.copyfile(inpfile, os.path.join(chemfolder, inpfile))
                shutil.copyfile('CKSolnList.txt', os.path.join(chemfolder,
                    'CKSolnList.txt'))
                shutil.copyfile(os.path.join(reactiondir, 'data',
                                'chemkindata.dtd'), os.path.join(chemfolder,
                                'chemkindata.dtd')
                                )

                # If the thermo data is in the chemistry file, we don't
                # have to copy therm.dat
                if not thermInChem:
                    shutil.copyfile(thermfilename, os.path.join(chemfolder,
                        thermfilename))
```

```python
283             #Change directory into the simulation directory.
                with cd(chemfolder):

285
                    # Set the filename for the modified chemistry input
287                 # file. Open the modified chemistry input file with
                    # write access, and write the file. This write is
289                 # buffered. Close the modified chemistry input file.
                    chemfilename = 'chem' + str(rxnNum + 1) + '.inp'
291                 with open(chemfilename, 'wt') as chemfile:
                        for outLine in outLines:
293                         chemfile.write(outLine)

295                 # Call the CHEMKIN-Pro interpreter, then the solver,
                    # then the post-processor, then the transpose
297                 # utility to create the solution .csv files. First
                    # check if we need the thermo file.
299                 if thermInChem:
                        subprocess.call([ckinterp, '-i', chemfilename, '-o',
301                                     chemoutput, '-c', chemasc]
                                        )
303                 else:
                        subprocess.call([ckinterp, '-i', chemfilename, '-o',
305                                     chemoutput, '-d', thermfilename, '-c',
                                        chemasc]
307                                     )
                    subprocess.call([reactor, '-i',inpfile, '-o',
309                                 simoutputfile, 'Pro', '-c', chemasc]
                                    )
311                 subprocess.call(['GetSolution', 'CKSolnList.txt',
                                    'XMLdata.zip']
313                                 )
                    subprocess.call(['CKSolnTranspose'])

315
                    # Open, read, and close the file with the solution
317                 # information.
                    with open('CKSoln_solution_point_value_vs_solution_'
319                             'number.csv', 'r') as outputFile:
                        ignLines = outputFile.readlines()

321
                    # Find the columns with 'Ignition' in the title -
323                 # these are the ignition delays. Then, convert the
                    # ignition delay to a float.
325                 ignCol = [x for x,val in enumerate(ignLines[0].split(','))
                                if 'Ignition' in val
327                             ]
                    ignDelay = [float(k) for k in
```

```python
                                     [ignLines[1].split(',')[x].strip() for x in
                                     ignCol]
                                     ]

                    # Create a list for writing to the output file,
                    # including the corrected (i.e. one-based) reaction
                    # number, the multiplication factor, and the
                    # ignition delay. Format the list into a comma-
                    # separated format and convert to a string. Then
                    # append a newline and print the list to the
                    # sensitivity output file.
                    ignSens = [rxnNum + 1, multfactor,'','',
                                     reacmatch.search(line).group(1).strip()
                                     ]
                    ignSens[2:2] = ignDelay
                    printsens = ','.join(map(str, ignSens))
                    tignsens.write(printsens + '\n')
                    tignsens.flush()

                    # Remove the simulation directory.
                    shutil.rmtree(chemfolder)

                    #Print to the screen some progress information.
                    caseNo = i + 1 + j*len(wantreactions)
                    print('Case {0} of {1} \nReaction #: {2} \nIgnition Delay:'
                          '{3}\nInput File: {4}\nFactor: {5}'.format(caseNo,
                          totalCases, rxnNum + 1, ignDelay, inpfile,
                          multfactor)
                          )

if __name__ == '__main__':
    main()
```

mechinterp.py, containing the mechanism interpreter

```python
def mechinterp(lines):
    """Interpret CHEMKIN chemistry input files and return lists of line
    numbers and reaction info.

    INPUT:
    lines - list of strings, lines of the CHEMKIN format chemistry input file
    numRxns - integer, number of reactions in the input mechanims
    OUTPUT:
    reacLines - list of integers, line numbers of reactions in the input set
                    of lines
    searchLines - list of lists of integers, line numbers of the lines between
                        the reactions
    extraInfo - list of integers, status of auxiliary information for a
                    reaction
                        0 - no auxiliary information
                        1 - LOW parameter specified
                        2 - HIGH parameter specified
                        3 - REV reaction specified
                        4 - PLOG reaction specified
                        5 - CHEB reaction specified
    thermInChem - boolean indicating the status of the thermodynamic data.
                    False - thermo data is stored in a separate file
                    True - thermo data is stored in the chemistry file

    """

    # Import the module for regular expressions.
    import re

    # Compile regular expressions for each of the expected keywords to
    # be encountered. (?i) indicates ignore case.
    reactionmatch = re.compile(r'=(?!.*\!)')
    commentmatch = re.compile(r'^\!')
    newlinematch = re.compile(r'^\n')
    lowmatch = re.compile(r'(?i)^[\s]*LOW')
    highmatch = re.compile(r'(?i)^[\s]*HIGH')
    dupmatch = re.compile(r'(?i)\bDUP\b|\bDUPLICATE\b')
    endmatch = re.compile(r'(?i)^END')
    revmatch = re.compile(r'(?i)^[\s]*REV')
    plogmatch = re.compile(r'(?i)^[\s]*PLOG')
    chebmatch = re.compile(r'(?i)^[\s]*CHEB')
    thermmatch = re.compile(r'(?i)THERM ALL|THERMO ALL')

    # Initialize 'reactionNum', a counter of the number of reactions,
    # and 'reacLines', a zero-based list of the line numbers of the
    # reactions in the input file. Set the 'numRxns' element of the
```

```
47      # 'reacLines' list to the number of lines in the input file so that
        # it can be used as a search parameter later.
49      reactionNum = 0
        reacLines = []

51

        # Begin a loop over all of the lines in the input file. The lines
53      # are stored in the variable 'line' for each iteration.
        for lineNum,line in enumerate(lines):

55

            # We have to reverse the line to properly check for a reaction.
57          # This eliminates the case where an auxiliary line may contain
            # an = sign in a comment, which would otherwise be included in
59          # the reaction list. Since Python does not allow variable length
            # look behind, the workaround is to reverse the string and use
61          # variable length look ahead.
            line = line[::-1]

63

            # Check for lines that are reactions, defined by the
65          # reactionmatch regular expression
            rxncond = reactionmatch.search(line)

67

            # If the reaction condition contains information the line is a
69          # reaction. Put the line number of this reaction in the
            # 'reacLines' list, and increment the reaction counter. Remember
71          # that since Python is zero-based, the real reaction number of a
            # reaction will be one more than the number from this loop
73          if rxncond is not None:
                reacLines.append(lineNum)
75              reactionNum += 1

77      # Append the last line number to the reacLines list so that it can
        # be used to determine the `searchLines` - see below.
79      reacLines.append(len(lines))

81      # Initialize two lists to hold information about the reactions.
        # 'searchLines' is a list of lists of the line numbers between each
83      # reaction. 'extraInfo' is a list of integers corresponding to each
        # type of reaction rate modification.
85      searchLines = []
        extraInfo = []

87

        # Begin loop to find and read all of the lines between each reaction
89      # to check for auxiliary information.
        for i in range(len(reacLines)-1):

91

            # Fill the ith element of 'searchLines' with a list of lines
93          # in the input file between the line number in the ith element
```

```python
            # of 'reacLines' and the line number in the (i+1)th element. Add
            # 1 to the first line number to avoid the reaction line itself.
            # The 'range' function automatically excludes the last number in
            # the range, which would be the next reaction, so there is no
            # need to subtract one from the second line number.
            searchLines.append(list(range(reacLines[i]+1,reacLines[i+1])))


            # Loop over the line numbers in the previously appended (i.e.
            # last) element of 'searchLines' to look for auxiliary
            # information.
            for lineNum in searchLines[-1]:
                line = lines[lineNum]

                # Check if the line is a comment or blank.
                blankcond = newlinematch.match(line)
                comcond = commentmatch.match(line)
                if blankcond is None and comcond is None:

                    # Use an if/elif block to check whether the current line
                    # contains any auxiliary information. The options 'LOW',
                    # 'HIGH', 'REV', 'PLOG', and 'CHEB' are mutually
                    # exclusive, so there should be no chance of a different
                    # type being present. Therefore, break out of the loop
                    # through `searchLines[i]` when a keyword is found.
                    lowcond = lowmatch.search(line)
                    highcond = highmatch.search(line)
                    revcond = revmatch.search(line)
                    plogcond = plogmatch.search(line)
                    chebcond = chebmatch.search(line)
                    if lowcond is not None:
                        extraInfo.append(1)
                        break
                    elif highcond is not None:
                        extraInfo.append(2)
                        break
                    elif revcond is not None:
                        extraInfo.append(3)
                        break
                    elif plogcond is not None:
                        extraInfo.append(4)
                        break
                    elif chebcond is not None:
                        extraInfo.append(5)
                        break

        # Check if the thermo data is included in the chemistry. Store the
        # result in the `thermInChem` boolean, where `True` indicates that
```

```python
141    # no separate thermo file is required.
       for line in lines:
143        if thermmatch.search(line) is not None:
               thermInChem = True
145            break
           else:
147            thermInChem = False

149    # Return the output information
       return reacLines, searchLines, extraInfo, thermInChem,
```

sens_helper.py, containing helper functions

```python
# System imports
import re
import os
from decimal import *
import configparser
from io import StringIO


class NoSectionConfigParser(configparser.ConfigParser):
    """
    Subclass of ConfigParser that adds a [DEFAULT] header if one isn't present.
    """
    def read(self,filename):
        try:
            text = open(filename).read()
        except IOError:
            pass
        else:
            if not text.startswith('[DEFAULT]'):
                file = StringIO("[DEFAULT]\n" + text)
            else:
                file = StringIO(text)

            self.readfp(file,filename)
#############################################################################
def chebcheck(lines,rfac):
    """Take Chebychev auxiliary lines and return lines with modified a_(1,1)

    INPUT:
    lines - list of auxiliary information lines to check
    rfac - rate coefficient  multiplication factor
    OUTPUT:
    lines - list of modified auxiliary information lines

    """
    # Compile the regular expression to match the Chebychev `a`
    # coefficients and CHEB keyword.
    Amatch = re.compile(r'(([-+]?[0-9]+(\.[0-9]+)?[eE][-+]?[0-9]+)|'
                        '([0-9]+(\.[0-9]+)?))')
    chebmatch = re.compile(r'(?i)^[\s]*CHEB')

    # Set a logical for whether or not we've found the first line with a
    # CHEB keyword (not TCHEB or PCHEB).
    firstChebLine = True

    # Convert the input rfactor to log10 of the rfactor.
    rfac = Decimal(rfac)
```

```python
47          addfac = Decimal.log10(rfac)

49          # Loop through the input lines
            for lineNum in range(len(lines)):
51              line = lines[lineNum]
                chebcond = chebmatch.search(line)

53
                # If this is a 'CHEB' line and its the first time we've
55              # encountered a 'CHEB' line, set `firstChebLine` to `False`
                if chebcond is not None and firstChebLine:
57                  firstChebLine = False

59              # If this is a 'CHEB' line and it is not the first time we've
                # encountered a 'CHEB' line, match the a_(1,1) coefficient, and
61              # add log10(rfactor) to it.
                elif chebcond is not None and not firstChebLine:
63                  acoeff = Amatch.search(line)
                    x = Decimal(acoeff.group(1))
65                  x = x + addfac

67                  # Format the new a_(1,1) into scientific notation. Replace
                    # the correct line in `lines`. Break out of the loop to
69                  # avoid changing any more coefficients.
                    modline = line[:acoeff.start()] + '{0:13.6E}'.format(x)\
71                              + line[acoeff.end():]
                    lines[lineNum] = modline
73                  break

75          # Return the list of modified lines
            return lines
77      ###############################################################################
        ###############################################################################
79      def auxcheck(lines,matchcond,rfac):
            """Take auxiliary lines and return lines with modified Arrhenius coefficients.
81
            INPUT:
83          lines - list of auxiliary information lines to check
            matchcond - compiled regular expression used to search the auxiliary
85                      lines for a particular condition
            rfac - multiplication factor for the Arrhenius coefficients
87          OUTPUT:
            lines - list of modified auxiliary information lines

89
            """
91
            # Compile the regular expression to match the Arrhenius
93          # coefficients. This is intentionally different from the Amatch in
```

190

```python
        # run_sens.py
95      Amatch = re.compile(r'(([-+]?[0-9]+(\.[0-9]+)?[eE][-+]?[0-9]+)|'
                            '(?<![\d\.])([0]+\.?[0]+)(?![\d]))')

        # Loop through the lines in the input list
99      for lineNum in range(len(lines)):
            line = lines[lineNum]

            # Check that the line matches the input matching condition. If
103         # not, the line is not modified
            skip1 = matchcond.search(line)
105         if skip1 is not None:

                # If the line matches the proper condition, find the
107             # Arrhenius coefficient, multiply it by two, reconstruct
                # the line, and overwrite the original line in the input
109             # list.
                Afactor = Amatch.search(line)
111             x = Decimal(Afactor.group(1))
                x = Decimal(rfac) * x
113             modline = line[:Afactor.start()] + str(x) + line[Afactor.end():]
                lines[lineNum] = modline

        # Return the list of modified lines
117     return lines
119 ##############################################################################
    ##############################################################################
121 class cd:
        """Change directory.

123
        For use with the `with` keyword, i.e. `with cd(dir):` changes to the
125     directory `dir` within the `with` construct

        """
127

        def __init__(self, newPath):
129         """Set the newPath attribute to be the argument passed to the class."""
            self.newPath = newPath
131

        def __enter__(self):
133         """Change directory when the class is entered."""
            self.savedPath = os.getcwd()
135         os.chdir(self.newPath)

137     def __exit__(self, etype, value, traceback):
            """Change back when the class is exited"""
139         os.chdir(self.savedPath)
```

141 ##